# NOBLE METAL, ALLOY AND HYBRID PLATFORMS FOR PLASMONIC SENSING APPLICATIONS

Thesis submitted to
the University of Calicut in partial fulfillment of the
requirements for the award of the degree of

**Doctor of Philosophy**
**in Chemistry under the Faculty of Sciences**

by

**ANJU AJAYAN**

Under the guidance of
**Dr. P. Raveendran**

**DEPARTMENT OF CHEMISTRY**
**UNIVERSITY OF CALICUT**
**KERALA**
**JANUARY 2019**

# CERTIFICATE

This is to certify that the thesis entitled **"NOBLE METAL, ALLOY AND HYBRID PLATFORMS FOR PLASMONIC SENSING APPLICATIONS"** is an authentic record of the research work carried out by **Anju Ajayan** under my guidance for the award of the degree of Doctor of Philosophy in Chemistry under the faculty of Sciences, University of Calicut, Kerala and the same has not been submitted elsewhere for any degree or diploma.

Calicut University
January 2019

**Dr. P. Raveendran**
(Supervising Teacher)

# DECLARATION

I hereby declare that the thesis entitled **"NOBLE METAL, ALLOY AND HYBRID PLATFORMS FOR PLASMONIC SENSING APPLICATIONS"** is the bonafide report of the original work carried out by me under the supervision of Dr. P. Raveendran, Professor, Department of Chemistry, University of Calicut for the award of the degree of Doctor of Philosophy in Chemistry Under the Faculty of Sciences, University of Calicut, Kerala. The content of this thesis have not been submitted to any other institute or University for the award of any degree or diploma.

Calicut University
January 2019

**Anju Ajayan**

# ACKNOWLEDGEMENT

*I am extremely happy in presenting my doctoral dissertation.*

*In this journey of hard work and struggle, I am fortunate to have got many friends and received help, guidance, support and solace from different corners. I could complete the thesis with the help of several amazing dignitaries around me. I take this opportunity to express my sincere gratitude to them all for the love, care and support they showered on me.*

*Let me first bow to god Almighty and pray for your blessings.*

*First and foremost, I would like to express my special appreciation and thanks to my supervising guide Dr. P. Raveendran, Professor and Head of the Department of Chemistry, University of Calicut for the support, encouragement and guidance for my research period. His supervision and timely advices as well as his professional approach to research have helped me greatly to complete my thesis. I greatly acknowledge all his contributions and the valuable suggestions.*

*I am also grateful to Dr. V. M. Abdul Mujeeb and Dr. K. Muraleedharan, former heads of the department for providing me all necessary assistance for pursuing my research. I also thank the members of the chemistry faculty, Prof. E. Purushothaman, Prof. Abraham Joseph, Prof. D. Bahuleyan, Dr. N. K. Renuka, Dr. M. T. Rameshan, and Dr. Pradeepan Periyat for their Support.*

*I gratefully acknowledge Sri. Mohanan. A, Librarian, Dept. of Chemistry, University of Calicut and Sri. Satheesan. K, Technician, University of Calicut for the assistance they have given to me.*

*I wish to place on record my deep gratitude to Dr. Muhammed Basheer, Honorable Vice Chancellor, University of Calicut for the support given to me.*

*I am very much indebted to those who have rendered help in my work from outside the University. I thank Dr. M. Eswaramoorthy, JNCASR, Bangalore for his valuable suggestions and help to carry out the SEM Analysis.*

*I express my gratitude to STIC, Cochin University of Science and Technology, NIT Calicut, SAIF Mahatma Gandhi University, PSG College of Technology, Coimbatore. I am thankful to the Department of Nanoscience and Technology, Department of Physics, University of Calicut for helping me in Carrying out the analyses imperative for my research work.*

*I would like to express my gratitude to all the non-teaching staff, department of Chemistry for their kind help and support.*

*I place on record my special thanks to all the staff of the University Central Library for their wholehearted co-operation.*

*I gratefully acknowledge the financial assistance extended to me by the CSIR, New Delhi for pursuing my Ph. D work.*

*I remember with gratitude all my school, college and tuition teachers who have enlighted me very much in my studies. Sri. Premdas. S. V. needs special mention. He is the one who gave me the magical key to the mesmeric world of Chemistry.*

*I am also grateful to all the teachers who have directly or indirectly inspired me from kindergarten to college level. Their role in developing my character, personality, knowledge and attitude is profound and appreciated.*

*I am blessed with some wonderful friends around me. My heartfelt gratitude is extended to my colleagues in Physical Chemistry Research Lab and all my dear friends, especially Ansi. V. A, Dr. Bindu. U, Dr. Anju. M, Dr. Nikhila. M. P, Dr. Divya.T, Vineeth. M, Jyothi. P. R, Dr. Aparna. K. Balan, Pranav. K. G., Akhila. A. K. My gratitude to them cannot be expressed merely with a few words for the precious time and all the fun we had in the last few years.*

*Last but not the least, I like to dedicate this to my family-My parents, brother, husband and in-laws. Words fail to express how grateful I am for all of the sacrifices that they've suffered for me. Their prayers sustained me so far.*

***Anju Ajayan.***

*Dedicated to.....*

*My Family.....*

# PREFACE

Developments in the area of nanoscience and technology have revolutionized the area of material science and also the scientific world as a whole. It finds broad spectrum of applications in diverse disciplines. The nano structures, materials, and devices exhibit novel properties and functions on account of the smaller size. They possess unique structural, optical, electrical and mechanical properties differing from the bulk phase. The aim of nanotechnology is to combine all the manufacturing and non-manufacturing aspects of various scientific streams such as chemistry, biology, material science, molecular engineering, medicine, ecotoxicology etc to fabricate structures that can revolutionize our world.

Despite various measures adopted toward cleaner environment, pollution is still a concern. We need to find novel methods to address environmental hazards. Exposure to environmental pollution is one of the main sources of health risk throughout the world. Sensing of toxic materials such as heavy metals, dyes, peroxide etc requires sophisticated instruments and time consuming sample pretreatment. There is a profound urge towards the development of simple, fast yet inexpensive sensors for the detection of toxic materials in water bodies. Noble metal nanoparticles deserve attention in this regard as they find application for the heavy metal detection without the help of costly instruments. Surface enhanced Raman Spectroscopy has become an area of intensive research as it is able to find molecules even at a concentration of $10^{-6}$ up to $10^{-12}$.

Carbon based nanostructures are blessed with high mechanical strength and less weight. These nanostructures are incorporated into many industrial applications such as in chemical and semiconductor sectors. Nanomaterials are used in medicinal purposes also. But concerns about the safety of nanomaterials were expressed by many researchers as it is only an emerging area and the understanding that the nanomaterials are highly reactive species on behalf of their smaller size. Scientists became aware of the toxicological hazards due to their enhanced chemical, electrical and magnetic reactivity of nanomaterials. The chapters are arranged in the following manner.

The second chapter describes the general instrumental methods used for the characterization of the metal NPs and their networks. Electron microscopic techniques such as Scanning Electron Microscopy (SEM), Transmission Electron Microscopy (TEM), UV-Visible absorption spectroscopy, diffuse reflectance spectroscopy, XRD, FTIR etc are described.

The third discusses a simple anti-solvent method for the controlled deposition of metal and alloy nanoparticles for plasmonic applications. Here we discuss the preparation of two-dimensional arrays of Au, Ag, and Au-Ag alloy nanoparticles by the controlled deposition of Au, Ag and Au-Ag alloy nanoparticles from the colloidal dispersions of the respective nanoparticles. These arrays have been used for mercury sensing as well as a substrate for Surface Enhanced Raman Spectroscopy (SERS) taking 1, 4-benzenedithiol as the model system.

The fourth chapter deals with the application of Au, Ag, and Au-Ag NPs for sensing Hg(II) ions. A detailed comparative study has carried out using Au, Ag, and AuAg alloy nanoparticles of various compositions to establish their suitability for sensing Hg (II) ions by investigating the typical variations in the values of $\lambda_{max}$.

The fifth chapter discusses the synthesis of Copper nanoparticles@Graphene Oxide composite for the selective detection of hydrogen peroxide.

The sixth chapter presents the conclusions of the results of the investigations described in the previous chapters and presents a future outlook of the work.

# CONTENTS

# GLOSSARY OF TERMS

| | |
|---|---|
| SEM | Scanning Electron Microscopy |
| FE-SEM | Field emission Scanning Electron Microscopy |
| STM | Scanning Tunneling Microscopy |
| TEM | Transmission Electron Microscopy |
| AFM | Atomic Force Microscopy |
| NP | Nanoparticle |
| MNP | Metal Nanoparticle |
| NMNP | Noble metal Nanoparticle |
| NC | Nanocomposite |
| Au NP | Gold Nanoparticle |
| Ag NP | Silver Nanoparticle |
| Cu NP | Copper Nanoparticle |
| CNT | Carbon Nanotube |
| DOS | Density of states |
| QD | Quantum Dot |
| MNC | Metal nanoclusters |
| SPR | Surface Plasmon Resonance |
| LSPR | Localized Surface Plasmon Resonance |
| SPP | Surface plasmon polaritons |
| XRD | X-ray Diffraction Spectroscopy |

| | |
|---|---|
| FTIR | Fourier Transform infrared Spectroscopy |
| SERS | Surface Enhanced Raman Spectroscopy |
| CEME | Classical Electromagnetic Enhancement |
| CNT | Carbon Nanotube |
| SE | Secondary Electron |
| BSE | Back Scattered Electron |
| can | Acetonitrile |
| BDT | 1,4-Benzene dithiol |
| GO | Graphene Oxide |
| NIR | Near Infra Red |
| $H_2O_2$ | Hydrogen Peroxide |
| AA | Ascorbic Acid |

# CHAPTER 1
# INTRODUCTION

## Contents

## 1.1. Introduction

The recent focus on the development of advanced functional materials has been primarily due to the developments in the area of nanoscience and technology. It has evolved as a multidisciplinary area of research with a broad spectrum of applications in various disciplines such as biology, medicine, agriculture, energy, electronics, healthcare, textiles, transport, construction, cosmetics, water treatment etc. [1, 2] It can be said that there is no area of research untouched by the advancements in nanoscience and technology. It encompasses the development and utilization of structures, materials, and devices in the nanometer size regime exhibiting novel properties and functions on account of the smaller size. The design and creation of novel architectures in the nanometer size regime, their characterization, as well as the development of applications using these material structures, devices and systems form the heart of nanoscience and technology. In general, the bulk properties of the materials undergo significant and often tunable variations in the nanometer size range, depending on the size of the particles. [3, 4]

One can probably define nanoscience and technology as the science, engineering, and technology concerned with the deliberate design and construction of materials at the nanoscale, or the manipulation of atoms or molecules on a nanometer scale, in the range of 1-100 nm. One nanometer is a billionth of a meter, which is $10^{-9}$ of a meter. With the emergence of this new area, many definitions were put forwarded and the most accepted definition was given by the

NASA scientists and it can be stated as follows: "the creation of functional materials, devices, and systems through the control of matter on the nanometer length scale (1-100nm) and exploitation of novel phenomena and properties (physical, chemical, and biological) at that length scale". This also implies that nanoscience and technology deals with materials that undergo size-dependent optical and electrical properties which can be manipulated into engineering designs for applications in diverse disciplines. In fact, in one of the historically important lectures in 1958 entitled "There is plenty of room at the Bottom", the tremendous implications of materials and designs in the nanoscale was perceived and presented by Nobel Laureate Richard P. Feynman. [5] He called for research in the manipulation of molecules and materials in the nanoscale and many perceive that it was this prophetic call that eventually led to the developments in nanoscale science and technology.

The emergence of the detailed understanding about the structure - both electronic as well as the multi-dimensional architectures- led to the visualization and creation of several nanoscale functional architectures in one-dimensional (1D), two-dimensional (2D), or three dimensional (3D) spatial preferences and transformed materials science completely. This led to a new vision of the design of functional materials for applications in almost all branches of science and engineering. Such developments threw more light on the structure-property relationships starting from their fundamentally unique units and slowly transforming in property while moving to the bulk organizations. It also transformed many of the existing methods in

materials design with wide implications for various applications in chemistry, physics, biology, biomedical engineering, medicine, electrical engineering, computer architecture and many other specialized disciplines. This nanoscale revolution in materials science also led to the development of many bottom-up synthetic strategies for the creation of molecularly designed architectures with designed functions based on the manipulation of atoms or molecules guided by the fundamental principles of chemistry and physics. Many other developments in auxiliary areas of physics and chemistry have also helped the development of nanoscience. For example, the development of electron microscopy greatly helped researchers in overcoming the resolution barriers existed in imaging small scale objects. The highest resolution possible for imaging objects was limited to $\lambda/2$ where $\lambda$ is the wavelength of the electromagnetic radiation. With the use of de Broglie waves of electrons, this is far more reduced now and electron microscopic techniques such as Transmission Electron Microscopy (TEM) and Scanning Electron Microscopy (SEM) has made it possible to image nanoscale materials with good resolution and contrast. [6]

With the possibility of increasing the voltage between the electrodes, faster electrons and better resolution became possible. Many advanced techniques such as High Resolution TEM and Field-Emission SEM made significant improvement in imaging materials with better accuracy. Atomic Force Microscopy enabled the scanning of surface morphology precisely. All these developments, along with the new vision of materials science in the nanoworld led to several intelligent or smart materials that made significant leaps in diverse

areas such as optics, imaging, medicine, biomedical engineering, lasers, sensing, industrial catalysis, etc. [7-10]

Nature is a treasure-house of many functional nanomaterials. The self-assembled nanostructured organizations in biology such as DNA, lipid bilayers, micellar assemblies etc., play subtle functional roles in important biological processes. They possess several functional roles depending up on the designed molecular architectures suitable for the roles they have to play for the survival of various species. For example, it is well-established that the proteins in most species will become non-functional under high pressures. On the other hand, most hyperthermophilic proteins in under-water species will get denatured under ambient conditions. This is the diversity of bio-architectures.

## 1.2. Inorganic Nanoparticles

Among the inorganic nanomaterials, metal and semiconductor nanoparticles and their assemblies occupy a special place. This is due to the size-dependant variations in their electronic and optical properties. The self-assembled architectures of the fundamental nanoparticles and their functionalized forms finds several applications including optical, sensing, spectroscopic, as well as in applied catalysis. The catalytic applications are enhanced by the high surface area of these materials in the nanoscale. Carbon nanostructures, such as fullerenes, nanotubes (CNTs), graphene, etc are also of great applications in industrial area. [11-13]

### 1.2.1. Nanoparticles of noble metals and their alloys

Noble metal nanoparticles and their alloys have a historic presence in the ancient period, particularly in pottery, paintings, and traditional medicine. Colloidal dispersions of silver and gold were used in the medicines of ancient India and China. The historically important "Lycurgus Cup," in the British Museum, shows beautiful colour displays because of the NPs of Gold-Silver alloy they contain. The medieval European churches have colourful tinted glass walls and windows made from gold nanoparticles in various matrices. The *thanka bhasma* of India and the *Aurum Potabile* (drinkable gold) of the ancient European medical systems were nothing but gold particles in the nanometer size regimes and were thought to have medicinal action against many diseases.

In modern day science, the first synthesis of colloidal Au NPs goes back Michael Faraday's method (1857) of the synthesis of stable, aqueous dispersions of Au NP. [14] Faraday described the nanoparticles as "divided metals", a definition still considered very relevant in describing its material properties. He perceived that when metal is divided into smaller and smaller units, at some stage it stops acting as a metal, an important observation from even our present day understanding on metal nanoparticles. He could also present a reasonably good explanation for the colours exhibited by the metals in the colloidal state. In 1905, Einstein suggested that the colloids behave as big atoms and explained their movement in terms of Brownian motion. [15] Jean-Baptiste Perrin, who confirmed this view

experimentally, was awarded the Nobel Prize in Physics in the year 1926. However, It was Gustav Mie (1908) who presented a theory for the various beautiful colours exhibited by metal nanoparticles of different sizes and metals. [16] Gans gave a modification to this theory later.

### 1.3. Importance of Nanosize

Nanomaterials are made up of a few number of atoms or molecules, or what we call clusters. In the nanometer dimensions, materials exhibit unique physical and chemical properties. At particle sizes below 100 nm, the ratio of the number of atoms on the surface to the number of atoms inside increases as demonstrated in Figure 1.1 and Figure 1.2

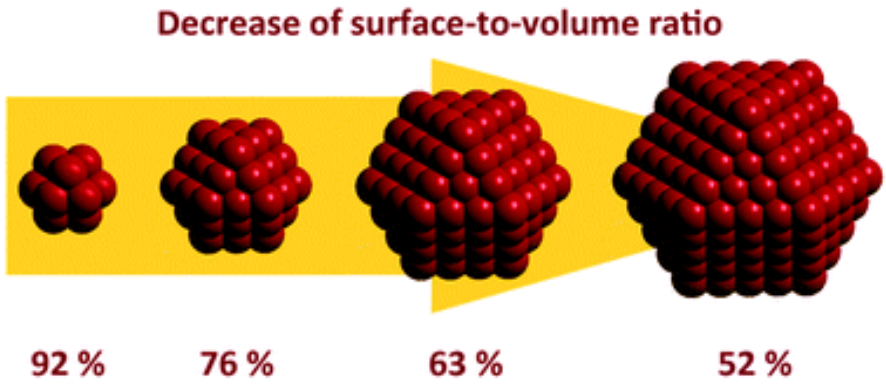


**Figure 1.1.** Schematic diagram showing the decrease in surface area with increase in size (adapted from Sonstrom, P.; Baumer, M. Supported colloidal nanoparticles in heterogeneous gas phase catalysis-on the way to tailored catalysts. *Phys. Chem. Chem.* Phys. **2011**, 13, 19270–19284.)

It can be seen that the ratio of the number of atoms on the surface to those in the interior increases drastically upon size reduction. By dividing a particle into smaller units, the surface area for a given volume of a material increases drastically. The increase in the ratio of surface area to volume with decrease in individual particle size is shown in Figure 1.2. If we assume that a cube is divided into eight cubes, the surface area gets doubled as shown schematically. In the same way, if we divide the particles many-fold into cubes of very small dimensions, the increase in surface area can be tremendous. Since many applications such as sensing, memory, catalysis, etc. depend on the active surface area, one can expect significant advantages in size reduction.

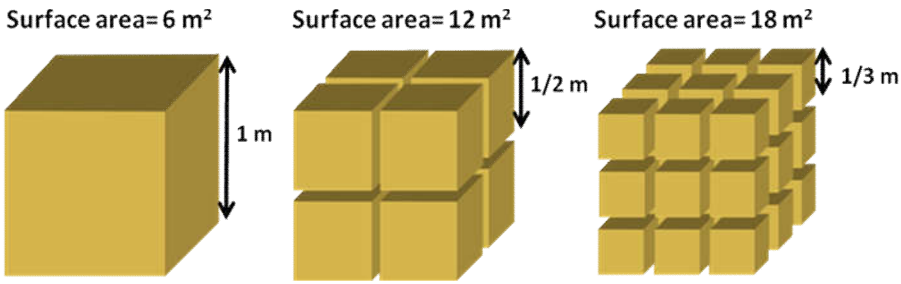


**Figure 1.2.** Diagrammatic representation of the increase in the surface area as the individual particle size is decreased (adapted from Rayappan, J. B. B.; Jeyaprakash, B. G. Introduction to Materials and Classification of Low Dimensional Materials. *NPTEL – Electrical & Electronics Engineering – Semiconductor Nanodevices,*).

### 1.3.1. Confinement Effects

As discussed in the previous sections, nanomaterials have at least one of the dimensions in the nanometer size. When particle

dimension is reduced, energy levels become discrete rather than the continuum in the bulk. Depending on the particle sizes, the discreteness of the energy levels increases. This is due to the quantum confinement effects.

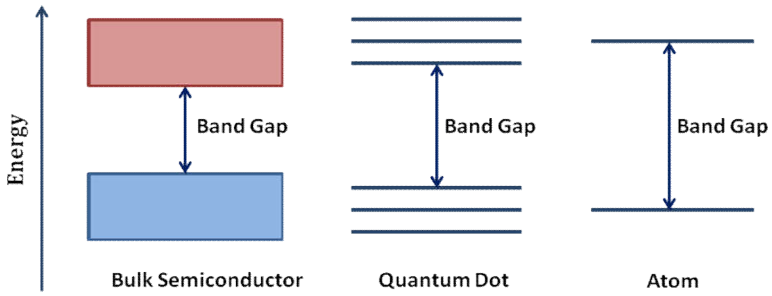


**Figure 1. 3.** Evolution of Discreteness in Energy levels with size reduction (adapted from Adlim. Review: Preparations and application of metal nanoparticles. *Indo. J. Chem*. **2006**, 6 (1), 1–10).

Density of states (DOS) refers to the quantum mechanical approach to determine the number of states available in a system which is essential to understand various spectroscopic and transport properties of materials. It is the number of states per unit energy range and its mathematical representation is density distribution. If there are many states available for occupation, then it is said to have a high DOS value and vice-versa. In the case of matter at bulk state, the density of states is continuous and for isolated systems, it becomes discrete. [17]

In the case of a semiconductor material, the free motion of carriers is limited to two, one and zero dimensions. The optical, electronic and magnetic properties of a material were determined by the DOS and the electronic energy levels. There is a dramatic change

in the DOS as the particle dimensions got reduced. The topological properties of a system also have a major role in determining the density of states.

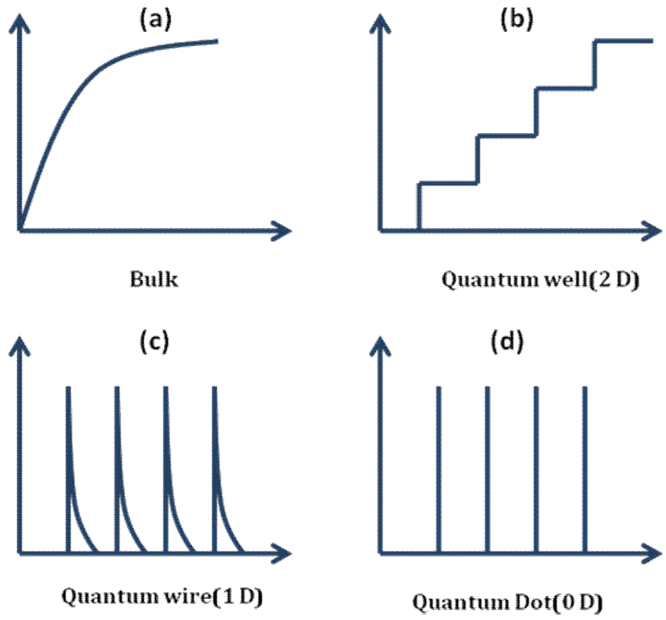


**Figure 1.4**. The diagram illustrates the change in DOS with change in size of a nanomaterial. (adapted from Dresselhaus, M. S.; Chen, G.; Tang, M. Y.; Yang, R. G.; Lee, H.; Wang, D. Z.; Ren, Z. F.; Fleurial, J. P.; Gogna, P. New directions for low-dimensional thermoelectric materials. *Adv. Mater*. 2007, 19, 1043–1053.

### 1.3.2. Quantum Dots (QDs):

For semiconducting nanocrystals in the 1-30nm size range, the band gap is a few eV. Upon the application of a suitable potential, the electron gets excited from conduction band to valence band and creates electron-hole pairs (excitons). The electron - hole is described as Bohr-exciton radius.

The band gap has affixed value for the bulk materials. However, as the size decreases, the energy levels in quantum dots become discrete and the Bohr exciton radius ($r_B$) alters upon the addition or subtraction of even a single atom. Since $r_B$ is much smaller than the size of the bulk crystal, the exciton moves freely through the lattice. On the other hand, for quantum dots, the Bohr-exciton and the crystal dimensions are of the same order of magnitude. Generally, one can describe a quantum dot as a particle with size comparable to the Bohr- exciton radius.

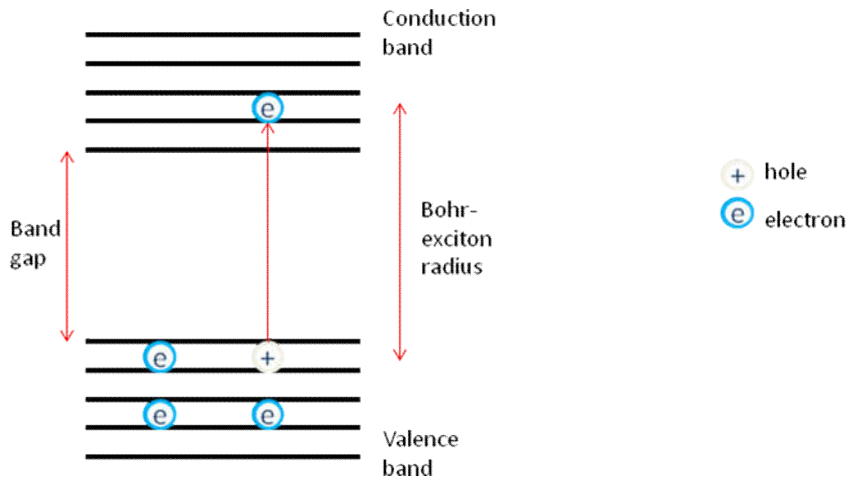


**Figure 1.5.** Schematic description of Bohr exciton radius (adapted from "Quantum Dots Explained." *Evident Technologies*. 2008).

For nanoclusters, the "Kubogap" becomes comparable to kT (the thermal energy), causing change in the conducting properties of the cluster. The breadth of a band depends on the interaction between the individual entities. Clusters of small molecules are characterized by weak interactions, whereas metallic clusters have somewhat strong

neighbor interactions. This will cause greater DOS near Fermi energy ($E_F$) for small metal clusters, causing a reduction in the conductance of electrons.

Metals are less affected by quantum confinement because quantum confinement starts at the band edges than at the centre of the band. [18] Also, the metal nanoclusters (MNCs) are more sensitive to shape than size. [19] Confinement effects in different dimensions are described in Figure 1.6.

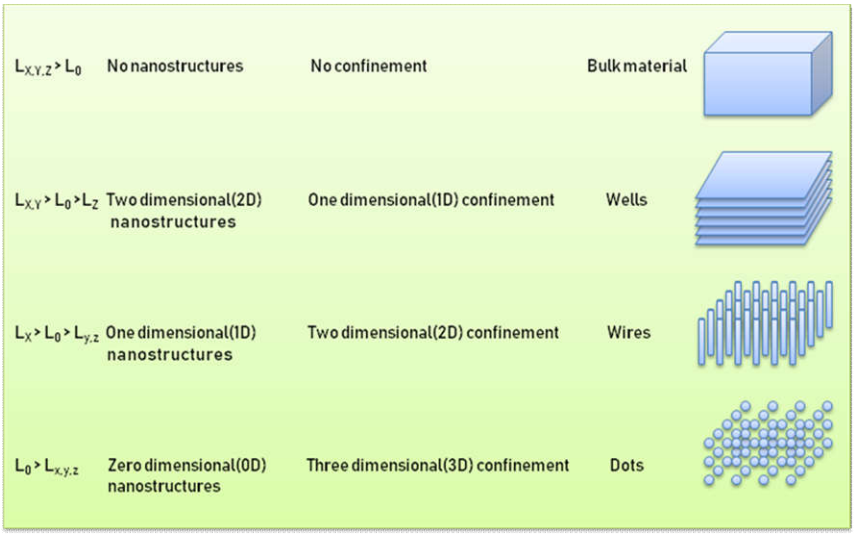


**Figure 1.6.** Schematic description of the confinement effects in different dimensions (adapted from Fundamentals of nanomaterials, Lecture 5, Nanomaterials).

They constitute a second class of nanostructures wherein the crystallite size is unrestricted only in one dimension. The electron-hole movement is restricted in the other two directions. These are one-dimensional nanostructures or nanowires and are characterized by two

dimensions comparable to Bohr-Exciton radius. Metal nanowires, carbon tubes, etc are examples for this.

### 1.3.3. Two-dimensional Nanostructures

For this class of materials, the motion of electron-hole pairs is confined only in one dimension leaving the other two dimensions unrestricted. Thin films are examples of 2D materials. Graphene also can be considered as a typical example of a two-dimensional nanostructure.

## 1.4. Optical properties of Metal and Alloy Nanoparticles

Metal nanoparticles (MNPs) have attracted much interest among researchers in the recent years due to the important applications in sensing, catalysis, optics, and imaging. NPs of metals such as Au, Ag, and Cu are characterized by unique colours and have attracted much attention in the recent years due to their potential applications in many advanced areas of physics, chemistry, biology, and medicine. From a fundamental perspective, these colours arise due to a phenomenon called the Localized Surface Plasmon Resonance (LSPR). [20]

It results from the resonant optical absorption in the visible region of the electromagnetic spectrum resulting from collective oscillation of the free electron cloud around the positively charged particle center with respect to the oscillating electromagnetic radiation. The observed colour is complementary to the colour absorbed. These are usually measured using UV-Visible absorption spectroscopy and

are characterized by the wavelength at which maximum absorption is observed ($\lambda_{max}$). Spherical nanoparticles of Au, Ag, and Cu in the approximate size range of 10-50 nm are characterized by $\lambda_{max}$ around 520nm, 400nm, and 560nm, respectively.

The displacement of the electron cloud with respect to the resonant electromagnetic radiation and the resulting surface charge polarization are shown in Figure 1.8.

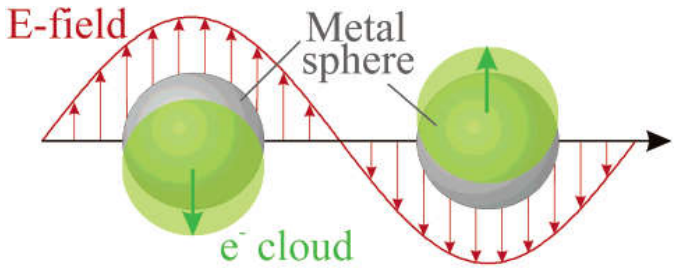


**Figure 1.7.** Polarization and displacement of the electron cloud with respect to the oscillating electric field of the electromagnetic radiation (adapted from Reference 61).

Since the charge polarization is temporary, the Coulombic attraction due to the positively charged nuclei will try to restore the electron cloud to the initial position. This leads to the collective oscillation of the electron cloud called plasmon polaritons. The term "Plasmons" was proposed by Shopper to explain the pheneomenon. When the incident radiation couples in phase with the natural frequency of the plasmon, a resonant absorption of electromagnetic radiation occurs resulting in the excitation of the electron cloud to conduction band. [21]

SPR can be of two types: SPP (Surface plasmon polaritons) and LSPR (Localized surface plasmon resonance). SPP originates from the propagating waves along a metal surface. [22, 23] LSPR is observed for very small particles; smaller than the wave length of light (or the condition is that radius should of the order of 1/100 of wave length of light). The NPs experiences a field that is spatially constant, quasi-static limit. Thus, it must be noted that only the dipolar resonance of the plasmon causes the observed optical resonance. LSPR can generate a local field enhancement of 100 – 1000 times greater than the incident light. This is due to the confinement of the surface plasmon to a small volume which results in an oscillating electromagnetic field very close to the surface. This causes the extinction coefficient to reach a maximum value at the resonance frequency resulting in a sharp absorption band. For larger particles quadrupole or higher resonances can occur, giving rise to multiple absorption bands, but of relatively low intensities. The study of the surface Plasmon absorptions from metal nanoparticles is known as nanoplasmonics or simply, Plasmonics.

Gustav Mie (1908) provided an explanation for the color changes displayed by spherical particles for given values of dielectric constants. Neglecting the interparticle interactions, he applied the Maxwell's equation to spherical metal nanoparticles with a bulk dielectric function $\varepsilon_{\omega}$.

For an incident radiation with intensity $I_0$ corresponding to wave length λ and a dielectric constant $\varepsilon_0$, the transmitted intensity is given by

$$I = I_0 e^{-\mu l}$$

Here, μ is the extinction coefficient, which depends on the the total number of particles N and the volume V of colloidal particles.

$$\mu = \frac{N}{V} C_{ext}$$

Here $N$ is the number of particles, $V$ is the volume of the particles and $C_{ext}$ is the extinction cross-section of a particle. For larger particles,

$$C_{ext} = C_{abs} + C_{scatt}$$

$C_{abs}$ and $C_{scatt}$ can be obtained by solving Maxwell's equations. According to Mie, in the case of very small particles, extinction is mainly due to absorption. $C_{ext}$ for small particles of radius R (dielectric constant ε') surrounded by a homogeneous medium (dielectric constant $\varepsilon_m$) was shown to be

$$C_{ext} = \frac{24\pi^2 R^3 \varepsilon_m^{3/2}}{\lambda} \frac{\varepsilon_\omega''}{\left(\varepsilon_\omega' + 2\varepsilon_m\right)^2 + \varepsilon_\omega''^2} \text{; and}$$

$$\varepsilon_\omega = \varepsilon_\omega' + i\varepsilon_\omega''$$

This expression provides not only the value of $\lambda_{max}$, but also the line shape of the absorption band. The maximum value of the extinction coefficient is obtained when $\varepsilon_{\omega}^{'} = -2\varepsilon_m$ becomes the condition for resonance. Thus, LSPR peak strongly depends on the dielectric constant of the material. The dielectric constants of metals $\varepsilon^{'}$ and $\varepsilon^{"}$ are depend strongly on frequency and with both real and imaginary components. It is also clear from this derivation that the magnitude of absorption is proportional to $R^3$. Thus, in the case of small particles, the LSPR is dominated by absorption. With increase in the size of the particle, contributions from scattering too become significant.

Although Mie theory could provide a good explanation for the absorption spectra from spherical nanoparticles, it failed to explain the spectra from non- spherical shapes such as disks or rods. Gans (1912) modified the Mie equation to account for the nanorods sand suggested two Plasmon absorptions for the longitudinal and transverse modes.

Gan provided the expression

$$C_{ext} = \frac{8\pi^2 R^3 \varepsilon_m^{3/2}}{3\lambda} \sum_j \frac{\left(\frac{1}{P_j^2}\right)\varepsilon^{"}}{\left(\varepsilon^{'} + \frac{1-P_j}{P_j}\varepsilon_m\right)^2 \varepsilon^{"2}}$$

where $P_j$ stands for the depolarization factors for the nanorod axes (a > b = c).

$$P_a = \frac{1-r^2}{r^2}\left[\frac{1}{2r}\ln\left(\frac{1+r}{1-r}\right)-1\right], \text{ and}$$

$$P_b = P_c = \frac{1-P_c}{2} \quad \text{where r} = \sqrt{1-\left(\frac{b}{a}\right)^2}\ .$$

The SPR for nanorods has two bands. With an increase in the aspect ratio, the separation between the ones corresponding to the longitudinal SPR also increases. These equations are used to calculate the extinction spectra of Au nanorods of any aspect ratio.

Alloy nanoparticles constitute a separate class. While considering the optical properties of alloy NPs, the dielectric function of the alloy NP needs to be considered. $\varepsilon = a\varepsilon_A + (1-\alpha)\varepsilon_B$ ;

where α is the relative volume concentration of the metal A. The dielectric functions $\varepsilon_A$ and $\varepsilon_B$ are calculated in the same way as for single MNPs. With further advancement in the area several physicists and chemists have attempted to give better descriptions of the surface plasmon band.

## 1.5. Chemical Properties

### 1.5.1. Catalytic activity:

As stated previously, nanomaterials are characterized by high surface area to volume ratio. In a catalyzed reaction, the catalyst usually reacts with the reactant to form a temporary intermediate which then regenerates the original catalyst in a cyclic process.

Increase in the amount of catalyst concentration increases the rate of a chemical reaction. But in the case of nanomaterials as catalysts, the large surface area provides increased adsorption of reactant molecules on to the surface, resulting in a higher catalytic activity without increasing the catalyst concentration.

The catalytic activity is further enhanced by the greater number of active sites exposed to the surroundings. As the size gets reduced further, there is dramatic increase in the effective surface area accelerating the rate of a chemical reaction. Hence small MNPs are better catalysts. Gold in the bulk state is catalytically inactive, but when the dimensions got reduced to the nanoscale, it is found to be an excellent catalyst for many chemical reactions. Haruta *et al*. reported the application of gold clusters as catalysts. [24] Metal nanomaterials are used as such or can be supported on suitable porous template structures to enhance its catalytic ability. Commonly used templates for this purpose are porous structures (macro-, meso-, micro- or combinations), with well defined pore sizes to allow specific adsorption of reactants. Porous gold nanoparticles and supported mesoporous materials are excellent for catalytic applications as the catalytic activity is dependent upon the surface area. [25]

MNPs supported on porous structures of metal oxides are good catalysts for photochemical reactions. Several metal oxide possess suitable band gap to be excited by UV or Visible light, and the redox potentials can promote a series of oxidative or reductive reactions. Titanium dioxide ($TiO_2$) is widely being used in solar cells and as a

catalyst in several photoreactions due to its favorable optical and electrical properties, chemical stability, non–toxicity and low cost of manufacture. [26]

## 1.6. Synthesis of nano-sized materials

Nanoparticles are widely being used since ancient times without knowing that they are nano-sized species. But more research on the identification of nanomaterials, study on their properties and various synthesis attempts started only a century back. There are different ways to synthesize nanomaterials. A number of methods have been developed so far to generate different sized, shaped and porous nanostructures. The interest in the area of nanoparticle synthesis is not ceased yet, since different methods gives nanoparticles of different properties for applications in medical diagnostics, therapeutics etc.

There are two general methods adopted for the synthesis of nanoscale assemblies, they are top-down and bottom-up approaches. [27] In the case of Top-down approach, larger initial structures are broken down with precise control onto nano-sized objects. Typical techniques employed for reducing the size are etching, ball milling, and application of severe plastic deformation. Examples of top-down include ball milling, chemical etching, sputtering, laser pyrolysis and various lithographic techniques such as electron beam lithography, ion beam lithography, nanosphere lithography, photolithography, multi-photon photo lithography etc. [28]

Generally the top-down approaches are expensive compared to the bottom-up ones. In the case of Bottom-up method, the individual building units such as atoms, molecules, polymers and colloids are assembled with needed controllability. The basic units are self assembled by virtue of the physical forces operating in between them to get nanoscale particles. Typical example is the formation of colloidal metallic nanoparticles by reducing the respective metallic ions with suitable reducing agents and stabilizing them by using capping agents. Fabrication of nanomaterials by bottom-up method is generally less expensive. Vapour deposition, Bio-reduction, chemical deposition etc comes under the category bottom-up The atoms produced after the reduction of ions are assembled to produce nano-sized structures.

There is another technique termed Hybrid Fabrication Technology, which combines both these top-down and bottom-up mechanisms simultaneously to generate nanoparticles. Various chemical strategies are adopted for fabricating nanomaterials. In the synthesis of metallic nanoparticles, suitable salts of metal ions are reduced resulting in nucleation and growth of nanomaterials. Choice of capping agent, pH of the medium, temperature etc are optimized to precisely control the size and shape of NMs. Generally used capping agents are surfactants and polymer materials such as thiols, citrates, starch, Poly Vinyl Alcohol and Poly Vinyl Pyrollidine. Chemical, photochemical, electrochemical, sonochemical and thermal methods are some bottom up routes adopted for synthesizing nanomaterials which include Sol synthesis, Sol-gel process, Co-operative self

assembly, Langmuir Blodgett method, Template synthesis and hard matter templating.

Bimetallic and trimetallic NPs are better for several applications of sensing, catalysis, photonic devices, gene delivery and electronic devices as they exhibit novel properties on behalf of their higher micro heterogeneity than their monometallic counterparts. [29-31] Co-reduction of metal ions, polyol method, gamma irradiation, photochemical method, sputter deposition, and microwave irradiation etc are employed for synthesizing alloy nanomaterials.

Deposition-Precipitation method, galvanic replacement, co-precipitation and usage of templates are some techniques for synthesizing hybrid materials. Core-shell structures belonging to nanodimensions meet numerous applications in optics, drug delivery, medicinal field and engineering. Among them most commonly used ones are metal–metal oxide core-shell as they are more interesting for several applications.

Au and Ag are mutually soluble and forms alloy in their bulk state and also in their nanoforms. A straight line is obtained when we plot the absorption maximum against the percentage of Au in the AuAg alloy compositions and this linear dependence is characteristic of the alloy nanoparticles, whereas core-shell NPs exhibit two characteristic absorption peaks. Colloidal Au@Ag nanospheres were first synthesized by Morris and Collins in the year 1964. [32] One step synthesis of Au-Ag alloy NPs by the co-reduction of $HAuCl_4$ and $AgNO_3$ by sodium citrate was done by El-Sayed *et al.* [33]

The SPR for the alloy NPs lies in between that of pure Au and pure Ag NPs. Not only isotropic alloy NPs, but also anisotropic NPs can be prepared by adopting certain stringent reaction conditions. A small change in the method will be needed for controlling the shape of the materials to be synthesized. Bimetallic nanoparticles with high aspect ratio are superior for several applications as they exhibit different properties upon modification of transverse or longitudinal modes.

Self Assembly is a thermodynamically controlled phenomenon based on the fundamental interactions such as hydrogen bonding, polar and non-polar interactions, etc, hence energetically favorable for the synthesis of NP assembles. The fascinating functional organizations of the molecules of life are governed by such interactions. There are several self assembly processes occurring in nature such as assembly of living cells during the process of mitosis, protein folding and aggregation, pairing of bases in DNA, formation of lipid bilayers etc. Nanoparticles can be organized into 1D, 2D or 3D architectures by the process of self-assembly.

We are adopting self assembly to synthesize metal NPs and also their 2D arrays. For preparing well defined nanostructures, we can employ block copolymers, which acts as good templates. The pH of the solution and polarity of the solvent are also critical in controlling and regulating self assembly. The assembly is possible either at solid interfaces or liquid interfaces since those results in a decrease in the interfacial energy.

## 1.7. Green Chemistry

Compared to the synthetic methods of synthesis, Green chemistry have several advantages such as they release less amount of hazardous chemicals to the environment, less protective equipments required, less prone to accidents, safer methods and less damage to the ecosystem. Green chemicals will degrade to non-injurious products or are recycling for further use. They have the advantage of causing lower potential towards global warming, smog formation, ozone depletion etc. No need of higher amounts of feed stock for getting higher yield in farming sector. Faster synthesis of products as the number of synthetic steps required is less. Less amount of waste, easy waste disposal, use of safer raw materials and recycling of the raw materials are some of the advantages of adopting green chemical strategy.

Another merit about green chemical strategy is atom economy, attempting to incorporate as many atoms of the raw material used in the process into the final product so as to reduce waste elimination. Chemicals with minimal toxicity are selected for synthesis purpose and the solvents used will be safer as possible. Reactions are mostly carried out at ambient temperatures and pressure. Raw materials should be renewable. Catalysts are preferred as they can increase the rate of formation of products and also save energy consumption. All these are put to use for an efficient and safer environment. We are adopting green chemical strategies for synthesizing noble metal nanoparticles and their alloys. The choice of glucose as the reducing agent and starch as the capping agent are confirming the utilization of green chemical strategies for our synthesis procedure.

## 1.8. Preparation of two-dimensional Arrays of MNPs

### 1.8.1. Anti solvent precipitation/ preferential solvation approach

Preparation of two-dimensional arrays of nanoparticles is one of the important perquisites for the plasmonic applications. Controlled, anti-solvent precipitation aided by the principles of preferential solvation is employed for the preparation of such arrays. Anti-solvent precipitation, also referred as de-solvation consists in drawing-out precipitation or solvent displacement and is achieved by decreasing the stability of a solute in a solvent in which it is dissolved. [34-36]

When a third component (anti-solvent) is added to a two component system the solubility of one component (solute) gets decreased because of the higher affinity of the third component towards the other one. The term coacervation is also used to describe this process. Anti-solvent precipitation can also be achieved by the addition of a non-solvent to a solution to induce super-saturation and solute precipitation. Careful and proper selection of the solvent and anti-solvent is important. There must be high affinity between the solvent and anti solvent or at least they need to be miscible over the concentration range at which they will be used for the process of nanoparticles by precipitation.

During anti-solvent precipitation, there occurs the imbalance of molecular interactions between solute, solvent, and anti-solvent. These interactions lead to the precipitation of particles. At that condition the solute-solute interactions will become large enough to overcome the

solvation and undergo precipitation. The entropy of mixing will be high that point. Also there should be sufficient repulsion between the particles to prevent aggregation.

Addition of the anti-solvent to the solution decreases the solvent power leading to the process of supersaturation. When the concentration of the solute becomes greater than the equilibrium saturation concentration of that particular solvent/anti-solvent mixture, the system becomes supersaturated. And above a specific critical supersaturation concentration, nucleation is induced. The time lag between the starting of supersaturation and the onset of nucleation is known as the induction time.

There will be a metastable zone in which no nucleation is observed within a given time range for a particular solvent/anti-solvent composition. The metastable zone is narrow if high and homogeneous nucleation rates are observed. Anti solvent precipitation is commonly used for the preparation of micro- and nano- sized materials especially used to make drugs in the pharmaceutical industry. The physical and chemical properties of an antisolvent can change the rate of mixing with the solutions and hence the rate of nucleation and precipitation are all influenced.

However, this technique has some drawbacks such as difficulty in controlling the size of the particles produced after precipitation, usually with a rapid growth rate can be observed in certain situations which leads to a broad particle size distribution. The process is thermodynamically controlled, thus the mechanical energy input is

minimized. Also, poor micro-mixing leads to accidental zones of local supersaturation which results in the aggregation of particles. Ultrasound Sonication helps to provide a feasible mixing method to get uniform sized particles.

## 1.9. Present study

Noble MNPs, especially Au and Ag are excellent to be used for various chemical and biological applications such as in optical and electrical sensors, as catalyst and in medical diagnostics and treatments. The Au-Ag alloy nanoparticles and their three-dimensional networks possess exceptional properties than their individual monometallic counterparts because of their higher micro-heterogeneity. As they have high affinity towards mercury even in their bulk state, they will be superior for sensing mercury when their dimensions are reduced. We have also carried out the ability of all Au-Ag bimetallic compositions in between that of pure Au and Ag. Two dimensional arrays of metal nanoparticles are excellent to be used as SERS substrates. Nanomaterials embedded in carbon nanomaterials show novel unique properties which will make them highly efficient in sensing applications.

# CHAPTER 2
# INSTRUMENTAL METHODS

## Contents

## 2.1. Introduction

In this Chapter, we discuss the general experimental methods we have adopted for the preparation and characterization of the materials. Brief accounts of the instrumental methods employed in this work such as Transmission Electron Microscopy (TEM), Scanning Electron Microscopy (SEM), Scanning Tunneling Electron Microscopy (STEM), UV-Visible Absorption Spectroscopy, X-Ray Diffraction (XRD) etc. are presented. [37, 38]

Out of the two methods of characterization available in the direct space method of identification, electron microscopic techniques and optical microscopy are used to characterize nano-sized particles. TEM, SEM, STM, and AFM are included in this category, whereas reciprocal space methods utilize the phenomena of interference and diffraction properties of electrons and photons to get the structural identification. [39, 40] In all the electron microscopic techniques, a high energy electron beam is used to image the structural properties of material as is the case with a beam of light in the case of the optical spectroscopy. [41]

The dual nature of electron, *i.e.*, both particle and wave nature, makes it a good candidate for imaging purposes. The wavelengths of the de-Broglie matter waves of electrons are much smaller than those of photons and hence a higher resolution is achieved in electron microscopic techniques as compared to that of the optical spectroscopy. It is also possible to tune the momentum of the electron by altering the potential between the cathode and the anode to get

higher resolutions. The various secondary effects that occur when an electron interacts with matter are represented in Figure 2.1.

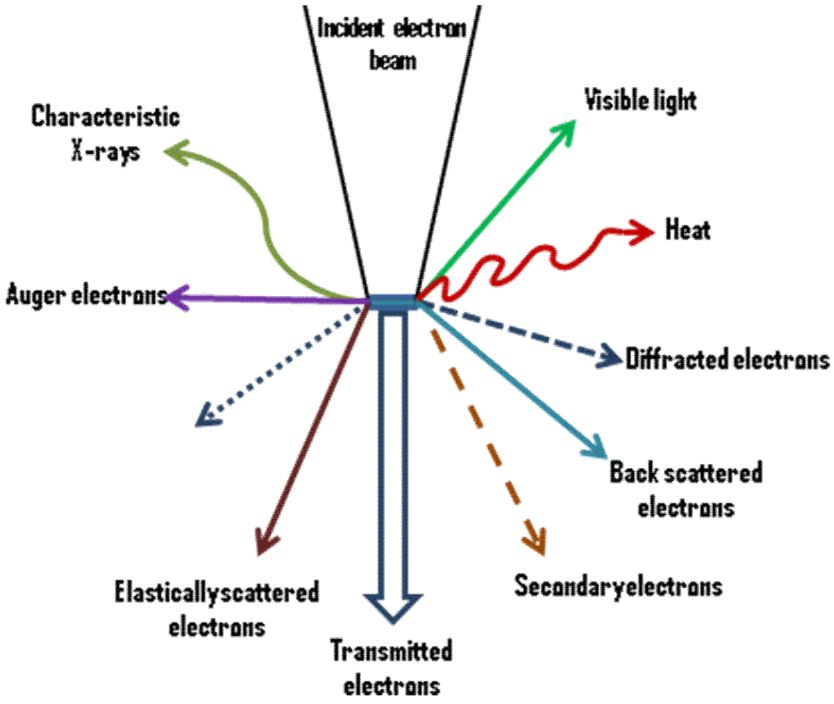


**Figure 2.1.** Schematic representation of various secondary effects when the electron beam interacts with matter (adapted from Williams, D.; Carter, C. B. Transmission Electron Microscopy, 2nd edition, Springer, 2009, p 7).

## 2.2. Elastic and inelastic scattering:

When an electron is incident on the particle, it can interact with the positively charged nuclei of the specimen and the electron is deflected back at an angle ranging from ~ 10° – 180°. Most of the electrons are scattered without any loss in energy and this process is

termed as *elastic scattering*. But at low angles of deflection, *inelastic scattering* also occurs. The latter is associated with a significant loss of energy for the incident electron. Unlike the optical scattering process (where a small cross section of the photons acquire higher energy resulting in the anti-Stokes scattering), the scattered electrons seldom bear energy higher than the incident electrons. Thus inelastic scattering of electron beam always results in a loss of energy.

### 2.2.1. Secondary Electrons (SE):

These arise from the inelastic interactions between the primary electron beam and the sample. When a primary electron is incident on the core of an atom, it causes the excitation of an inner K-shell electron. Thus, some of the K-shell electrons, which are known as secondary electrons, are ejected and the ejection of electrons can occur from the surface or near-surface with a depth of about 1-5 nm. These secondary electrons, having lesser energy than the primary electrons, are very beneficial for the analysis of the size, topography, surface morphology and the shape of the material under inspection.

### 2.2.2. Back-scattered Electrons (BSE):

Primary electrons scatter back in high deflections when collided with large atoms. These types of electrons originate from a broad region of interactions. Larger atoms scatter electrons more than the smaller ones. The intensities of the backscattered electrons are proportional to their atomic number (Z). Thus, imaging contains information on the sample composition and phase differences in an

inhomogeneous material. It is also possible to gather information on the crystal structure, topography and the magnetic field of the sample by an analysis of the BSEs. The intensity of BSEs is lower compared to SEs, but they are highly directional in nature.

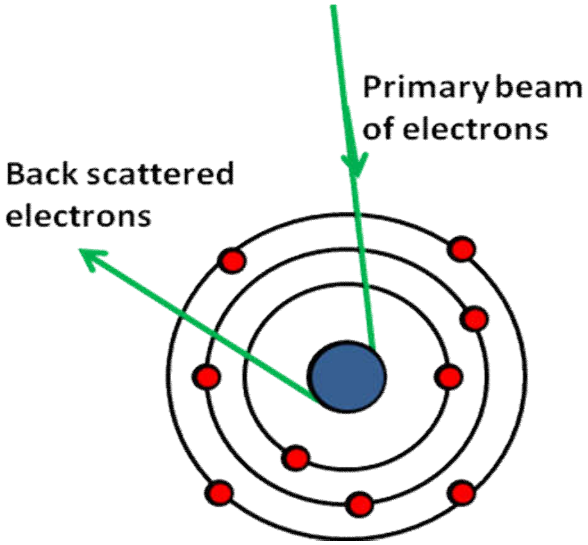


**Figure 2.2.** Schematic illustration of the back-scattering of electrons (adapted from reference 47).

### 2.2.3. Auger electrons:

The release of SEs from an atom may result in a fall of the highest energy electron in to a vacancy created by the ejected inner shell (normally K-shell) electrons. The filling of the inner-shell vacancy is then followed by a release of energy and the emission of an electron from a higher energy level of the same atom. Many times, this energy is released in the form of a photon. Another possibility is the transfer of energy to another electron, causing the ejection of that electron and is termed Auger electron. Even though this phenomenon

was first observed by Lise Meitner in the year 1922, [42] Pierre Victor Auger independently established this phenomenon shortly afterwards and these electrons were termed after him, as Auger electrons. [43-45]

The kinetic energy of these electrons will be equal to the energy difference between the energy released in the process of relaxation of the excited ion and the energy needed to eject the second electron from its orbit. The energy difference between the two energy levels can result in a release of low energy Auger electrons or can be emitted as X-rays. The vacancy created in the K-shell may get filled by the falling of an electron from the next higher L-shell. A vacancy is thus created in the L-shell and it may get filled by an electron from the M-shell and the process may accompany the emission of characteristic X-rays. The energy and the intensity of X-rays help us to determine the chemical composition of the sample both qualitatively and quantitatively.

Energy Dispersive X-ray Spectroscopy (EDS) and Wavelength Dispersive X-ray Spectroscopy (WDS) are used to characterize the X-rays thereby the surface morphology. The energy profile for the various secondary effects involved after the interaction of the primary electron beam with matter is in the order, Auger electrons < secondary electrons < BSE < X- rays. As the Auger electrons are ejected from the inner K-shell or deeper regions of the sample, there is a possibility of loss of energy through collisions with others before they can reach the surface. These Auger electrons contain information about the bonding state of that material. The X-rays are specific to each element, hence

called characteristic X-rays. X-rays are produced from K, L, and M shells at a depth of about 1–3nm.

## 2.3. Electron Microscopic techniques

Analysis of the various secondary effects caused by the electron–matter interaction is helpful for the characterization of the sample. [46,47] Two of the most common electron microscopic techniques adopted for this purpose are (a) Scanning Electron Microscopy (SEM) and Transmission Electron Microscopy (TEM). These techniques provide different types of information with respect to the sample analyzed. SEM measures the SE or BSE for the analysis of a sample which may be thick or opaque, and it provides the size, shape and morphological features of significance. On the other hand, TEM measures the intensity of an electron beam after it has passed through an electronically transparent thin sample. The basic principles of SEM and TEM are described below.

### 2.3.1. Scanning Electron Microscopy (SEM)

The SEM is a microscopic technique used to study the surface of a material by focusing it with a high-energy beam of electrons to generate a variety of signals from solid specimens. [48-50] The electron beam coming from a filament is focused to a small spot of the material surface using electrostatic or magnetic lenses. The beam is then swept across the sample and the secondary electrons coming out from the sample are collected by a detector. The signals that are obtained from electron-sample interaction contain information about the surface

morphology of the sample and also the chemical composition, crystalline nature and orientation of the materials constituting the sample structure. The imaging is done over a certain area of the surface and the corresponding two dimensional image is then generated. The intensity of the signal is directly proportional to the number of SEs produced. Generally areas ranging from approximately 1 cm to 5 microns in width can be selected for imaging purpose.

If the incident electrons are decelerated in the solid sample, the electron-sample interaction produces a variety of signals as the kinetic energy of the electrons are dissipated in different ways. These signals include SEs, BSEs, diffracted backscattered electrons, characteristic X-rays, visible light (Cathodoluminescence–CL), and heat. Scattered electrons help us to determine crystal structures and orientations of minerals. Secondary electrons and backscattered electrons are the most important for the morphological and topographic analysis.

X-ray generation occurs as a result of the inelastic collision of the incident electrons with electrons present in the discrete orbitals of an atom. The electrons gets excited and they will try to return to a lower energy state, by releasing energy in the form of X-rays. X-rays possess a fixed wavelength will be equal to the difference between concerned energy levels of the electron for that particular element. Thus, the X-ray produced from an element will be characteristic of that material. SEM analysis is considered to be a "non-destructive" technique as the X-rays generated by electron interactions doesn't result in the volume loss of the sample. The essential components of a

SEM include electron gun, sample stage, electron lenses, and detectors for all signals of interest and the display.

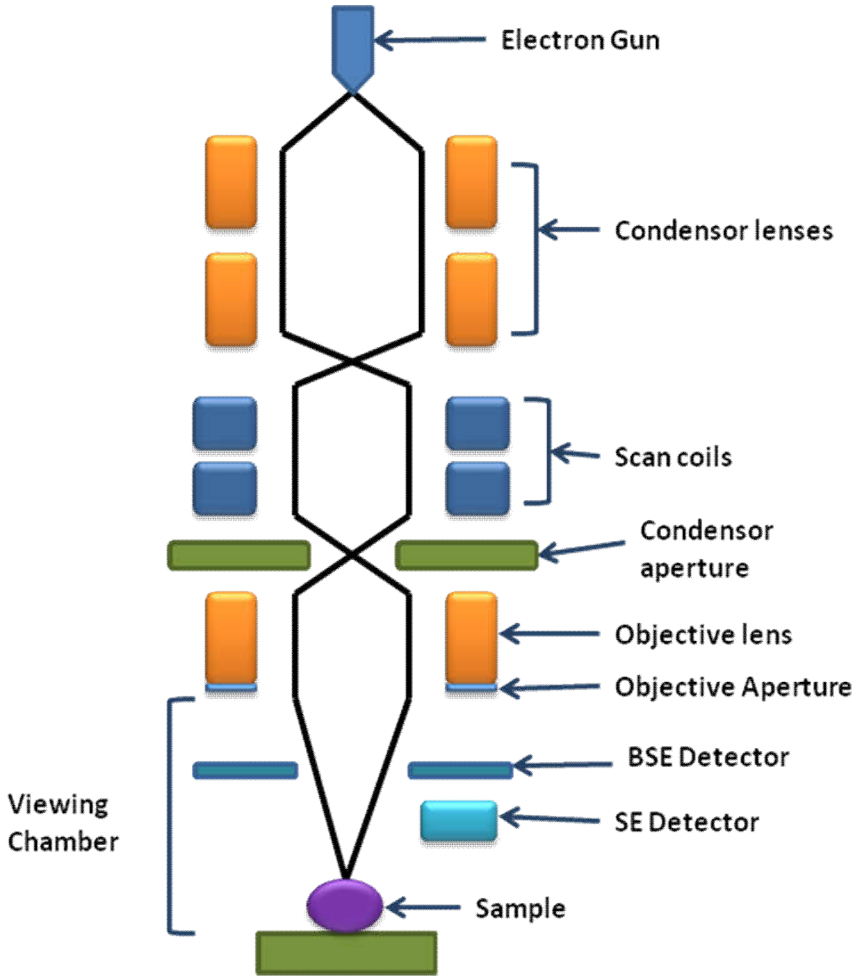


**Figure 2.3.** Schematic diagram of a Scanning Electron Microscope (SEM). (Adapted from Flewitt, P. E. J.; Wild, R. K. Physical Methods for Materials Characterization. Chapter 6, *Inst. of Physics Pub. Inc.* **1994**, Bristol).

A resolution up to 0.7nm – 5nm can be achieved by using SEM. The imaging of individual atoms is not possible with the help of a SEM as the area of the spot exposed to the electron beam and the interaction volume are both larger than the distance between individual atoms.

### 2.3.2. Transmission Electron Microscopy (TEM)

Transmission electron microscope (TEM) operates on the same basic principles as that of the optical microscope but uses electrons instead of light. [51, 52] The transmission electron microscope is a very powerful tool for analysis in material science. As TEMs uses electrons for imaging purpose and the wavelength of electrons are much shorter than that of light waves, a resolution obtained for a TEM is at least thousand times better than that for an optical microscope. TEM can reveal the finest details of the internal structure of a material-even able to image individual atoms. However, since the transmitted electrons are used for creating the images, morphological details are less prominent in the TEM images. It is possible to even observe molecules of the order of a few angstroms ($10^{-10}$ m). It has been shown that by increasing the potential between the anode and the cathode, one can generate fast electron beams that can probe individual atoms and the technique has helped us a lot in understanding the fine-structure of materials. The achievability of very high magnifications has made the TEM a powerful tool in materials research.

A high energy beam of electrons from the electron gun is made to focus on a small spot on the sample under analysis by the use of the

condenser lens. The electron beam then passes through the electromagnetic objective lens which focuses the electrons scattered from the specimen into one point on the image plane. The interactions between the electrons and the atoms are observed to deduce the structural features in the material. As the electrons are passing through the sample, they get scattered by the electrostatic potential set up by the constituent elements in the specimen. A portion of the beam is transmitted depending upon the thickness and electron transparency of the specimen.

This transmitted part is then focused by the use of an objective lens into an image on a phosphorescent screen. When the beam strikes the screen, phosphorescent light is produced, allowing us to observe the image. The brighter areas in the image indicate those areas of the sample where more electrons are transmitted through while the darker areas represent those areas where fewer electrons are transmitted. High resolution TEM is widely used to analyze the size, shape, quality and density of quantum wells, wires and dots. A TEM specimen must be thin enough to transmit sufficient electrons to get an image with sufficient signal intensity.

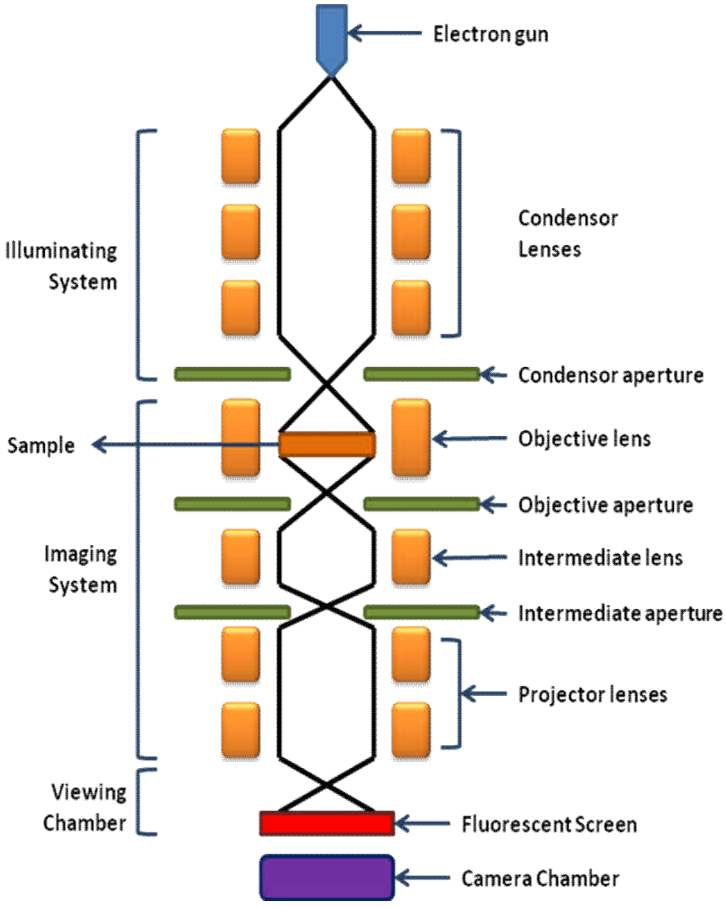


**Figure 2.4.** Schematic diagram of a Transmission Electron Microscope (TEM). (Adapted from Brydson, R.; Brown, A.; Benning, L. G. et al. Analytical transmission electron microscopy. *Reviews in Mineralogy and Geochemistry*, **2014**, 78 (1), 219 – 26, ISSN 1529-6466).

## 2.4. UV-Vis Absorption Spectroscopy

Several materials exhibit resonant absorption of light in the Visible and Ultraviolet region of the electromagnetic spectra, corresponding to the energy gaps between the various electronic states

in the system under study. In the UV-Visible absorption spectrometer, the response of a sample towards ultraviolet and visible range of electromagnetic radiation is measured. [53, 54] According to the Beer-Lambert Law, the absorbance of a sample is directly proportional to the concentration of the solution and the path length (thickness) of the medium, as stated by Beer-Lamberts law. This law can be expressed mathematically as

$$A = \varepsilon c l$$

Where **A** is the absorbance, **ε** is the molar absorption co-efficient, **c** is the concentration of the solution and **l** is the path length of the medium. Absorption of light in the UV-Visible part of the spectrum (210 – 900 nm) is measured. Transitions between electronic energy levels results in the absorption of electromagnetic radiation in this region of the spectrum. Mostly, these correspond to transitions of electrons from the highest occupied molecular orbital (HOMO) to the lowest occupied molecular orbital (LUMO).

In the case of metal and alloy nanoparticles, UV-Visible absorption spectra are routinely used to characterize these particles based on the resonant absorption of light corresponding to the Localized Surface Plasmon Resonance (LSPR) of colloidal metal nanoparticles. In the case of colloidal Au, Ag, Cu nanoparticles, the SPR absorption occurs in the visible region. The position and shape of the SPR bands provides us information about the size, shape, composition of the particles as given by Mie Theory and other theories.

Typically, the Au NPs give rise to SPR absorption around 520 nm and Ag NPs around 400 nm. The SPR absorptions corresponding to the AuAg Alloy NPs lie in between those for Ag NP and Au NP, and one observes a linear correlation between $\lambda_{max}$ and the alloy composition. Most of the phenomenon associated with the nanoparticles such as inter particle association, networking, amalgamation, etc can be can be monitored in terms of the variation in $\lambda_{max}$, since it is directly linked to the surface electronic structure of the particle.

The width and shape of the peaks also give information about the microstructure of the specimen as a result of the direct correlation between the electronic relaxation and the bandwidths. The Full Width at Half maximum (FWHM) of the peak is indicative of the high micro-heterogeneity of the substrate as a result of relaxation processes. The resolving power depends on the wave length of source and the best resolution achievable will be equal to half of the wave length of source used. The absorption spectra of all the samples are measured using Jasco-V 550 UV-Visible Spectrophotometer.

## 2.5. FTIR and Raman Spectroscopy

Both IR and Raman spectroscopic techniques are based on the quantization of the energies of molecular vibrations. Molecules undergo vibrational motions absorbing characteristic energies in the infrared region. Infrared spectroscopy deals with the resonant absorption of IR radiation causing characteristic excitations between the ground and excited vibrational states. [55-57] Since the different

vibrational modes of the same molecule absorbs at different energies, one obtains a spectrum of absorbed radiations. IR spectra are routinely used in the structural elucidation to find the functional groups present in a molecule. The spectrum is obtained by passing infrared radiation through the sample and measuring the amount of the incident radiation absorbed at that particular energy. IR spectrum of a chemical species provides the finger print of a molecule for its structural identification as it unravels the presence of the different functional moieties present in that molecule. With advent of Michelson's interferometer and Fourier transformation, recording of IR spectrum is made much simpler by the evolution of FT IR spectrometer. The Raman Effect was discovered by the great scientist C. V. Raman in the year 1928 and was awarded Nobel Prize for the same in the year 1930. [58]

Raman spectroscopy is fundamentally very different from the IR spectroscopy. The former is based on the inelastic scattering of light after interacting with the molecules, unlike the resonant absorption in the IR spectroscopy. The radiations, in general, undergo two types of scattering -the elastic and the inelastic. In elastic scattering (Rayleigh scattering), the scattered radiation will have the same energy as compared to the incident radiation. On the other hand, in the case of inelastic scattering (Raman scattering), the scattered radiation will have an energy different from that of the incident radiation. This difference amounts to the energy given by the molecule to the radiation (anti-Stokes) or the energy taken up by the molecule (Stokes). Thus the Stokes lines will always have lower energy than the incident radiation

while the anti-Stokes lines will have a higher energy than the incident radiation.

The population of the vibrational energy states is governed by the Boltzmann distribution and so at low temperatures, most of the molecules will be occupying the ground vibrational states and only a small fraction of the total number of molecules will be occupying higher vibrational energy states. Thus, the anti-Stokes lines will be rather weak as compared to the Stokes lines. Also, the Raman scattering cross section is very small as compared to the Rayleigh scattering. Statistically, only one out of 100 molecules will undergo Raman scattering.

### 2.5.1. Surface-enhanced Raman Spectroscopy (SERS)

Raman spectroscopy is a very powerful tool in the structural elucidation of molecules and the group theoretical selection rules makes Raman spectra complementary to the IR spectroscopy. Raman and IR spectra together will be able to explain molecular structure in great detail. Since water is a poor scatterer of light, Raman spectroscopy can be a powerful to probe bio-molecular structure in functional forms. However, due to the poor signal intensities, it has not been able to utilize this method in its full capabilities. However, it was observed that when molecules get adsorbed on roughened metallic surfaces or metal nanoparticles, the Raman signal intensities get enhanced by a factor of approximately $10^6$ (even more in the case of molecules that give Resonance Raman effect), and that this can overcome the poor Raman cross section. [59]

Such large enhancement of Raman signals on metal nanoparticle surfaces is called Surface Enhanced Raman Spectroscopy (SERS) and this has been of tremendous use in lifting the Raman signal intensities of important bio-molecules. A schematic description of SERS enhancement has been presented in Figure 2. 5.

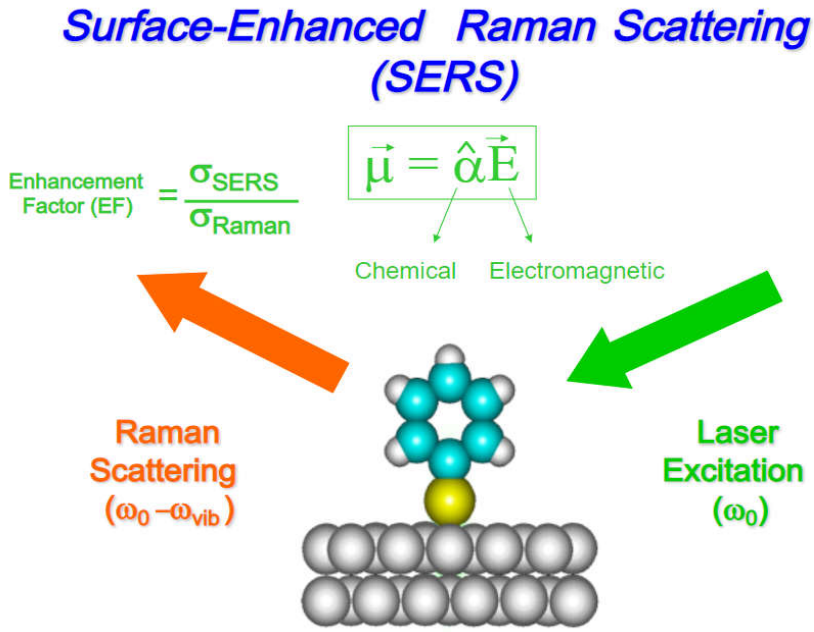


**Figure 2.5.** Schematic illustration of signal enhancement in SERS. (Adapted from Haynes, C. L.; McFarland, A. D.; Van Duyne, R. P. Surface-Enhanced Raman Spectroscopy. *Anal. Chem.* **2005**, 77(17), 338 A-346 A).

The quantum mechanical operator in a Raman scattering process is the induced dipole moment, **μ**, given by

$$\mu = \alpha E,$$

Where **α** is the polarizability tensor and **E** is the local electric field experienced by the molecule. When a molecule is adsorbed on the surface of metal nanoparticles, the electric field of the radiations gets enhanced by the resonant, in-phase oscillation of the electrons on the nanoparticles. This type of enhancement is usually termed as the Classical Electro-magnetic Enhancement (CEME) and this can give an enhancement by a factor of $10^6$. Also of interest is the Chemical Enhancement, generally caused by the transient excitation of some of the excited metal electrons into the molecular orbitals of the adsorbed molecular system.

CHAPTER 3

# A SIMPLE ANTI-SOLVENT METHOD FOR THE CONTROLLED DEPOSITION OF METAL AND ALLOY NANOPARTICLES

## 3.1. Introduction

As discussed in Chapter 1, Surface Plasmon absorptions from metal and alloy nanoparticles have attracted volumes of work in the past two decades due to unique colours of the nanoparticles as well as the close correlation of these colours to their surface electronic structures. [60-66] Not only that these colours have generated considerable interest from a basic science perspective to manipulate the optical properties of metal nanoparticles, it has also led to the development of important applications in physics, materials science, optics, biology, and medicine. As discussed earlier, much of the original reasoning for the colours of the noble metal nanoparticles have been linked to the Mie theory. [67]

In later years, many theoretical simulation methods based on Mie theory, discrete dipole approximation (DDA), and finite difference time domain (FDTD) have been developed to model the Plasmon behaviour in nanoparticles of complex shape, geometry, and composition. [68-70] Applications of metal nanoparticles in applications such as sensing, catalysis, and targeted drug delivery are of special importance in advanced functional materials. Also, arrays of metal nanoparticles encapsulated in silica matrices and the like have found immense applications in the development of optical limiters. Studies on LSPR has also led to the opening of several new horizons for the development of a wide range of applications in ultrasensitive chemical and biological sensing by virtue of the advanced techniques such as

Plasmon Resonance Sensing, Surface-enhanced Raman Scattering (SERS) and Surface-enhanced Fluorescence (SEF). [71-76]

Since the LSPR has been attributed to the resonant optical absorptions due to the collective oscillations of the polarisable surface electrons of the metal nanoparticles, in tune with the oscillating electric field of the incident electromagnetic radiation, any modification in the surface electronic structure will be reflected in the position ($\lambda_{max}$) as well as the line shape of the absorption band.

In fact, Plasmonics has now been developed into a full-fledged discipline in physics and materials science. It is also established that one can tune the colour of the nanoparticles or the surface Plasmon absorption maximum (λmax) by the preparation of alloy nanoparticles of various metals by modifying their compositions.18-20 For example, in the case of Au-Ag alloy nanoparticles, it is possible to tune the plasmon absorptions of alloy nanoparticles between that for pure Au and that for pure Ag, and that the λmax varies quite linearly with composition. These materials have significant interest in Plasmonics. Of particular interest is SERS which enables the vibrational spectroscopic detection of molecules at very low concentrations allowing us to overcome normally weak Raman cross-section. [77, 78]

One important challenge in enabling all these applications is the development of a strategy for the controlled deposition of such nanoparticles of metals on various substrates in sufficiently large concentrations, but without leading to the normal aggregation and the

resulting inter-plasmonic coupling, eventually leading to the shifting, broadening or even the loss of the LSPR. These noble metal nanoparticle surfaces can serve as good SERS substrates.SERS is attributed to both the enhancement of the local electric field of the electromagnetic radiation on the nanoparticle surface as well as the possible chemical enhancement effects due to potential, transient, electron transfer from the metal nanoparticles to the vacant anti-bonding orbitals of the analyte molecules.

The normally weak Raman cross-section is overcomed by a million-time enhancement brought in at the metal nanoparticle surface by the two established mechanisms, viz., the Classical Electromagnetic Enhancement (CEME) and the Chemical Enhancement. While CEME is directly related to the local amplification of the local electric field experienced by the molecule at the metal nanoparticle surface by the oscillation of the surface electrons, Chemical effect arises from the change in polarizability of the molecule by virtue of the charge-transfer or what is generally described as the chemical effects between the nanoparticle surface and the molecule.

It has been reported that these two mechanisms together can cause an enhancement of $10^6$ times in the Raman signal intensity. Often, coupled with Resonance Raman effects, this can go up to the tune of $10^{12}$ times and can lead the way to single molecule detection of important bio-molecules. Plasmonics also supports sensing applications such as the naked eye-detection of toxic metal ions such

as $Hg^{2+}$ at low concentrations without the use of any sophisticated equipment.

In this Chapter, we present a simple strategy for the controlled deposition of metal and alloy nanoparticles based on preferential solvation, guided by the competitive intermolecular interactions in a micro-heterogeneous environment created by different liquid molecules. Aqueous dispersions of starch-stabilized Au, Ag, and Au-Ag alloy nanoparticles of different compositions were prepared and these were deposited on to a Whatman filter paper by the controlled drop-wise addition of acetone to the dispersion. The preferred acetone-water interactions and the poor solubility of starch in acetone presumably reduce the stabilization of the starch-stabilized metal/alloy nanoparticle resulting in the slow precipitation of the nanoparticles. Such two-dimensional nanoparticle arrays will greatly help to enable the plasmonic applications to more precise optical applications. It is demonstrated that these two-dimensional arrays can act as good platforms for carrying out SERS studies taking 1,4-Benzene dithiol as a model molecular system.

### 3.1.1. Controlled Deposition of Metal and Alloy Nanoparticles

Anti-solvent precipitation, also referred as de-solvation consists in drawing-out precipitation or solvent displacement and is achieved by decreasing the stability of a solute in a solvent in which it is dissolved. This method has received much attention as simple physical chemistry tool for the precipitation of many solutes in a controlled way

often leading to the crystallization of many systems that are otherwise difficult to crystallize. In addition to liquids, gases such as $CO_2$ have been used for the purpose in simple gaseous state as well as supercritical states.

One can consider a solution as a two-component system consisting solute and the solvent. The solute is dissolved in the solvent by virtue of either site-specific solute-solvent interactions such as in the case of polar solvents like water or simple dispersive forces like the van-der-Waal's forces as in the case of non-polar solutes and non-polar solvents. The rule of thumb in such cases is described as "the like dissolves the like". For example, in the case of solvation of $Na^+Cl^-$ crystals in water, the lattice energy of the solute crystal is replaced by the favorable solvation of the individual $Na^+$ and the $Cl^-$ ions by the surrounding water molecules, which are held together by the cooperative networks of hydrogen bonds. The Oxygen atoms of the water molecules are oriented towards the $Na^+$ ions to ensure the required charge stabilization in the primary solvation process. But, in the case of the $Cl^-$ ions, the primary solvation shell consists of the partially positive hydrogen atoms of the water molecule orienting towards the $Cl^-$ ions. The complex cooperative networks of the hydrogen bonds of water will then govern the primary, secondary, tertiary, and higher order solvation shells, eventually the bulk water structures.

In fact, the water molecules in each one of these solvation shells are different from spectroscopic perspective consisting different

degrees of polarization. Even the charge densities on the ions can have profound effect on the solvation. For example, the $Ag^+$ ion, which has a lower charge density as compared to that the $Na^+$ ion (by virtue of the larger size of the former), gets solvated more effectively in organic solvents such as Acetonitrile (AcN).

In the case of simple hydroxyl systems such as sugars, the hydrogen bonding between the hydroxyl groups of the solute and the solvent water molecules ensure their solvation in water. A third solvent (or third component) which has a high interaction cross-section and higher miscibility with the solvent molecules (second component) that are solvating the solute molecules (first component), preferential solvation effects begin to be operational. If the interaction between the third component and the second component outweighs the interaction between the first and the second components, the molecules of the second component will be drawn away from the first component, eventually leading to the precipitation of the first component out of the solution. The strength of the interaction between the individual solute ions/molecules will also have a crucial role here. The larger the interaction cross-section, the easier would be the precipitation of the first component.

Although this is strictly an issue of preferential solvation, often it is termed as anti-solvent as the first component gets thrown out of the solution by the addition of the third component. Thus, the term anti-solvent is used very often. The term coacervation is also used to describe this process. Anti-solvent precipitation is also be achieved by

the addition of a non-solvent to a solution in order to induce super-saturation and solute precipitation. Careful and proper selection of the solvent and anti-solvent is important. There must be high affinity between the solvent and anti solvent or at least they need to be miscible over the concentration range at which they will be used for the process of nanoparticles by precipitation.

During anti-solvent precipitation, there occurs the competition of molecular interactions between solute, solvent, and anti-solvent. These interactions lead to the precipitation of particles. At this point, the solute-solute interactions will become large enough to overcome the solvation and lead to the precipitation of the solvated species. The entropy of mixing will be high that point. It may also be perceived that the addition of the anti-solvent to the solution decreases the solvent power leading to the process of supersaturation. When the concentration of the solute becomes greater than the equilibrium saturation concentration of that particular solvent/anti-solvent mixture, the system becomes supersaturated. And above a specific critical supersaturation concentration, nucleation is induced. The time lag between the starting of supersaturation and the onset of nucleation is known as the induction time. [36]

There will be a metastable zone in which no nucleation is observed within a given time range for a particular solvent/anti-solvent composition. The metastable zone is narrow if high and homogeneous nucleation rates are observed. Anti solvent precipitation is commonly used for the preparation of micro- and nano- sized materials especially

used to make drugs in the pharmaceutical industry. The physical and chemical properties of an antisolvent can change the rate of mixing with the solutions and hence the rate of nucleation and precipitation are all influenced. One of the drawbacks of this method is the difficulty in controlling the size of the particles produced after precipitation, usually a rapid growth rate can be observed in certain situations, which leads to a broad particle size distribution. Since the process is thermodynamically controlled, the energy requirements are minimized in this process.

## 3.2. Experimental

The nanoparticles of Au, Ag, and Au-Ag nanoparticles are prepared by a variant of the green chemistry method described earlier using β-D Glucose as the reducing agent and soluble starch as the protecting agent. [79, 80] About 10 ml 0.05 N aqueous solution of D-Glucose was taken in a beaker and 20 ml of 1% aqueous starch solution was added to it. To this mixture, an aqueous solution of $HAuCl_4$ (0.01N, 500μL) was added and is heated to boiling in a microwave oven. Then 200 μL of 0.01 N NaOH is added to increase to pH. The appearance of ruby red color indicates the formation of Au NPs. Ag NPs and AuAg alloy NPs are also synthesized by the same method by taking required stoichiometric amounts of the individual metal precursors.

The metal precursors, viz., $AgNO_3$ (Extra pure 99.9%) and $HAuCl_4$ (purity ≥99.9%), as well AR grade β-D Glucose (the reducing

agent) and Soluble Starch (extra pure AR) were purchased from Sigma Aldrich. AR grade acetone was used for the deposition of the nanoparticles from various dispersions. UV-Vis Absorption spectra were recorded using a JASCO Model V550 spectrometer fitted with accessories for solid state measurements. High resolution FESEM images were obtained using Hitachi S-4800 Model High Resolution Field Emission Electron Microscope. Controlled deposition of metal and alloy nanoparticles were carried out by the preferential solvation method by the drop-wise, slow addition of Acetone from a burette to the aqueous dispersion of the nanoparticles.

### 3.3. Results and Discussion

We have carried out the controlled precipitation of the nanoparticles of Au, Ag, and the AuAg alloy nanoparticles of various compositions as shown below. The colloidal metal nanoparticle, which is stabilized by the soluble starch molecules and these starch-stabilized metal and alloy nanoparticles are stabilized in water as a colloidal dispersion, plausibly by virtue of the hydrogen bonding between the starch molecules and water. The photographic images of the aqueous dispersions of Au, Ag, and Au-Ag alloy nanoparticles prepared as mentioned above are presented in Figure 3.1.

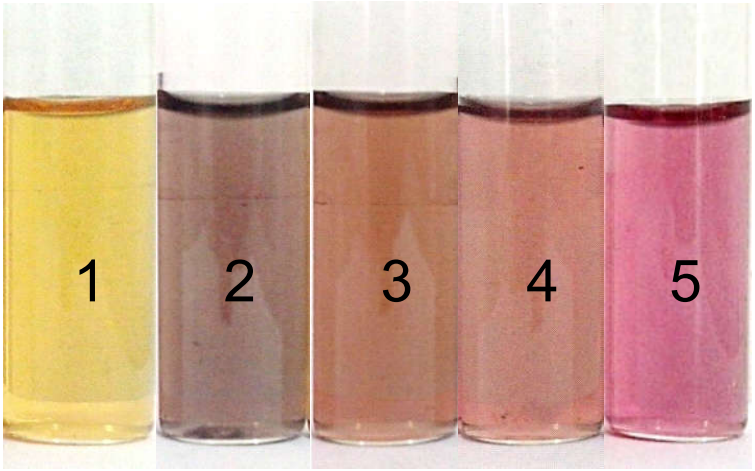


**Figure 3.1**. (a) Photographic images of aqueous dispersions of (1)Ag NP; Ag:Au alloys of the compositions (2)3:7 Alloy, (3)5:5 Alloy, (4)7:3 Alloy and (5)Au NP.

One can clearly observe the variation of the colour from that of pure Au and Ag nanoparticles indicating the formation of the alloys.

### 3.3.1. UV-Visible Spectra

The UV-Vis absorption spectra of these metal and alloy nanodispersions are presented in Figure 3.2.

A plot of $\lambda_{max}$ against the composition and the UV-Vis absorption spectra of these dispersions are presented in figures 1(b) and 1(c), respectively. It is observed that the $\lambda_{max}$ varies linearly with composition indicating the formation of the alloys as against core-shell particles.

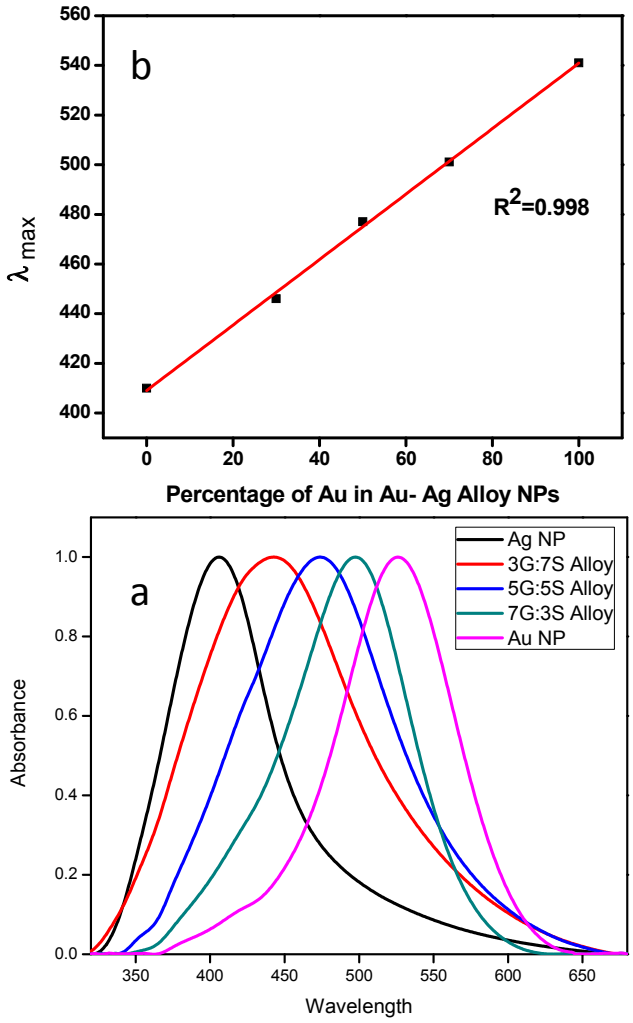


**Figure 3.2.** (a) UV-Vis absorption spectra of the aqueous dispersions of Ag NP; Ag:Au alloys of the different compositions mentioned in Figure 3.1. (b) Plot of $\lambda_{max}$ Vs percentage of Au in the nanoparticle for the various compositions.

### 3.3.2. TEM Analysis

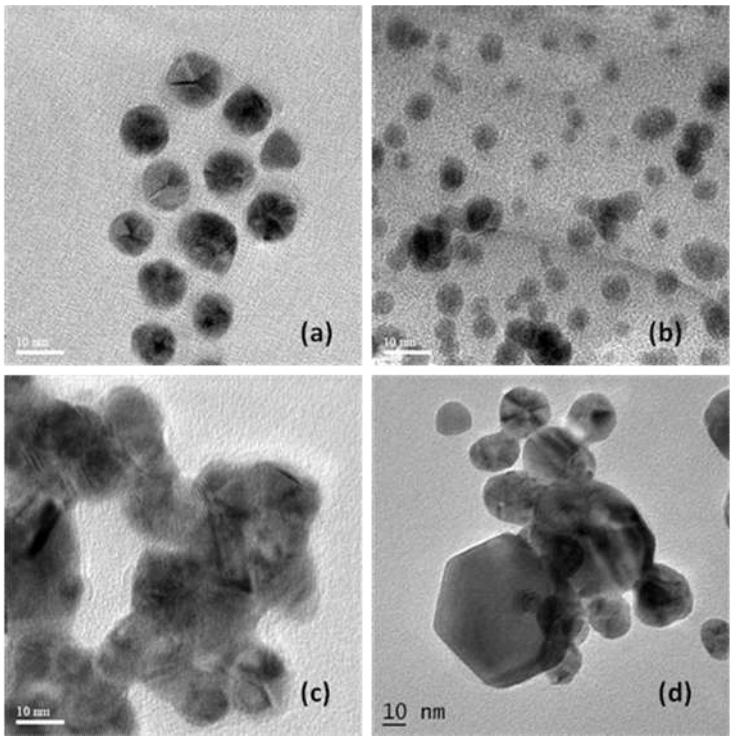


**Figure 3.3.** The High Resolution-TEM images of colloidal nanoparticles drawn on a TEM grid (a) Au NPs, (b) 7:3AuAg Alloy nanoparticles, (c) 3:7 AuAg Alloy nanoparticles and (d) Ag NPs.

Gold nanoparticles have an average size around 10-20 nm and are all spherical in nature. Silver nanoparticles shows varying size ranging from 10-100 nm Also we can find hexagonal nanoparticles in addition to spherical ones. Intermediate alloy nanoparticles have smaller size than the individual gold and silver nanoparticles. But on drying, they are found to aggregate slightly as evident from the TEM

images given below. This may because of their higher surface reactivity on account of their smaller size and higher microheterogeneity.

The method can be adopted for the easy synthesis of Au, Ag, and Au-Ag nanoparticles of desired $\lambda_{max}$ by employing suitable stoichiometric compositions of the precursor metal ions. These stable dispersions were then transferred to glass beakers containing cellulose paper at the bottom. As discussed in the introduction, acetone was added through the sides of the beaker slowly from a burette to allow the slow and controlled deposition of the metal and alloy nanoparticles.

It is seen that the particles fall out of the dispersion and slowly deposit at the bottom on the paper placed for the purpose, as evidenced by the reduction in the colour of the aqueous dispersion. The deposition of the nanoparticle on the Whatman paper is found to be uniform as evident from the thickness measurements. A digital micrometer screw gauge was employed to measure the thickness of the sample. Bare Whatman filter paper has thickness 0.187 ± 0.001 mm, for the nanogold deposited film, it is 0.2 ± 0.001 mm and for silver nano film, it is 0.211 ± 0.002. The variation is too small of the order of ±0.001 and ±0.002 mm. The proposed mechanism of the deposition is shown schematically in Figure 3.4.

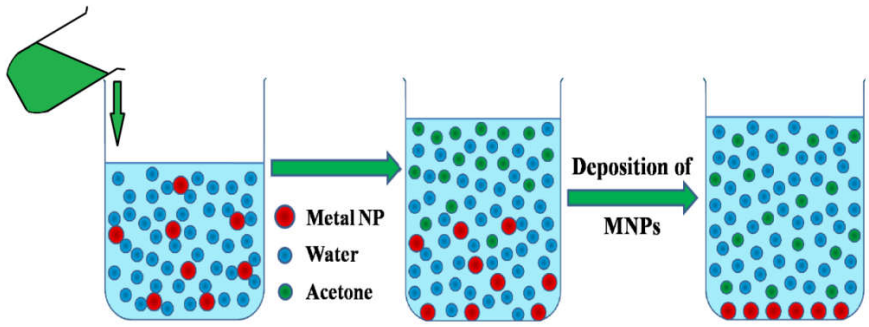


**Figure. 3.4.** Cartoon depicting the plausible mechanism of acetone-mediated deposition of the starch-stabilized metal or alloy nanoparticle from the respective aqueous dispersions.

The starch stabilized metal or alloy nanoparticles are stabilized in water; solvated by the cooperative networks of hydrogen bonds between starch and the various solvation shells of water around the nanoparticle. Upon the addition of acetone, there comes a competitive interplay between the water-acetone and the water-starch interactions. [81, 82] It is well-established that even in the apparently homogeneous mixtures of liquids such as water and acetone there are different regions in the phase diagram dominated by different types of interactions and exhibit microscopic heterogeneity in the different compositions.

For example, vibrational and NMR relaxation studies by Reimers and Wallen, respectively, had demonstrated a water-rich region, acetone rich region and a region where there is a competitive interplay between the various acetone-water structure. From a similar standpoint, we perceive that in the present scenario, there is a competitive set of two interactions. The starch-water solute-solvent

interaction is sufficiently strong to stabilize the starch-stabilized metal nanoparticles in water. However, upon the addition of acetone, the acetone-water interactions become dominant enough to push out the metal nanoparticles from the dispersion eventually leading to their controlled deposition. The clear aqueous part was then drained and the cellulose papers were dried at room temperature. Photographic images of the cellulose papers deposited with the Au, Ag, and Au-Ag alloy nanoparticles of different compositions as well as their corresponding Diffuse reflectance UV-Vis spectra are presented in Figure 3.5.

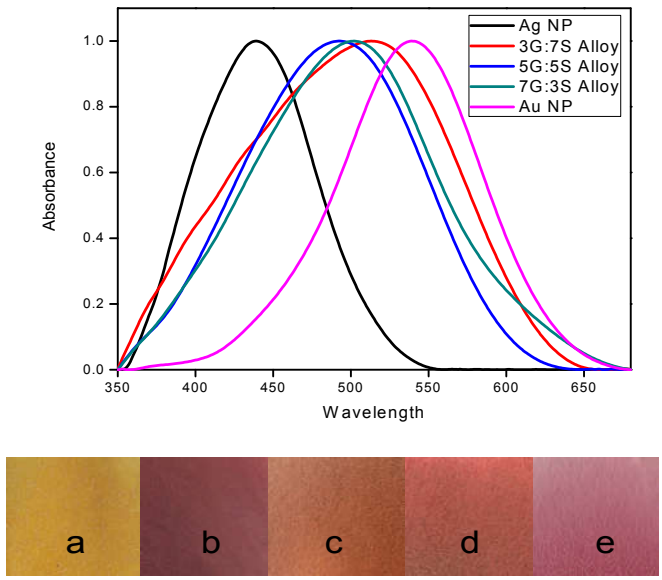


**Figure 3.5.** Photographic images of the cellulose papers deposited with various metal and alloy nanoparticles: (a) Ag; (b) AgAu (7:3); (c) AgAu (5:5); (d) AgAu (3:7); and (e) Au. The corresponding diffuse reflectance UV-Vis absorption spectra are presented above.

### 3.3.3. FE-SEM Analysis of 2D MNP arrays

High resolution FE-SEM images at different magnifications of a typical bed of Ag nanoparticles deposited on a cellulose paper are presented in Figure 3.6.

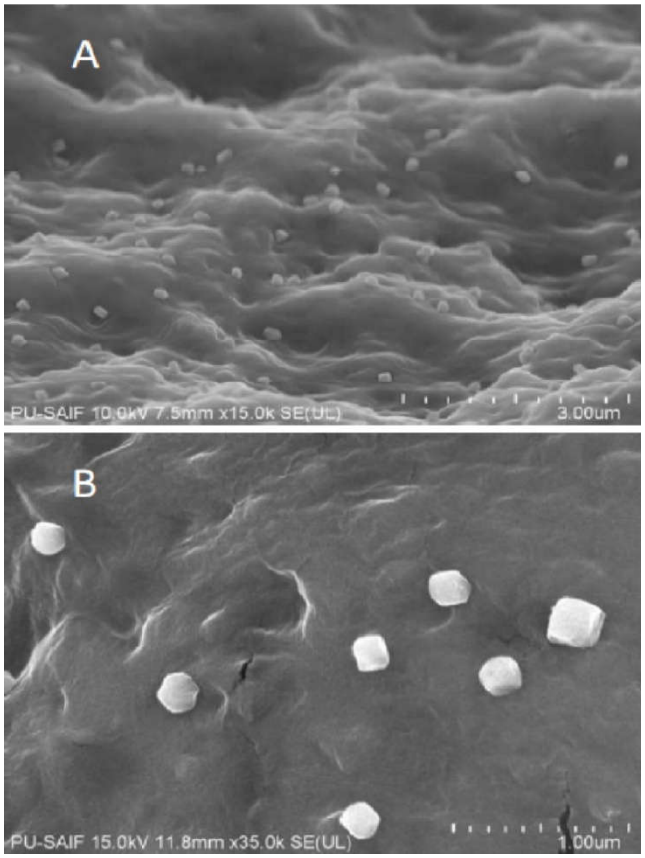


**Figure 3.6.** (a), (b), & (c) Field-emission SEM images of the Ag NP film at different magnifications.

One can observe a bed of well-separated Ag nanoparticles, mostly cubes with an average size of 200 nm in such a way that there is no aggregation or possible inter-plasmonic coupling. In comparison

with the earlier reported work, the sizes of the nanoparticles are at least an order of magnitude higher (ref), plausibly formed by the Ostwald-type ripening of the nanoparticles upon treatment with acetone. This is also evidenced by the red-shift of the $\lambda_{max}$ values for the films as compared to those of the corresponding aqueous dispersions.

## 3.4. Applications

### 3.4.1. Surface Enhanced Raman Spectroscopy

There are several applications for such nanoscale assembles of metal nanoparticles, particularly in sensing. Among such methods, of special significance is the substrates for the surface enhanced Raman spectroscopic detection of molecules at low concentration wherein one overcomes the disadvantage of the low Raman scattering cross section (and thus low intensity of the peaks) facilitated by the enhancement of the local electric field experienced by the molecules at the metal nanoparticle surface. The SERS spectra of one of the typical compounds, Benzene Dithiol (BDT) recorded on Ag, Au and the various AuAg (1:1) alloy particle assemblies at a low concentration of $10^{-3}$ M are presented in Figure 3.7.

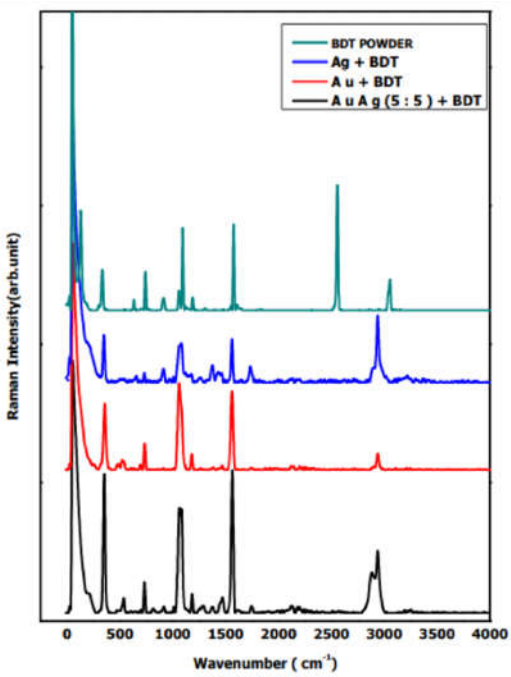


**Figure 3.7.** (A)FT Raman spectrum of BDT (powder); (B), (C), (D) Fourier transform SERS spectra of BDT on two-dimensional beds of Ag, Au, and AuAg (5:5) alloy nanoparticles.

Electrons have different vibrational levels defined by specific energy differences. When an incident monochromatic light interacts with an electron in the sample, the electron absorbs energy from the incident photon and rises to a virtual state of energy. The energy transferred is given by the formula E= hν. The electron then falls back to an energy level by losing energy. If the energy lost is equal to that of the energy of incident photon, the electron falls back to its initial vibrational level and in this process emits another photon. Energy lost is equivalent to the energy of incident photon; the released photon has same frequency as that of the incident photon giving rise to Rayleigh

scattering. Sometimes, the electron, when losing energy from the virtual state can fall back to a different vibrational level. As a result, the photon emitted by the electron has energy different than the incident photon. Depending upon the final energy of the electron or final vibrational level of electron, Raman scattering is separated into stokes and anti-stokes lines.

A Raman spectrum gives the molecular fingerprint and it is different for different molecules. By studying the spectra, one can identify rotational levels and thus image a particular molecule. This helps in performing qualitative analysis. Intensity value of a particular Raman line helps to determine the concentration of a molecule in a given sample. So it is ascertained that Raman spectroscopy is an excellent tool for both Qualitative and Quantitative analysis. Raman spectroscopy has several disadvantages such as low sensitivity when the sample volume is low or when the concentration of Raman active molecules is less. When that molecule is placed in the vicinity of a nano roughened noble metal surface, the intensity of Raman scattering is found to be enhanced tremendously.

The FT-SERS spectrum of BDT recorded on the various substrates demonstrate significant SERS enhancements enabling their detection at low concentrations. Electromagnetic enhancement model suggests that the vibrational modes that are parallel to the surface will not be enhanced while those modes that are perpendicular to the surface will be enhanced. Since the aromatic C-H stretching vibrations are absent, one might assume that the benzene ring is oriented parallel to the metal nanoparticle surface. Also, the absence of the S-H stretch

mode around 2510 $cm^{-1}$ is indicative that the formation of the Au-S or Ag-S bonds by the elimination of hydrogen at the metal nanoparticle surface. All the other peaks of BDT are present in the spectrum with good signal to noise ratios. One of the most interesting features observed is the variations in the relative intensities of the various peaks in the spectra obtained on different substrates, which could be due to the differences in the fine structures of the nanoparticle surfaces and specific adsorbate metal/alloy interactions.. Although such intensity variations have been obtained earlier for the spectra for the same substrate with different excitation lines, in this case, it is the same excitation line in the NIR range (1064 nm) gives such intensity variations for different $\lambda_{max}$ values of the substrates. The exact reasons for such variations would provide more insights into the mechanism [83, 84] of SERS itself.

## 3.5. Conclusions

Plasmonics of metal and alloy nanoparticles is an important field in physics and chemistry of materials with potential applications in sensing. Preparation of two-dimensional arrays of metal/alloy nanoparticles of noble metals without causing aggregation and consequent inter-plasmonic coupling is an important aspect for enabling such applications. In the present work, we have presented a very simple, anti-solvent approach for the preparation of such two-dimensional arrays of noble metal and alloy nanoparticles and have demonstrated that these substrates could be used as effective SERS substrates.

# CHAPTER 4
# PLASMONIC SENSING OF Hg (II) IONS USING GOLD, SILVER AND GOLD-SILVER ALLOY NANOPARTICLES

## Contents

## 4.1. Introduction

Heavy metal toxicity has been proven to be a major threat to human health and environment. They can adversely affect human body and its proper functioning, may even interfere with metabolic processes even though they do not have any biological role. [85] This is because they can act as a pseudo element of the body. Some heavy metals get accumulated in the body through food chain, showing a chronic nature leading to several disorders and also results in excessive damage due to the oxidative stress induced by free radical formation. [86] Mercury is considered to be the most toxic among heavy metals. [87, 88]

Mercury poisoning is also known as *acrodynia* or pink disease. Mercury is extensively used for making thermometers, barometers, hydrometers, pyrometers, fluorescent lamps and mercury arc lamps. It is also used in various industries such as pharmaceuticals, pulp and paper industries, agriculture industry, chlorine and caustic soda production industry. Major sources of mercury pollution are anthropogenic activities such as agriculture, mining, incineration, municipal waste water discharges, and industrial waste water.

Mercury exists mainly in three forms: metallic elements, inorganic salts and organic compounds. Exposure to elevated levels of mercury can damage the brain, kidneys and the developing fetus. Inorganic mercury has the ability to combine with other elements forming amalgam and also can easily convert into organic forms of mercury. Micro-organisms convert mercury present in soil and water

into methyl mercury, a well known potent neurotoxin. Organic mercury has the ability to penetrate biological membranes as they are lipophilic in nature making them more hazardous. [89]

It can easily pass through the placental membrane and the blood-brain barrier making even slightest exposure during pregnancy to be a great concern. The nervous system is very sensitive to all types of mercury. Mercury can impair any organ and lead to the malfunctioning of nerves, kidneys and muscles, brain being the major target organ. [90] It can also cause disruption of the membrane, potential interrupting the intracellular calcium homeostasis. Mercury can easily bind to freely available thiols as the stability constants are high. Mercury vapor inhalation can cause bronchitis, asthma and several respiratory diseases. The inorganic form of mercury, mercuric ion ($Hg^{2+}$), being highly water soluble, exists mostly in the surface water, making it more hazardous than other forms of mercury. [91]

In order to determine the mercury content in a water sample, several methods can be adopted such as Atomic Absorption/Emission Spectroscopy(AAS/AES), [92] Cold Vapor Atomic Absorption Spectroscopy (CVAAS), [93, 94] Electro-chemiluminescence, [95] Cyclic Voltammetry [96], Atomic Emission Spectroscopy, Atomic Fluorescence Spectrometry (AFS), Inductively Coupled Plasma - Mass Spectrometry (ICP-MS) and Reverse-phase High-performance Liquid Chromatography.

Even though they are powerful techniques for the trace determination of $Hg^{2+}$, they require costly instruments, sample preparation, help of a highly experienced personnel, and may often encounter interferences from other metal ions, making the selective detection rather difficult. So the development of an inexpensive, simple and direct method for the sensing mercury becomes necessary. For over 2500 years noble metals had been extracted, based on the knowledge that mercury forms an amalgam with such noble metals. It is well understood that mercury has an affinity towards noble metals such as gold and silver in the bulk state. Hence, noble metal nanoparticles can also be used as a good probe for the easy and sensitive detection of Hg (II) ions. It is found that noble metal nanoparticles are excellent sensors of $Hg^{2+}$ ions due to the modification of surface electronic structure and thereby the plasmonic properties of metal nanoparticles upon amalgamation. They can detect even trace amounts of mercury as dissolved salts in water samples.

As discussed in the previous chapter, the characteristic colours of the metal nanoparticles are caused by typical optical absorptions due to their distinct surface plasmon resonance (SPR) absorptions in the visible region of the electromagnetic spectrum, resulting from the collective oscillations of the surface electrons of the metal nanoparticles with respect to the oscillating electric field of the incident radiation. The $\lambda_{max}$ of absorption is characteristic of different metals and that the magnitude of absorption is proportional to $R^3$. The

wavelength at which the NP absorbs depends on several factors such as size, shape, composition and local environment.

Upon adsorption of mercury, the complex dielectric function of metal NPs gets altered resulting in a blue-shift in the LSPR wavelength. The Hg (II) ions get reduced to Hg(0) and will cover the surface of the metal nanoparticles and as time goes, some of the Hg atoms will diffuse into the metal lattice.

## 4.2. Experimental

The synthesis of Au, Ag and AuAg Alloy nanoparticles were carried out by adopting the procedure discussed in the previous chapter in section 3.2.

## 4.3. Results and Discussion

### 4.3.1. Sensing of Hg(II) ions using Noble metal NPs

Detection of Hg (II) ion by using Ag NPs as probe is based on the blue-shift of the $\lambda_{max}$ of the surface Plasmon absorption upon amalgamation. The spectra of Ag NPs give a $\lambda_{max}$ value around 400 nm, which gets blue-shifted from the visible to the UV-region of the electromagnetic spectrum upon the addition of Hg (II) ions to the Ag NP dispersion. Visibly, the colour of the Ag NP dispersion gradually changes from yellow to colourless. The intensity of the optical absorption is also found to decrease with increasing mercury concentration. There are two important processes which require consideration in this context.

The first is the modification of the plasmonic structure around the nanoparticle as a result of the incorporation of the Hg atoms in place of the host noble metal lattice (often truncated). The latter is the process of diffusion, wherein the Hg atoms diffuse through the noble metal lattice modifying the dielectric function of the nanoparticle. Both these processes can directly alter the surface Plasmon absorptions and the $\lambda_{max}$ values as described by the Mie theory and its extensions. This is also true for the bimetallic systems such as AuAg alloy nanoparticles wherein one can tune the $\lambda_{max}$ values based on the composition of the alloy nanoparticles.

It may be noted that the atomic radii (calculated) of Ag and Au atoms are 1.65 Å and 1.74 Å, respectively. This also suggests that there will be significant disorder in the AuAg alloy nanoparticle, originating from the size difference between the two atoms. The atomic size of Hg(0) is 1.71 Å indicating that Hg atoms too can easily diffuse into Au, Ag, or the AuAg alloy organizations. It may also be noted that the lattice energy of the Hg is rather low as evidenced by its existence as a liquid at room temperature, in sharp contrast to the other metals. Such an incorporation of Hg atoms can lead to a change in the dielectric behavior as well as surface electronic structure of the Au, Ag, and the alloy nanoparticle, leading to the modification of the wavelength of their surface Plasmon absorptions.

In a typical experiment as shown in Figure 4.1, when a drop of a solution containing Hg (II) ion is added into a dispersion of Ag NPs prepared by the glucose reduction, the colour of the Ag NP dispersion

changes from yellow to colourless. The spectra of Ag NPs give a maximum absorption peak at around 402 nm, which gets blue shifted upon the addition of Hg (II) solution.

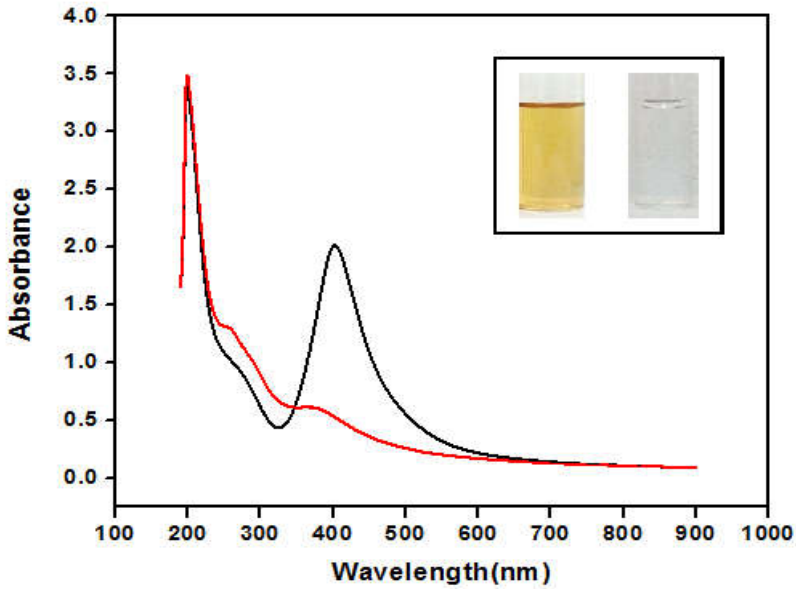


**Figure 4.1.** The UV-Vis spectra of colloidal Ag NPs showing a $\lambda_{max}$ at 402 nm (Black line) and that after amalgamation (Red line).

Similar experiment was carried out with a dispersion of Au NPs, which absorption peak is ruby red in colour and one observes a colour change from ruby red to orange yellow, qualitatively, upon the addition of a few drops of Hg(II) ion. The characteristic $\lambda_{max}$ of 530 nm obtained for the Au NP dispersion is blue-shifted to 493 nm. The UV-Visible absorption spectra corresponding to the Au NP dispersions before and after the addition Hg (II) ions are presented in Figure 4.2.

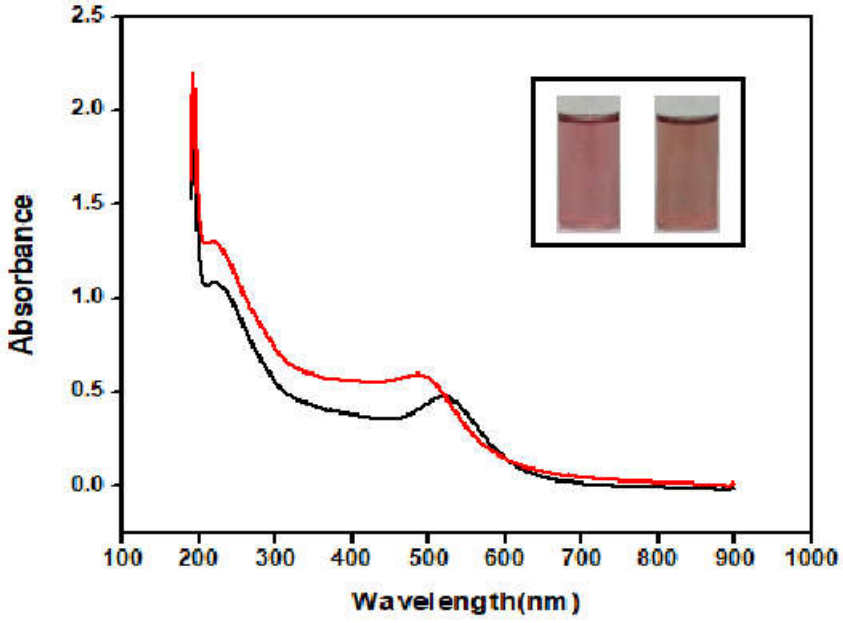


**Figure 4.2.** UV-Vis spectra of colloidal Au NPs showing $\lambda_{max}$ at 530 nm (Black line) and that after amalgamation having $\lambda_{max}$ at 493nm (Red line).

### 4.3.2 Spot Test

Even though there is a clear blue shift for the $\lambda_{max}$ of both the Au and Ag NPs, it is observed that the colour change cannot be demarcated by the naked eye in the case of the AuNP dispersion because the blue-shifted absorption is still in the visible region of the spectrum. On the other hand, the bright yellow colour of Ag NPs will vanish or completely shift from the Visible to the UV region upon upon treatment with mercury, enabling the use of Ag NP dispersion an ideal candidate as a sensor for the naked eye detection of Hg (II) ion and thus, ideal for the Thus it also becomes a spot test identification

of detection of Hg (II) ions by a spot test. Although there are many sophisticated instrumental methods for the analysis and estimation of various metal ions in solutions containing mixture of metal ions, it is highly desirable to have simple and novel experimental methods for their *in-situ* identification and confirmation in the qualitative inorganic analysis. Since the preparation of Ag NP dispersion is a simple and straightforward one-step process that can be carried out in any simple chemistry lab, such spot test detection can find useful for the detection or confirmation of Hg (II) ion in the undergraduate labs. [97-107]

It is also important that spot test should be highly selective and specific to a particular metal ion. In many cases, such spot tests can even serve as simple and low-cost methods for the *in-situ*, naked eye detection of metal ions at low concentrations for a range of applications including the testing for toxic metal ions in drinking water. [108-110] The spot test for Hg(II) ions is also highly useful in providing a classic, class room example for how surface Plasmon absorption from metal nanoparticles can serve as in important tool for sensing and for explaining how the Plasmon absorption gets modified by changes in the surface electronic structure of metal NPs.

#### 4.3.2.1. TEM Analysis

The high resolution TEM image of the Ag NPs synthesized using glucose reduction is given below. The image confirms the formation of Ag NPs with average particle size ranging from 20-40 nm.

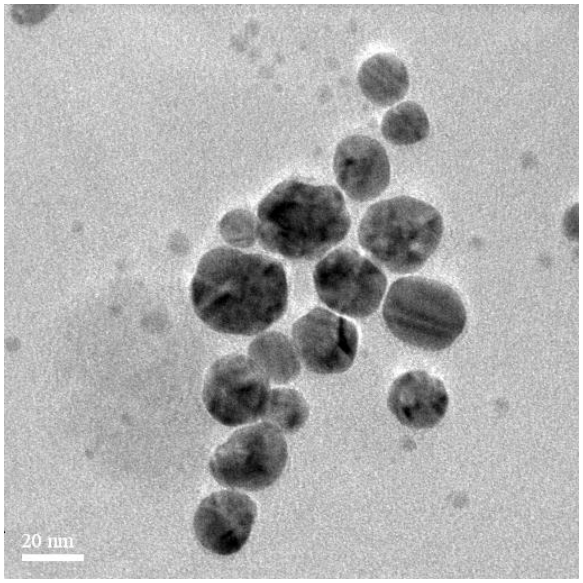


**Figure 4.3:** High-resolution TEM image of the Ag nanoparticles formed.

This spot test identification is highly cost effective and simple. An added advantage is that the synthesized Ag NPs can be preserved in the laboratory for 4-5 months without affecting the sensitivity of the experiment. In addition to the possibility of the glucose reduction of Hg (II) ions, it is also believed that two silver atoms react with one mercuric ion, which carries a two-fold positive charge, to produce two silver ions, which go into solution, and a neutral mercury atom, which is taken up by the metallic silver particles. [111]

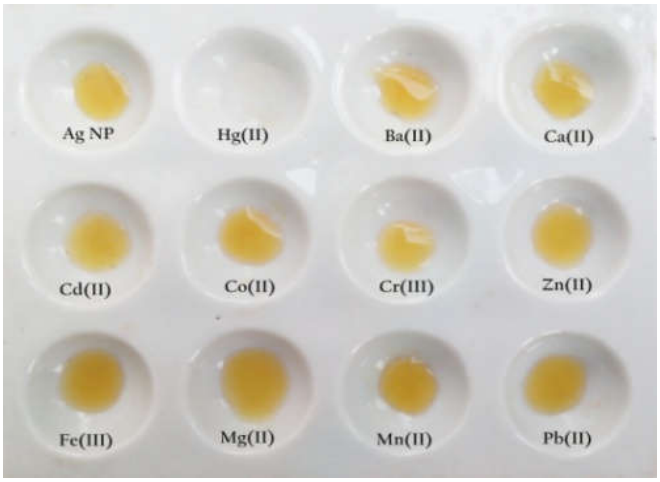


**Figure 4.4:** Optical response of the aqueous dispersion of Ag NPs with the various metal ions.

The as-prepared colloidal suspension of Ag NPs (4mL) was treated with one drop of Hg(II) ions ($10^{-3}$N). The optical response was noticed. The experiment was repeated to quantify the response of Hg(II) ions with Ag NPs by taking Hg(II) ion solutions in the concentration the range $2.4 \times 10^{-5}$ to $2 \times 10^{-4}$ mol/L. It was noticed that even a minimum concentration of $1.11 \times 10^{-4}$ mol/L of Hg(II) is sufficient to cause complete disappearance of the yellow colour of Ag NPs. The as-prepared colloidal suspension of Ag NPs (1 or 2 drop) was taken in one trough in a spot plate, and to this bright yellow dispersion, a drop of Hg(II) ion solution was added and it was observed that the yellow colour of the Ag NPs vanished almost instantaneously.

The selectivity of the method towards the sensing of Hg (II) ions, experiments were also carried out with different metal ions. The

possibility of interference from other metal ions or masking is also investigated. The photographic image of Ag NPs treated with common interfering ions is given below.

To this objective, the same experiment was carried out with different common metal ions such as Mg(II), Cu(II), Fe(II), Ba(II), Cd(II), Pb(II), Cr(III), Co(II), Mn(II), Zn(II) and Ca(II). None of the above metal ions showed a colour change as observed in the case of Hg(II), ensures the selectivity of Ag NPs to Hg(II) ion demonstrating its reliability as a characteristic tool for the spot test of Hg(II) ion. [112-115]

The intensity of the Plasmon absorption is also found to decrease with increasing mercury concentration. [116] The blue shift was in proportion with the Hg (II) concentration over the range from $2.4 \times 10^{-5}$ to $2 \times 10^{-4}$ mol/L. The characteristic peak was found to become broadened and red shifted when other cations were used instead of Hg (II). When Hg (II) ion was added to the colloidal Ag NPs solution, the excess glucose present in the colloidal Ag NPs solution reduces Hg (II) ions to Hg (0) atoms. As formed Hg (0) atoms tend to wrap around Ag NPs to form amalgam which absorb at a lower wavelength leading to a blue shift in the absorption spectrum.

### 4.3.3. Mercury detection using Ag NP Strip

From an operational point of view, it could be even more advantageous to prepare plasmonic paper strips tethered with Ag nanoparticles. This is particularly so in the case of the detection of

Hg(II) ions in water sources to ascertain the safety of drinking that water. For this purpose, we have prepared Ag NP strips which can be directly dipped in water. The strategy for the preparation of of Ag NP strip using the anti-solvent precipitation of the Ag NPs on to the Whatman filter paper is explained in chapter 3. These strips also found application for detecting mercuric ions. The preparation of Ag NP strip involves introduction of 10ml of acetone into Ag NP dispersion prepared as above. Acetone-water interaction is greater than water- Ag NP interaction, so that acetone pulls out water molecules causing the Ag NPs to settle down. These nanoparticles can be uniformly coated onto a membrane filter to form a thin layer simply by filtration of the nanoparticle dispersion. It is then dried well and can be used as test strip for detecting mercuric ions. The Field emission SEM image of the paper strip deposited with Ag NPs was presented in Figure 4.5. We can clearly see cubical nanoparticles with an average particle size around 200 nm.

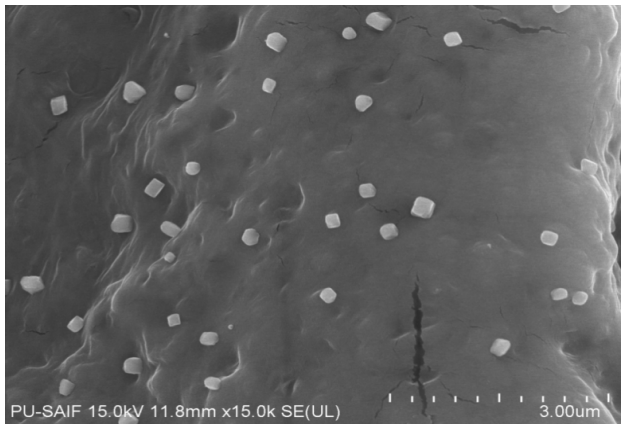


**Figure 4.5.** FE-SEM image of deposited Ag nanoparticles.

The UV-Visible diffuse reflectance spectra of the strips before and after treatment with Hg (II) ions are presented in Figure 4.6. The surface plasmon absorption band showing a $\lambda_{max}$ at 421 nm clearly indicates the formation of Ag NPs. The as-prepared Ag NP test strip is then treated with Hg(II) ions ($10^{-3}$M). The optical response was noticed. The yellow colour of the test strip disappeared gradually with increasing volume of Hg(II) ion solution. The absorption intensity is also found to decrease with increasing mercury concentration. The blue shift was in proportion with the Hg (II) concentration. After some time, the peak at 421 nm gets completely disappeared and is shifted to a lower wavelength region, known as blue shift or hypsochromic shift.

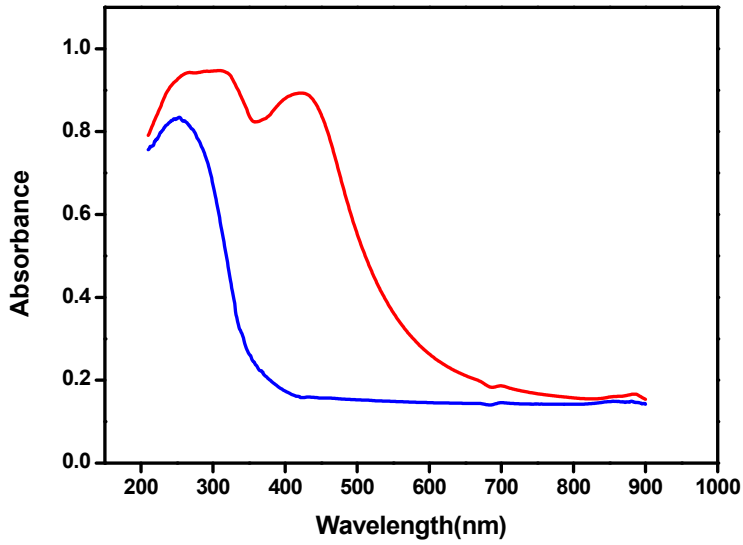


**Figure 4.6.** UV-Vis DR spectra of Ag NP test strip showing a $\lambda_{max}$ at 421 nm (Red line) and that after treatment with mercuric ions (Blue line).

To check the selectivity of Ag NP test strip towards mercuric ions, it is then treated with various common interfering metal ions such as Mg(II), Cu(II), Fe(II), Ba(II), Cd(II), Pb(II), Cr(III), Co(II), Mn(II), Zn(II) and Ca(II). The concentration of metal ions taken was $10^{-3}$ M.

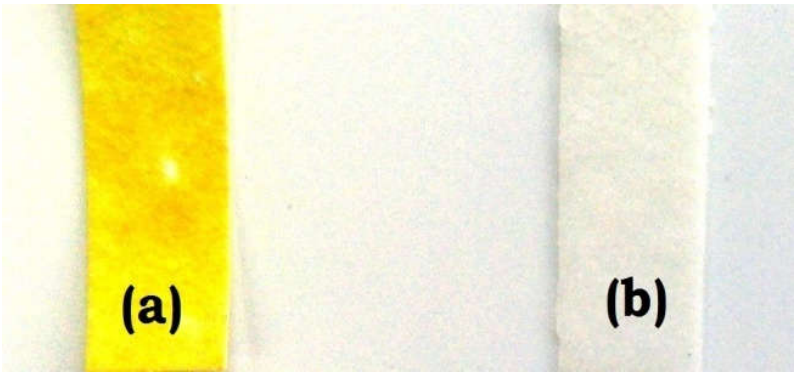


**Figure 4.7.** Ag NP test strip, (b) After treatment with $10^{-3}$ M $Hg^{2+}$.

It is found that only mercuric ions decolorize the Ag NP strip. No such colour change is observed upon treatment of the Ag NP film with other metal ions.

### 4.3.4. Spectrometric detection of Hg(II) ions using Au, Ag and AuAg alloy nanoparticles

Although Au and AuAg alloy nanoparticles do not present drastic visual changes as in the case of the Ag NPs, they show significant change in the $\lambda_{max}$ values and can be followed using spectrometric methods. As discussed in the introduction of this chapter, the alloy nanoparticles are inherently more disordered and are more amenable for the diffusion of the Hg (0) atoms and thus one can

optimize the alloy composition that provides the maximum shift in the $\lambda_{max}$ values.

The Au, Ag and Au-Ag alloy NPs of all the varying compositions were prepared using the method discussed in Chapter 2 by the co-reduction of Au(III) and Ag (I) ions to the Au (0) and Ag (0) which cluster kinetically to form the alloy structures. Since there are significant differences between the Au and Ag atoms, one could expect some sort of microscopic heterogeneity in these alloy clusters. One would expect that this can lead to modifications in the value of $\lambda_{max}$ and particularly, this can lead to interesting concentration-dependent changes with the amalgamation with Hg (0) atoms.

The effects of the modified surface electronic structure and effects due to the diffusion of the Hg (0) atoms into the interior of the disordered alloy nanoparticle lattice can be followed using the UV-Vis spectroscopy. Typically, one would expect that the introduction of Hg(0) on the surface of the alloy nanoparticles will modify surface electronic properties and reflect in a blue-shift in their SPR absorption, as observed in the case of the Ag NPs. However, with diffusion of the Hg(0) to the interior, the surface structure will have lesser number of Hg atoms and this will push the Plasmon absorption to higher wavelengths. One also needs to consider the change in the dielectric constant of the metal or alloy nanoparticle as a result of the diffusion of the Hg atoms into the host lattices. These competing effects can make the situation more complex. However, it will be intriguing to investigate these effects as a function of the Hg(0) concentrations. At lower concentrations, the first effect will be more dominant and one

would anticipate a linear dependence of $\lambda_{max}$ or with the concentration of Hg(0). A plot of $\lambda_{max}$ for Ag NPs with the concentration C in the range range from $2.4 \times 10^{-6}$ to $2.0 \times 10^{-5}$ mol/L is presented in Figure 4.8. As expected, linear relationship is observed between $\lambda_{max}$ and C.

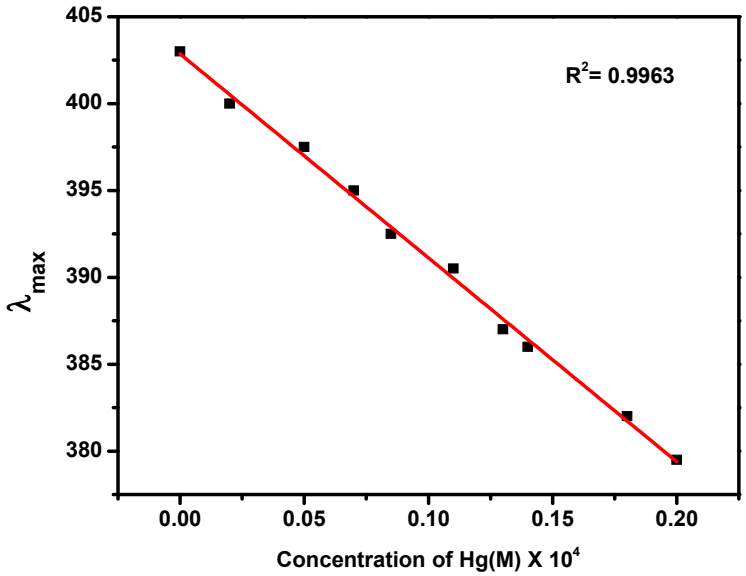


**Figure 4.8.** Linear dependence of $\lambda_{max}$ values of Ag NPs upon treatment with Hg(II) on the concentration of mercuric ions.

At higher concentrations, the linearity will be broken and one observes a maximum value for $\lambda_{max}$ above which, we observe a red-shift in the $\lambda_{max}$. The maximum blue shift occurred when the Hg (II) concentration was 6.98 X $10^{-5}$ mol/L in the case of gold and alloy NPs. Accordingly the colour change was also maximum for 6.98 X $10^{-5}$ mol/L. After that, the extent of blue shift was found to be decreased, i.e., after reaching a particular concentration of mercury, turnover is observed for the value of $\lambda_{max}$. Similar trends were observed for all the

MNPs such as Au, Ag and alloy NPs. We have plotted the $\lambda_{max}$ values of all the compositions against the mercuric ion concentration and it is given below. Plots of $\lambda_{max}$ Vs concentration of $Hg^{2+}$ ions for Ag NPs, Au NPs and Au-Ag alloy nanoparticles are presented in Figure 4.9. One observes a dependence of $\Delta\lambda_{max}$ (the difference between the $\lambda_{max}$ for the metal nanoparticle before and after treatment with Hg(II) ions) at the turnover point with the alloy composition. Also, one observes a dependence of the turnover concentration with the alloy composition.

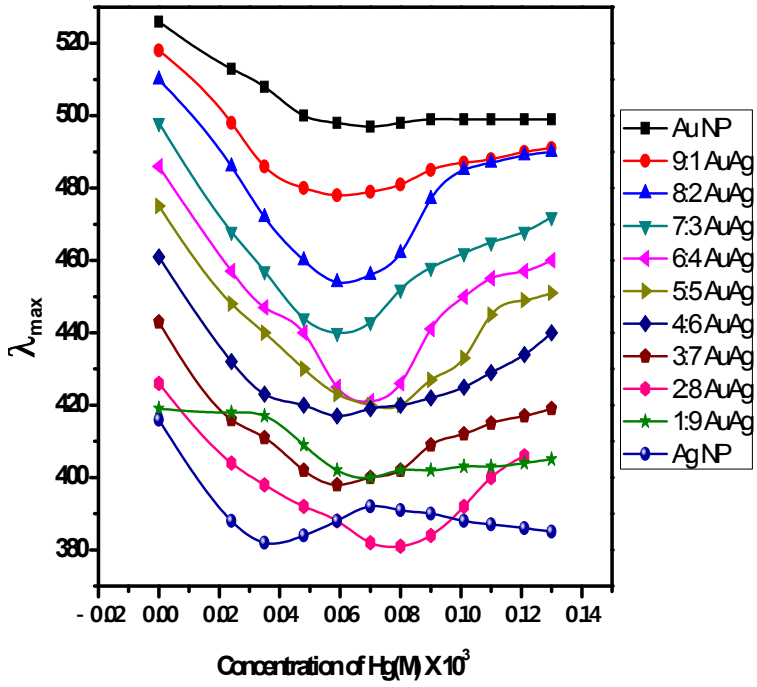


**Figure 4.9.** Plots of $\lambda_{max}$ Vs concentration of $Hg^{2+}$ ions for Ag NPs, Au NPs and Au-Ag alloy nanoparticles.

It is seen from figure 4.9 that there is a turnover concentration of Hg(II) ions, below which there is a blue shift with the concentration of Hg(II) ion and above which there is a red-shift. This can be explained by considering the mechanism as a two-step process. The first process is that the mercuric ions get wrapped around the metal nanoparticles, forming a core-shell like structure [117] and as they have totally different dielectric properties, this will lead to a blue shift in the absorption wavelength. At lower concentrations of mercury, there is more density of mercuric ions on the surface of the nanoparticles as evident from the characterization studies causing larger blue shift. [118]

In the next step, there occurs diffusion of mercuric ions into the core of the metal nanoparticle, causing less blue shift. These two competing phenomena are responsible for the crossover that we see at higher con concentrations of mercury. Especially when we take higher concentrations of mercuric ions, the diffusion process will the major contributor leading to a slight red shift. The maximum value of blue shift ($\Delta\lambda_{max}$) obtained for the different compositions are plotted in the image given below.

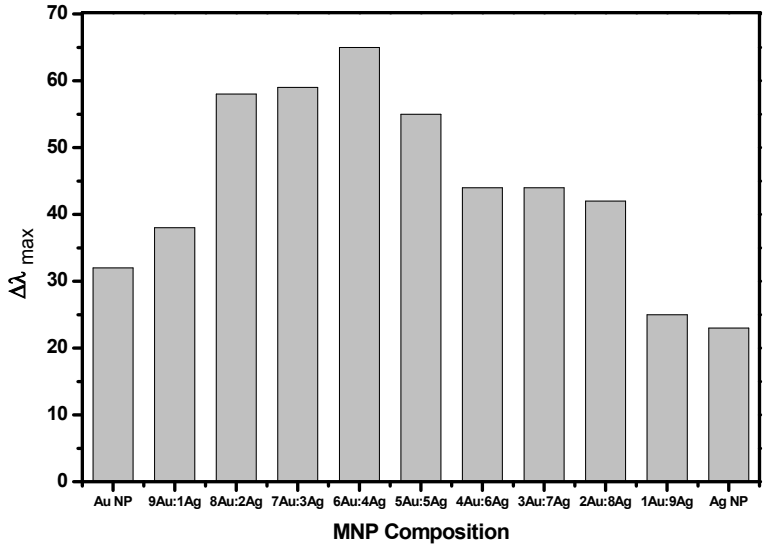


**Figure 4.10.** A histogram showing the values of Plots of $\Delta\lambda_{max}$ vs. concentration of $Hg^{2+}$ ions for Ag NPs, Au NPs and Au-Ag alloy nanoparticles.

From Figure 4.10, it is seen that that 3:2 (Au:Ag) alloy nanoparticles show the maximum value for $\Delta\lambda_{max}$ indicating that these systems will be superior systems for the spectrophotometric detection of Hg (II) ions. This could be due to higher degree of microheterogeneity for this alloy composition.

### 4.3.5. Interference studies with common metal ions

The photographic images of the silver, gold and 3:2 AuAg alloy nanoparticles treated with common ions is shown in the figure given below.

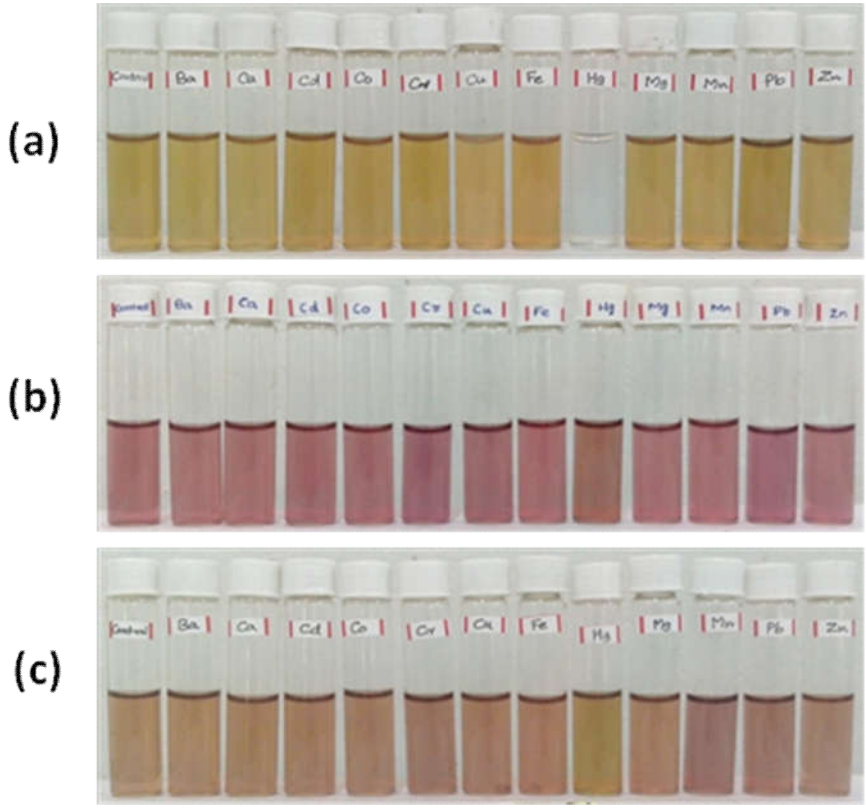


**Figure 4.11.** (a) Colour change of Ag NPs in the presence of various metal ions. (b) Colour change of Au NPs in the presence of various metal ions and (c) Colour change of 3Au:2Ag NPs in the presence of various metal ions. Only $Hg^{2+}$ is found to give blue shift of the maximum absorption peak.

Noble metal nanoparticles are found to be extremely selective towards mercury and hence they can be considered as a better candidate for mercury detection and no other common metal ions are found to interfere in the process and the selectivity profile diagram is provided in the figures given below.

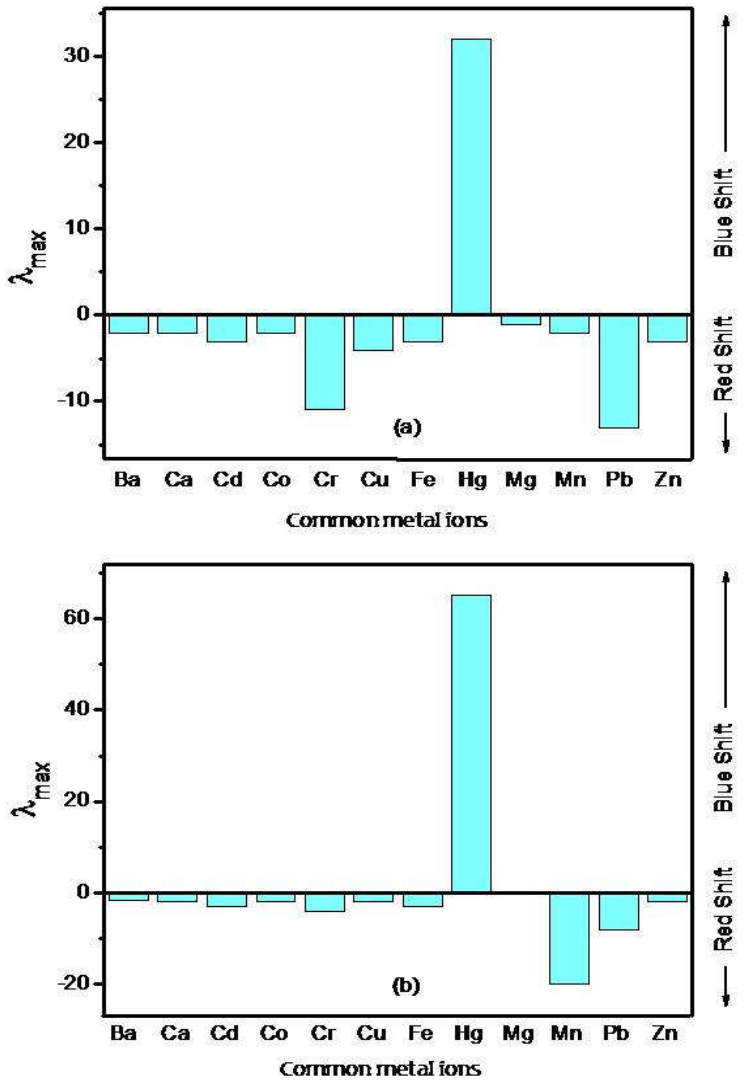


**Figure 4.12.** Selectivity of mercury over other common metal ions upon the amalgamation of (a) Gold nanoparticles and (b) 3Au:2Ag alloy nanoparticles. The concentration of metal ions used here is 6.98 $\times 10^{-5}$ mol/L.

Surprisingly the alloy composition 3Au: 2Ag give maximum shift of the absorption peak up to 65 nm. The colour change was from brown to yellow and can be easily detected with the naked eye, although the contrast is not as good as in the case of the Ag NPs. The other alloy compositions give intermediate results. Thus, it may be inferred that the alloy composition 3Au: 2Ag is the most suitable alloy composition for the photometric sensing of Hg (II) ions. While Au and Ag NPs give the $\Delta\lambda_{max}$ values of 32 nm and 23 nm respectively, the 3:2 AuAg composition gives a $\Delta\lambda_{max}$ of 65 nm.

Although it was found that 3:2 AuAg is better towards mercury sensing on account of the higher $\Delta\lambda_{max}$, a UV-Visible spectrophotometer is required for the detection and is not that easily detectable with naked eye when compared to the colour contrast that is achieved with Ag NPs.

### 4.3.6. The Influence of pH

In order to investigate the influence of pH on the sensing ability of the various metal and alloy nanoparticle substrates, we carried out the above experiment at various pH values ranging from 4 to 10 and the absorption peak was taken. It was found that the optical response was highly dependent on the pH of the solution. By using the *K*sp of $Hg(OH)_2$, it was calculated that the deposition of Hg(II) would occur when the pH becomes higher than 6.24. Generally amalgamation is favoured when the pH becomes greater than 7(at the basic condition). The extent of blue shift increases with increase in the pH.

But the disappearance of yellow colour of Ag NPs upon treatment with Hg(II) was most prominent at lower pH indicating that lower pH would be ideal for spot tests. However, the Ag NPs have higher tendency to go into solution as $Ag^+$ ions (unlike Au NPs). [Hg(II)] ions have higher reduction potential(+0.85 V) than the $Ag^+$ ions(+0.80 V), resulting in the conversion of Ag NPs into $Ag^+$ ions, thus going into solution. So, practically, neutral pH would be more suitable for the spot test. [119]

## 4.4. Conclusions

Metal nanoparticles act as a good probe for the selective sensing of mercury as they are able to shift the LSPR towards higher wavelength region upon amalgamation. We propose a simple, cost effective and highly selective spot test for Hg (II) ion by using starch stabilized aqueous colloidal Ag NPs prepared via green methodology. The spot test can be used for sensing trace amounts of mercury content in water samples. The method was efficient to detect even $1.11 \times 10^{-6}$ mol/L of Hg (II) content. Since Ag NPs show a drastic color change from bright yellow to colorless, this could serve as a probe for the naked eye detection of Hg (II) ions as well as the substrate for spot tests for the selective detection of Hg (II) ions. We can also use Ag NP dispersions as well as papers tethered with Ag NPs for the Sensing of Hg (II ions). AuAg alloy NPs with a composition 3:2 atomic ratio show presents the best values for $\Delta\lambda_{max}$ suggesting that these systems will be the most suitable for the spectrophotometric detection of Hg (II) ion.

# CHAPTER 5
# PLASMONIC SENSING OF HYDROGEN PEROXIDE USING COPPER@GRAPHENE OXIDE NANOCOMPOSITES

## Contents

## 5.1. Introduction

Carbon nano-structures have been one of the most involved research areas in nanoscience and technology in the past two decades. Although the structure-property correlations for graphite and diamond had been one of the most fascinating aspects of structural chemistry and physical chemistry, it was the discovery of fullerenes and their derivatives that revolutionized the interest in the Carbon chemistry. [120-123]

The bucky ball ($C_{60}$) was one of the most fascinating structures created by the scientists. Afterwards, the discovery of carbon nanotubes and graphene generated much interest in the carbon chemistry and gave birth to many advanced functional materials. Graphene is in fact planar two-dimensional molecule with all $sp^2$ carbon atoms that forms a single layer of graphite. These nanostructures of carbon, often coupled with hetero atoms, form structurally and functionally important nano systems such as graphene oxide(GO), Graphene, carbon dots, fullerenes etc with applications in diverse fields such as molecular sensing, medicine, drug delivery, advanced catalysis, photo voltaic devices, etc. [124, 125]

Graphene consists of a two-dimensional, single layer of $sp^2$ hybridized carbon atoms. It is found to possess various unique properties owing to their high specific surface area; high sorption capacity and large delocalized pi-electron system which can easily form bonds with benzene ring system. [126] Due to the lack of functional

groups on the surface of the graphene, the interaction with metal ions is poor.

Graphene oxide(GO), the precursor of graphene, on the other hand, bears several oxygen-bearing functional groups on its hexagonal two dimensional carbon network which makes it highly hydrophilic in nature. [127] It is highly dispersible in water. The presence of oxygen allows them to show both electrostatic and co-ordinate interaction with several metal ions. This property makes it suitable for chemical and biological sensing. GO nanosheets are employed to disperse and stabilize nanoparticles, which is possible due to the surface functional moieties (–OH, C–O–C, and –COOH) on GO that acts as the reactive sites for the nucleation and binding of metal nanoparticles. GO sheets, exfoliated from graphite oxide, bears enormous number of oxygenated functional groups such as epoxy, hydroxyl and carboxyl groups. [128-132]

There is abundant number of literatures about the applications of carbon based materials in diverse fields. Carbon based nanoscale building blocks such as nanotube, graphene oxide, graphene etc possesses high surface area, mechanical strength, electrical conductivity, biocompatibility and low cost of preparation. Graphene oxide (GO), is the oxidized form of graphene with disorder on the basal planes and edges in its two dimensional hexagonal structure. [133] The presence of covalent oxygen functional groups provides high mechanical strength and also molecular-level chemical sensing capability.

These functional groups are better sites for the growth of inorganic nano-structures. Carbon based nanostructures decorated with metal nanoparticles are better for several applications and some may even possess novel properties than the individual particles. The tuning of size, morphology, and dispersity of the NPs could be more effective when GO sheets are used as support. The GO sheets with large specific surface area provide more sites for the nanoparticles to form. The Ag@GO composites have been vastly reported for the past few years, and have been found to possess interesting applications compared with free Ag NPs. [134-40] GO nanosheets loaded with Ag NPs can be synthesized by adopting various methods such as pulsed, microwave, and sonication methods. [141]

In recent years, copper nanoparticles have gained increased attention due to their interesting properties and low cost of preparation. It finds application in Catalysis, conductive inks and sensing applications. The possibility of utilizing the Cu nanoparticles for the detection of Hydrogen Peroxide ($H_2O_2$) is presented in Chapter 5. Copper nanoparticles are reported for the optical sensing of hydrogen peroxide. Hydrogen peroxide will oxidize $Cu^0$ onto $Cu^{2+}$ and it will go into the solution and as a result the reddish brown copper nanoparticle colloid will get decolorized. [142]

Hydrogen peroxide sensing using bare Cu NPs is not reliable as any disturbance that will destabilize the $Cu^0$ such as even a pH change can decolorize the solution. We tried to incorporate copper nanoparticles onto graphene oxide to synthesize hybrid nanomaterial

and checked whether it is showing any enhanced sensing capability towards hydrogen peroxide. Hydrogen peroxide ($H_2O_2$) is the simplest peroxide, which is miscible with water and is widely used as an oxidizer, bleaching agent and an antiseptic. The peroxide ion will cause the oxidation of proteins, membrane lipids and DNA. [143]

Hydrogen peroxide toxicity is via three main mechanisms: corrosive damage, oxygen gas formation and lipid peroxidation. Exposure to concentrated $H_2O_2$ may result in local tissue damage as it is a well known caustic. [144] Therefore fast and reliable detection of $H_2O_2$ at ultra trace level is of great importance. There are some papers describing the usage of noble metal nanoparticles, mainly silver NPs for the colorimetric sensing of $H_2O_2$. [145-49] It was found that Cu NPs and carbon nanoparticles decorated with Cu NPs are highly efficient for the detection of hydrogen peroxide. But all of them are electrochemical sensors. [150-56]

In this paper we present a low-cost facile approach for synthesizing copper-graphene oxide nanocomposite (Cu@GO) and its application towards the optical sensing of $H_2O_2$. As Ag@GO possesses interesting applications in sensing, we tried to incorporate copper nanoparticles onto graphene oxide and studied its applications towards sensing. From our studies, Cu@GO composite is found to be an excellent colorimetric sensor for sensing highly reactive oxygen species such as hydrogen peroxide. The Cu@GO dispersion was prepared by reducing copper (II) sulphate using sodium borohydride in presence of GO, under ultrasonication. Ascorbic acid is used as the

stabilizing agent. $NaBH_4$ reduces $Cu^{2+}$ into $Cu^0$ which is then stabilized by the functional groups present in GO. The color changes from light brown into dark olive green. The formation of copper nanoparticles protected by GO was confirmed by the characteristic surface plasmon resonance (SPR) band at 598 nm in the UV-Vis absorption spectrum. Copper nanoparticles synthesized in the absence of GO shows an absorption peak at 567 nm. [157-58]

We are mainly relying on the shift in the SPR of Cu@GO dispersion upon treatment with $H_2O_2$ for detecting its presence in the sample. The fabricated materials were further characterized using scanning electron microscopy (SEM), energy-dispersive X-ray analysis (EDAX) and Fourier transform infrared spectroscopy (FT-IR). The FE-SEM images showed that the synthesized Cu@GO nanocomposite were spherical in shape with size ranging from 50nm to 80 nm. After the addition of $H_2O_2$ into the Cu@GO, the peak at 598 nm is found to disappear and a new peak emerges at 388 nm, which becomes more intense with higher $H_2O_2$ concentrations.

## 5.2. Experimental

### 5.2.1. Chemicals and materials

Chemical reagents Copper Sulphate ($CuSO_4$), Graphite flakes, Sulphuric Acid ($H_2SO_4$, 98%), Potassium Permanganate ($KMnO_4$, 99.9%), Phosphoric acid ($H_3PO_4$, 85%) and Hydrogen Peroxide ($H_2O_2$, 30%) were purchased from Merck. L(+)-Ascorbic acid (AA) was purchased from Sisco Research Laboratories, Sodium Borohydride

($NaBH_4$) is from Sigma-Aldrich. All the chemicals used were of analytical grade and used without further purification.

### 5.2.2. Preparation of Cu@GO Nanocomposite

The preparation method of Cu@GO nanocomposite was as follows. Initially, GO was prepared by modified Hummer's method. [159] About 3 mg of GO was dispersed in 10 mL of DI water using a sonicator at 50 W in a RB flask. Then, added 500 µl of $CuSO_4$ (0.01 N) and 500 µl 0.01N Ascorbic acid to the above solution and is sonicated again for another 10 min. After that, 500 µl of 5 mM freshly prepared sodium borohydride ($NaBH_4$) solution was added to the $CuSO_4$-GO mixture. The colour of the solution initially changes to blackish brown, then into olive green. Sonication is continued for another 10 more minutes to ensure complete reduction of $Cu^{2+}$ into $Cu^0$.

Cu NPs are synthesized by adopting the same method, but without the addition of GO.

### 5.2.3. Instrumentation

A bath sonicator operating at (500 W, 50 Hz) was used for synthesizing Cu@GO Composite. Absorption spectra were measured by using V-550 JASCO UV–Visible spectrophotometer. The FT-IR measurements were carried out in JASCO FT-IR 4100 model. A drop of the sample was put in a transparent KBr pellet and allowed to dry. Then the spectrum was recorded in the transmittance mode as a function of the wave number ranging from 400 to 4000 $cm^{-1}$. High

resolution scanning electron microscopy (FE-SEM) images were obtained from a CARL ZEISS GEMINI FE-SEM 300, operating at 200 kV. For this, 10 μL of the sample solution was dropped on a glass plate and allowed to dry and the scanning microscopic image is recorded. The EDAX analysis was obtained using AMETEK Octane Plus model. The FT-IR spectra were collected using Jasco FT/IR-4100 model.

## 5.3. Results and Discussion

### 5.3.1. Characterization of Cu-GO Composite

#### 5.3.1.1. Optical studies:

The formation of copper nanoparticles can be observed visually as it gives a dark reddish-brown color. The Cu@GO composite is found to appear as an Olive green solution. The surface plasmon resonance peak of Cu@GO Nanocomposite was at 598 nm, whereas that of copper nanoparticles synthesized without GO has SPR at around 567 nm and has a reddish brown color.

#### 5.3.1.2. UV-Vis Spectroscopy:

The absorbance of the sample solution was measured using a Jasco V-550 UV-Vis spectrophotometer with de-ionized water as the reference over the range of 300 to 900 nm. The UV-Visible spectroscopy of Cu NPs shows a surface plasmon resonance pear at around 567 nm and appears brown in color. But, in the case of

Cu@GO composite, there is a SPR peak at 598 nm and it appears as olive green in colour.

The UV-Visible spectra of Cu NPs and CU@GO composite are given in the figure 5.1.

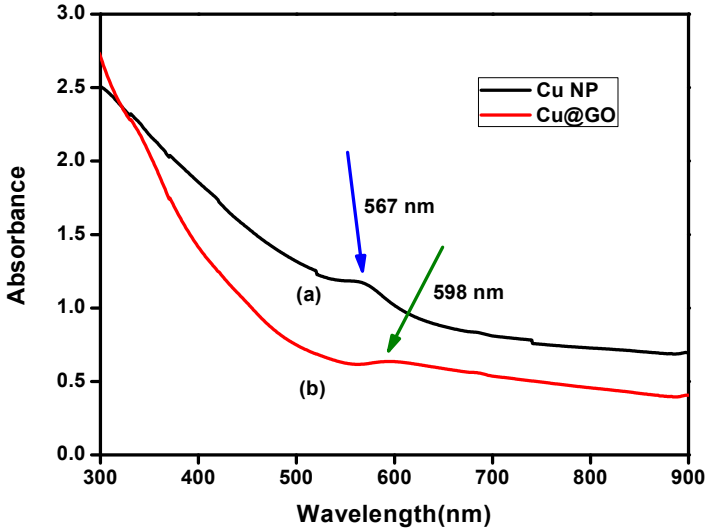


**Figure. 5.1.** (a)UV-Visible Spectroscopic image of Copper nanoparticles reduced by $NaBH_4$ in presence of Ascorbic acid has an SPR at 567 nm and (b)Copper nanoparticles synthesized in presence of graphene oxide and Ascorbic acid has an absorption maximum at 598 nm.

**5.3.1.3. EDAX analysis:** Energy-dispersive X-ray spectroscopy analysis was done to get an idea about the elemental composition of the fabricated material.

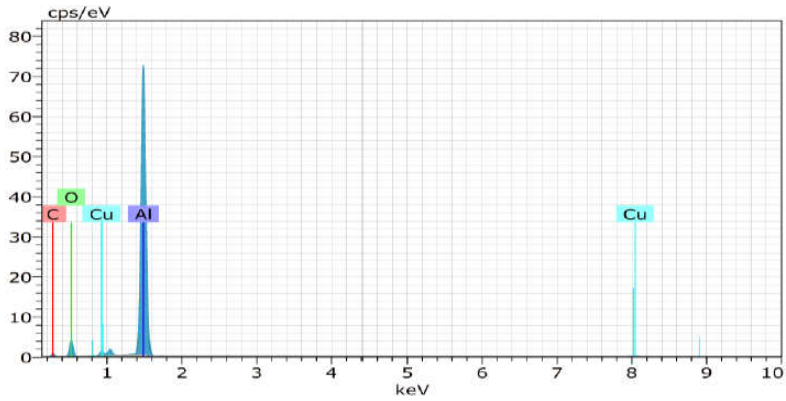


**Figure 5.2.** EDAX spectrum of Cu@GO coated on an aluminum sheet.

As can be seen in the EDAX spectrum, there are peaks at around 1 keV and 8 keV belonging to Copper. Other elements such as carbon (C) has peak at 0.2 keV and that of oxygen appears at 0.5 keV. The appearance of carbon and oxygen peaks confirms the presence of graphene oxide in the sample. The EDAX thus obtained was used for the elemental analysis. It contains Copper (1.08%), Carbon (26.72%) and Oxygen (24.18%) respectively which is confirmed by the EDAX spectrum. The composite formation was confirmed by EDAX. There is a peak correspond the element Cu, confirming the existence of metallic Cu NPs on the surface of the GO nanosheets. The presence of O indicates the several oxygen-containing functional groups in the GO, which remain unreduced during the Cu@GO composite synthesis.

### 5.3.1.4. FT-IR Studies:

To identify the presence of graphene oxide in the Cu@GO composite, we carried out the Fourier transform infrared spectroscopic analysis. The characteristic FTIR spectrum of GO nanosheets is shown

in the figure 5.3. The intense peak at 3467 $cm^{-1}$ is attributed to the O-H group stretching vibration. The absorption bands at 1635 $cm^{-1}$ can be assigned to C=O stretching of carboxylic and/or carbonyl moiety functional groups. The absorption peak at 1038 $cm^{-1}$ is assigned to the C–O stretching vibrations.

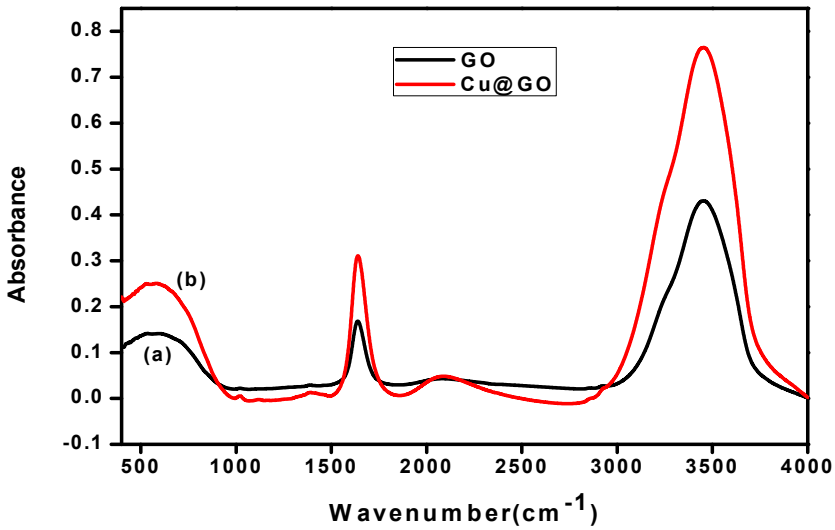


**Figure 5.3.** Fourier Transform Infrared Spectrum of (a)Graphene Oxide, (b)Cu@GO Composite.

The FT-IR spectrum of Cu@GO has the same peaks as that of graphene oxide, indicating that GO has not been reduced by the ascorbic acid and $NaBH_4$ present in the solution. So the fabricated material is confirmed to be Cu@GO, not Cu@rGO (where rGO stands for reduced graphene oxide).

### 5.3.1.5. Scanning Electron Microscopic Analysis:

In this study, the fabricated Cu@GO composite was characterized by using scanning electron microscopic analysis, which can provide better information about the size and morphology of the fabricated nanoparticles. The FE-SEM image of Cu@GO is given below.

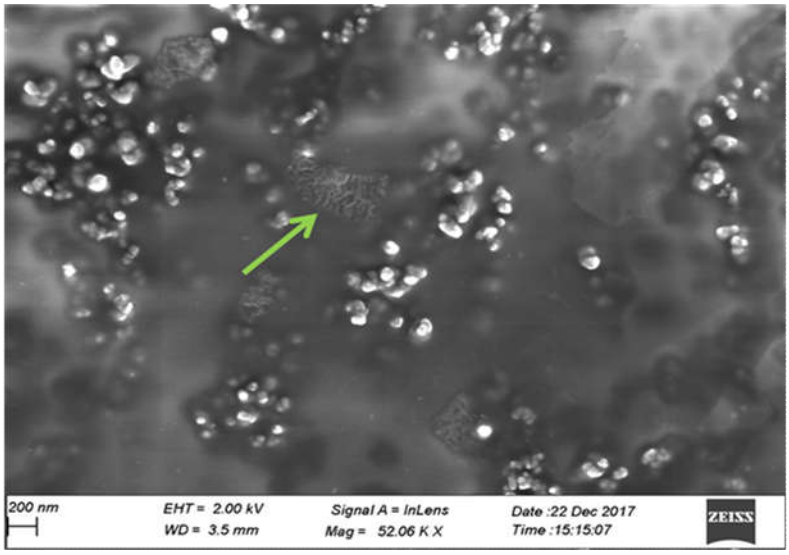


**Figure 5.4.** Field emission scanning electron microscopic (FE-SEM) image of Cu@GO composite. The unique crumpled and wrinkled structure of Graphene oxide is evident from the image (arrow mark).

It was observed that the fabricated Cu@GO composite have size lying in the nano range. It was found that they are all well dispersed without aggregation. The FE-SEM images of the fabricated Cu@GO nanocomposite showed that it has a spherical shape with size ranging from 50 nm to 80 nm. The unique crumpled and wrinkled

surface of graphene oxide which enables them to be a better substrate for surface modification is evident from the SEM image given below. Copper nanoparticles are distributed well dispersedly on the surface of GO sheets. The size of these nanoparticles lies in the range 50-80 nm. There is possibility that since the GO and copper ions are having opposite charges, Cu NPs can interact with the GO sheets through various ways such as physisorption, charge transfer or electrostatic attraction, leading to different sized nanoparticles. The high dispersity is expected to improve the sensor sensitivity.

## 5.4. Optical sensing of Hydrogen peroxide

### 5.4.1. UV-Vis Spectroscopy:

The optical detection of oxidizing species such as Hydrogen peroxide was carried out using Jasco V-550 UV-Visible Spectrophotometer. The calibration characteristics of $H_2O_2$ using Cu@GO as an optical sensor were studied. This was performed by adding varying amounts of 0.1 M $H_2O_2$ to the prepared Cu@GO composite and by taking the UV-Visible Spectra. 2 mL of Cu@GO was taken in a bottle and added varying amounts of $H_2O_2$, shaken well, and allowed to a react. The formation of bubbles in the solution was observed, due to the decomposition of $H_2O_2$ by the Cu@GO Composite. After that the absorption spectra of Cu@GO solution containing different amounts of $H_2O_2$ was recorded and analyzed. The UV-Visible spectrum of Cu@GO showing SPR at 598 nm and that after treatment with $H_2O_2$ is given below.

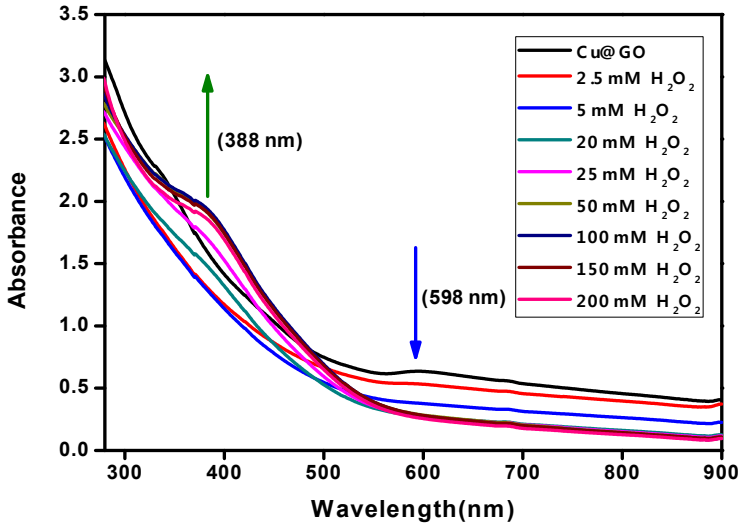


**Figure 5.5.** Cu@GO nanocomposite showing SPR at 598 nm and the disappearance of SPR upon treatment with $H_2O_2$ solution and the emergence of a new peak at 388 nm.

From Figure 5.5, it is clear that the SPR at 598 nm vanishes after treatment with $H_2O_2$ and it is observed that a new peak emerges at 388 nm and the solution turns yellow in colour. The corresponding UV-Visible spectra are given in Figure 5.6.

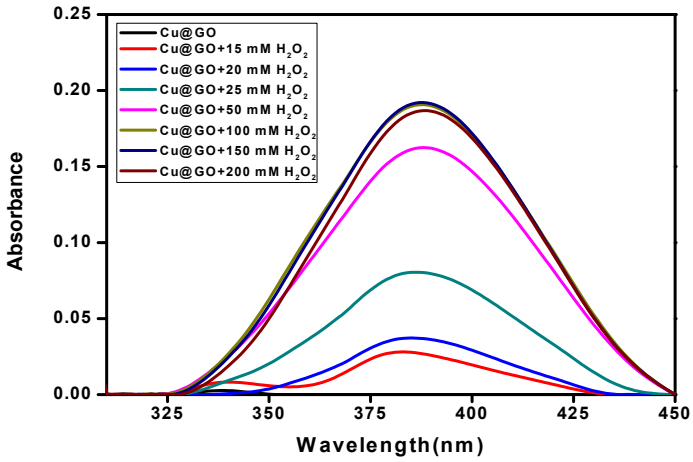


**Figure 5.6.** UV-Visible spectra of Cu@GO dispersion with varying concentrations of $H_2O_2$.

The photographic image of the Cu@GO dispersions before and after the treatment with $H_2O_2$ is presented in Figure 5.7.

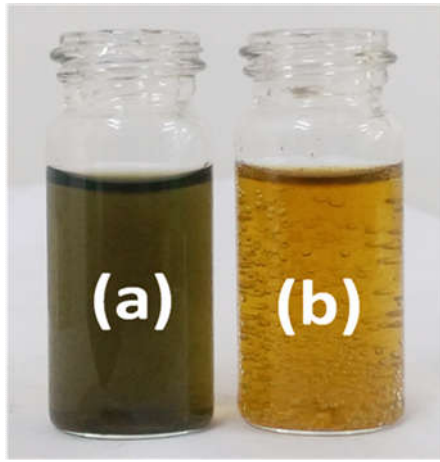


**Figure 5.7.** Photographic image of Cu@GO composite (a) before and (b) after treatment with $H_2O_2$.

A higher concentration of $H_2O_2$ solution causes a higher color change of Cu@GO composite and can even be observed with the naked eye; the color change is directly proportional to the amount of $H_2O_2$ solution added to the dispersion. As the colour change from olive green to yellow is proportional to the amount of $H_2O_2$ used, we plotted the absorbance ($\lambda_{max}$) at 388 nm against the concentration of $H_2O_2$ and the plot is shown in the Figure. 5.8.

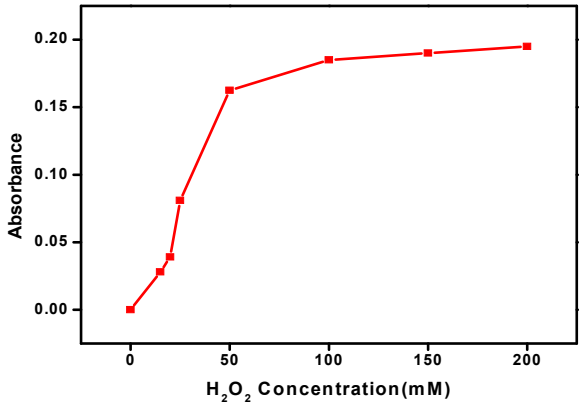


**Figure 5.8.** The plot showing the dependence of the absorbance at $\lambda_{max}$ against $H_2O_2$ concentration.

It is observed that the curve is linear at lower concentrations of $H_2O_2$ and after reaching an optimal concentration of $H_2O_2$, the difference in the absorbance becomes less significant.

We have done the same experiment with bare Copper nanoparticles. Copper nanoparticles are prepared by taking 500 µl of $CuSO_4$ (0.01 N) and 500 µl 0.01N Ascorbic acid in a round bottom

flask and is sonicated for 5 min. After that, 500 µl of 5 mM freshly prepared sodium borohydride ($NaBH_4$) solution was added to it. The colourless solution immediately changes to reddish-brown. Sonication is continued for another 10 more minutes to ensure complete reduction of $Cu^{2+}$ into $Cu^0$. The Cu NPs shows SPR at around 567nm.

It is found that the Cu(0) will undergo oxidation into $Cu^{2+}$ upon interaction with hydrogen peroxide and will go into the solution and the color of the solution changes from reddish-brown to very light blue(practically colorless). The UV-Visible spectra of $CuSO_4$ solution, Cu NPs and Cu NPs after treating with hydrogen peroxide are shown below.

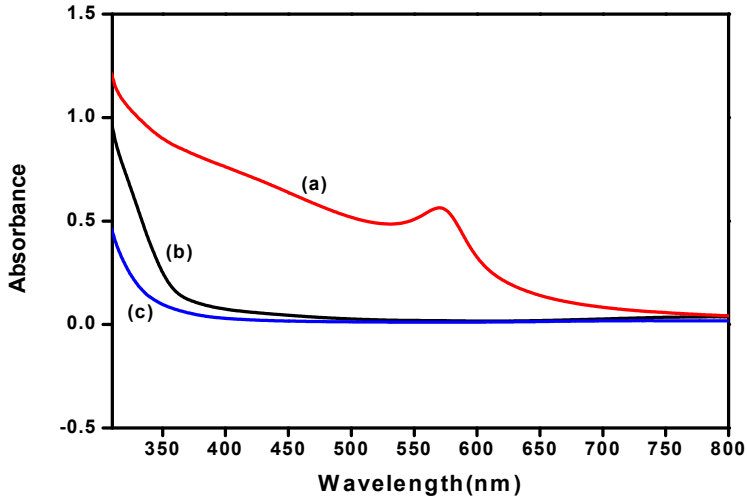


**Figure 5.9.** UV-Visible Spectra of (a) Cu nanoparticles, (b) $Cu^{2+}$ ions and (c) Cu NPs after treatment with $H_2O_2$.

The photographic image of Cu NPs before and after treatment with $H_2O_2$ is given below. The disappearance of color of Cu NPs is very evident from the image.

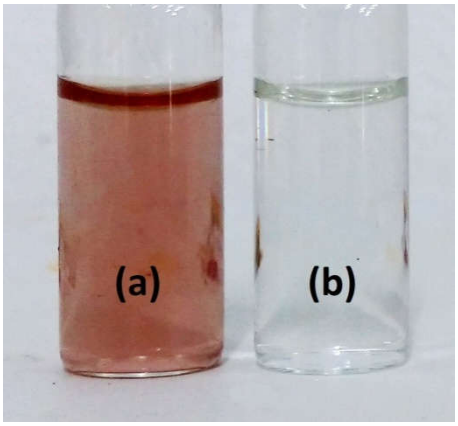


**Figure 5.10.** Photographic image of Cu NP (a) before and (b) after treatment with $H_2O_2$.

The UV-Visible absorption spectrum of Cu NPs upon treatment with varying concentrations of $H_2O_2$ is given in the figure 5.11. Here also there is loss of SPR upon interaction with peroxide as expected. But no yellow coloration is observed here and no new peak at around 390nm, instead the solution decolorizes as copper nanoparticles get oxidized onto $Cu^{2+}$. [142]

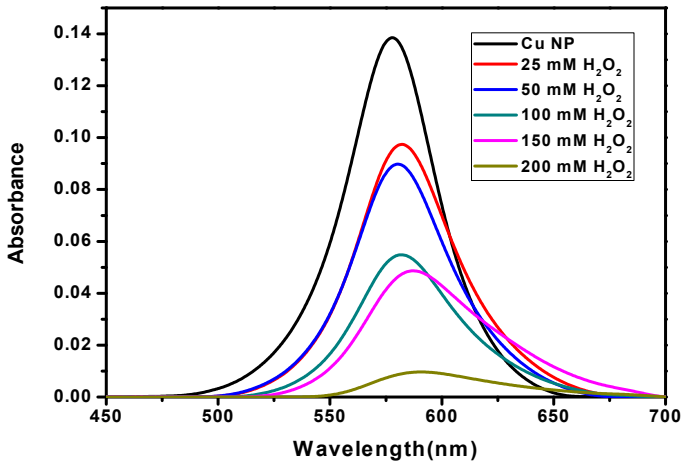


**Figure 5.11.** UV-Visible spectra of Cu NPs upon treatment with varying concentrations of hydrogen peroxide.

### 5.4.2. Interference Study

It is possible that certain amino acids and common metal ions may interfere in the sensing of $H_2O_2$. So we carried out the experiment with all these possible interfering species such as Thiamine, Alanine, Glycine, Cysteine, $CaCl_2$, $PbCl_2$, $ZnSO_4$, $MgCl_2$, $C_2O_4^{2-}$ and, $HgCl_2$ to make sure that Cu@GO is specific for $H_2O_2$ sensing. It was found that all these species doesn't produce any visible color change from green to yellow upon treatment with Cu@GO making it a reliable optical/ colorimetric sensor for $H_2O_2$ and the photographic image is given below.

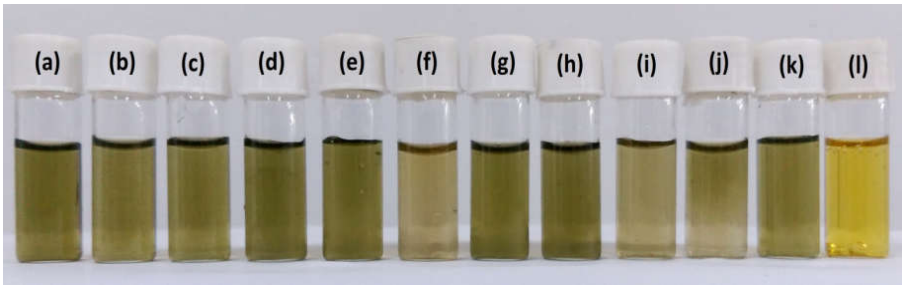


**Figure 5.12.** Photographic image of Cu@GO treated $H_2O_2$ and some common chemicals that may interfere in the $H_2O_2$ sensing. (a)Cu@GO Control, (b)Thiamine, (c)Alanine, (d)Glycine, (e)Cysteine, (f)$CaCl_2$, (g)$PbCl_2$, (h)$ZnSO_4$, (i)$MgCl_2$, (j)$C_2O_4^{2-}$, ,(k)$HgCl_2$ and (l)$H_2O_2$. It is well evident that only $H_2O_2$ is able to produce a yellow color upon treatment with Cu@GO.

It is observed that only $H_2O_2$ is able to change the olive green colour of Cu@GO composite into yellow. In the case of Cu NPs it only gets decolorized upon treatment with hydrogen peroxide. So we can say that Cu@GO is superior for peroxide sensing compared to bare Cu NPs.

## 5.5. Conclusions

In the present study, the Cu@GO nanocomposite was fabricated by a simple chemical reduction method by reducing Copper Sulphate precursor with Sodium Borohydride and GO. Ascorbic Acid is used as the stabilizing agent. The synthesized nanoparticle shows an SPR peak at 598 nm and appears dark olive green in color. The elemental composition, morphology, and other properties of the fabricated nanoparticles were characterized by using different

techniques. The Cu@GO NC has spherical morphology with an average particle size ranging from 50 nm to 80 nm which is confirmed by the SEM Analysis.

Thus formed Cu@GO dispersion is found to be excellent for detecting trace amounts of $H_2O_2$ by monitoring and analyzing the UV-Visible Spectra. There is loss of SPR and generation of a new peak at around 388 nm whose intensity is directly proportional to the amount of $H_2O_2$ hence beneficial for the quantitative determination of $H_2O_2$. The color of the solution changes from dark olive green to yellow enabling the naked eye sensing of hydrogen peroxide also. Bare Cu NPs which is brown-red in color just decolorizes upon addition of peroxide. From the results, it is obvious that the SPR characteristics and color of Cu@GO drastically got changed after $H_2O_2$ addition which is directly proportional to the $H_2O_2$ concentration. Thus we can conclude that Cu@GO can be synthesized by a simple, fast, and cost-effective method to be applied as a colorimetric sensor for $H_2O_2$ detection.

# CHAPTER 6
# CONCLUSIONS AND OUTLOOK

## 6.1. Introduction

Materials in the nanometer dimensions have been the central theme of materials research in the recent years by virtue of the unique structure and properties associated with them and the capability of tailoring smart functional materials that are capable of revolutionizing most of the conventional disciplines of physics and chemistry with potential applications in all these areas including biology and medicine. A fundamental level understanding on the structure-property relationships in materials science has also been the fruits of this still evolving nanoscience tree. Among the different classes of nanoscale systems, metal and alloy nanoparticles have been of special interest due to their unique optical and electronic properties.

The interest in the optical properties of metal nanoparticles arises primarily due to their unique surface Plasmon absorptions, resulting from the resonant absorption of electromagnetic radiation as a result of the collective oscillations of the surface electrons, which depend on the size and shape of these particles. It is well established that it is possible to tune the wavelengths of the Plasmon absorption by altering the size and shape of these particles. Theoretical models by Mie, Gan as well as the discrete dipole approximation methods have enables researchers to tailor the size, shape, and composition of metal and alloy nanoparticles to obtain the desired absorption. The nanoparticles of Au, Ag, and other metal nanoparticles have been widely used in molecular sensing and catalysis because of the high surface area of these materials in addition to their optical and

electronic properties. The works presented in this thesis is an attempt in this direction. We have developed plasmonic platforms for the detection of metal ions such as Hg (II), organic molecules (by SERS), and systems such as hydrogen peroxide which have important applications. The thesis is divided into six chapters.

## 6.2. Summary of the work

In the Chapter 1, a general introduction to nanoscience is presented with special focus on metal and alloy nanoparticles. Historical perspectives and the various theories that form the basis for the observed properties are presented herein. We have also discussed the general experimental methods for the synthesis of metal and alloy nanoparticles.

Advanced instrumental methods, particularly the electron microscopic techniques are the key to the analysis of nanomaterials. The different instrumental tools for the characterization of metal nanoparticle systems are described in Chapter 2.

In Chapter 3, we have presented the preparation of 2D arrays of metal nanoparticles. Metal nanofilms with high plasmon density are important in enable nanoparticle-based sensing such as surface-enhanced Raman spectroscopy (SERS). We propose a slow and simple anti-solvent precipitation of the metal and alloy nanoparticles from an aqueous dispersion of the nanoparticles by the slow addition of an ati-solvent, *viz*., Acetone. The advantage of this method is that there is no aggregation of nanoparticles and thus prevents the inter-plasmonic

coupling between the nanoparticles (which may result in the loss of SPR) on the deposited film. The FE-SEM images of the 2D reveal an even distribution of metal and alloy nanoparticles. It is demonstrated that these two-dimensional arrays of metal and alloy nanoparticles serves as a powerful substrate for the SERS detection of organic molecules such as BDT. These films are also shown to be useful for sensing Hg (II) ions in Chapter 4. A paper strip deposited with Ag NPs changes color from yellow to colorless making naked eye detection of Hg (II) ions rather easy.

In Chapter 4, we have presented a green chemical strategy towards the synthesis of Au, Ag, and Au-Ag NPs and the utilization of these particles towards various sensing applications. Ag and Au as well the AuAg alloy NPs of various compositions were made by using glucose as the reducing agent and starch as the capping agent. The application of Au, Ag, and AuAg alloy NPs (with different compositions) for the selective detection of mercury is presented here. The surface plasmon absorption maximum ($\lambda_{max}$) of the metal and alloy NPs undergoes significant shift upon amalgamation with Hg atoms produced by the reduction of Hg (II) ions. Since Ag nanoparticles show a notable, visual, colour change from golden yellow to colourless upon amalgamation, it would be ideal for the naked eye detection of Hg (II) ions. However, the nanoparticles of Au and the alloys also undergo significant shift in $\lambda_{max}$ ($\Delta\lambda_{max}$) upon amalgamation. In fact, the 3:2 AuAg alloy composition presented the maximum value of $\Delta\lambda_{max}$ upon amalgamation. A study on the effect of pH towards the process of amalgamation was also carried out. The

interference studies due to other metal ions were also carried out to understand the selectivity of the method.

Copper nanoparticles too are characterized by a Plasmon absorption in the visible range. The possibility of utilizing the Cu nanoparticles for the detection of Hydrogen Peroxide ($H_2O_2$) is presented in Chapter 5. In order to enhance the sensitivity, hybrid nanomaterials were prepared by incorporating Cu nanoparticles into the graphene oxide (GO) nanolayers for the selective sensing of hydrogen peroxide. The SPR of Cu@GO which is observed at the wavelength 598 nm is disappeared after treatment with peroxide and also the color changes from olive green to bright yellow enabling tanked eye detection. UV-visible spectra were taken showing the loss of SPR upon treatment with peroxide and the emergence of a new peak at the wavelength 388 nm which will be proportional to the amount of $H_2O_2$ used enabling the quantitative analysis.

# REFERENCES

1. Yetisen, A. K.; Hang, Q.; Manbachi, A.; Butt, H.; Dokmeci, M. R.; Hinestroza, J. P.; Skorobogatiy, M.; Khademhosseini, A.; Yun, S. H. Nanotechnology in Textiles. *ACS Nano*, **2016**, 10, 3042–3068.

2. Rivero, P. J.; Urrutia, A.; Goicoechea, J.; Arregui, F. J. Nanomaterials for Functional Textiles and Fibers. *Nanoscale Res. Lett*. **2015**, 10, 501.

3. El-Sayed, M. A. Small Is Different: Shape-, Size-, and Composition-Dependent Properties of Some Colloidal Semiconductor Nanocrystals. *Acc. Chem. Res*. **2004**, 37, 326-333.

4. Huang, B.; Cao, M. H.; Nie, F. D.; Huang, H.; Hu, C. W. Construction and Properties of Structure- and Size-controlled Micro/nano Energetic Materials. *Defence Technology*. **2013**, 9, 59-79.

5. Feynman, R. P. There is Plenty of Room at the Bottom, in Miniaturization, edited by H. D. Gilbert. *Reinhold Publishing Corporation, New York*. **1961**, pp. 282296.

6. Davis, B.; Ashley, S. Probing the History of Scanning Tunneling Microscopy. Discovering the Nanoscale, *Amsterdam: IOS Press*, **2004**, 145-156, ISBN: 1-58603-467-7.

7. Davis, F.; Shimizu, F. M.; Altintas, Z. Smart Nanomaterials. Biosensors and Nanotechnology: Applications in Health Care

Diagnostics, First Edition., *John Wiley & Sons, Inc*., **2018,** 219-226.

8. Kumar, R. Smart Micro/Nano Sensors and their Applications in Intelligent Sensory Network System. *Int J Sens Netw Data Commun* **2018**, 7(1), doi:10.4172/2090-4886.1000e113.

9. Ballauff, M.; Lu, Y. ‘‘Smart’’ nanoparticles: Preparation, characterization and applications, *Polymer 48*, **2007,** 1815-1823.

10. Yoshida, M.; Lahann, Smart Nanomaterials. *J. ACS Nano*, **2008**, 2, 1101–1107.

11. Iijima, S. Helical microtubules of graphitic carbon. *Nature*, **1991**, 354, 56–58.

12. Zhang, M.; Fang, S. L.; Zakhidov, A. A.; Lee, S. B.; Aliev, A. E.; Williams, C. D.; Atkinson, K. R.; Baughman, R. H. Strong, Transparent, Multifunctional, Carbon Nanotube Sheets. *Science* **2005**, 309, 1215-1219.

13. Philip, G. C.; Avouris, P. Nanotubes for Electronics. *Scientific American*, **2000**, 62-69.

14. Faraday, M. *Philos. Trans. R. Soc. Lon-don* **1857**, 147, 145 – 181.

15. Einstein, A. On the molecular-kinetic theory of the movement by heat of particles suspended in liquids at rest. *Ann. Phys*. 1905, 17, 549.

16. Mie, G. *Ann. Phys*., **1908**, 25, 377-445.

17. More, R. M. Pressure Ionization. Resonances. and the Continuity of bound and free states. *Advances in atomic and molecular physics*. **1985**, 21, 305-356.

18. Stucky, G. D.; Mac-Dougall, J. E. Quantum Confinement and Host/Guest Chemistry: Probing a New Dimension. *Science* **1990**, 247, 669-678.

19. Qi, W. H.; Wang, M. P.; Liu, Q. H. Shape factor of nonspherical nanoparticles. *Journal of materials science* **2005**, 40, 2737 – 2739.

20. Aghlara, H.; Rostami, R.; Maghoul, A.; SalmanOgliet, A. Noble metal nanoparticle surface plasmon resonance in absorbing medium. *Optik* **2015**, 126(4), 417–420.

21. Kreibig, U.; Vollmer, M. Optical Properties of Metal Clusters, *Springer*, Berlin, **1995**.

22. Zhang, J.; Zhang, L.; Xu, W. Surface plasmon polaritons: physics and applications. *Journal of Physics D: Applied Physics*, **2012**, 45(11).

23. Zayats, A. V.; Smolyaninov, I. I.; Maradudin, A. A. Nano-optics of surface plasmon polaritons. *Physics Reports* **2005**, 408, 131–314.

24. Daniel, M. C.; Astruc, D. Gold Nanoparticles: Assembly, Supramolecular Chemistry, Quantum-Size-Related Properties, and Applications toward Biology, Catalysis, and Nanotechnology. *Chem. Rev*. **2004**, 104, 293−346.

25. Wu, P.; Bai, P.; Yan, Z.; Zhao, G. X. S. Gold nanoparticles supported on mesoporous silica: origin of high activity and role of Au NPs in selective oxidation of cyclohexane. *Scientific Reports*, **2016**, 6:18817.

26. O'Regan, B.; Gratzel, M. A low-cost, high-efficiency solar cell based on dye-sensitized colloidal $TiO_2$ films. *Nature* **1991**, 353, 737–740.

27. Zhang, X.; Sun, C.; Fang, N. Manufacturing at nanoscale: Top-down, bottom-up and system engineering. *Journal of Nanoparticle Research* **2004**, 6, 125–130.

28. Daraio, C.; Jin, S. Synthesis and Patterning Methods for Nanostructures Useful for Biological Applications. *Springer*, **2011**, 27-44, ISBN: 978-0-387-31282-8.

29. Sharma, G., et al. Novel development of nanoparticles to bimetallic nanoparticles and their composites: A review.

*Journal of King Saud University – Science* **2017**. doi: 10.1016/j.jksus.2017.06.012

30. Blosi, M.; Ortelli, S.; Costa, A. L.; Dondi, M.; Lolli, A.; Andreoli, S.; Benito, P.; Albonetti, S. Bimetallic Nanoparticles as Efficient Catalysts: Facile and Green Microwave Synthesis. *Materials* **2016**, 9(7), 550.

31. Moghimi, N.; Mohapatra, M.; Leung, K. T. Bimetallic Nanoparticles for Arsenic Detection. *Anal. Chem*. **2015**, 87, 5546−5552.

32. Morris, R. H.; Collins, L. F. Optical properties of multilayer colloids. *J. Chem. Phys*. **1964**, 41, 3357-3363.

33. Link, S.; Wang, Z. L.; El-Sayed, M. A. Alloy Formation of Gold-Silver Nanoparticles and the Dependence of the Plasmon Absorption on Their Composition. *J. Phys. Chem. B* **1999**, 103, 3529-3533.

34. Lonare, A. A. and Patel, S. R. Antisolvent Crystallization of Poorly Water Soluble Drugs. *International Journal of Chemical Engineering and Applications* **2013,** 4, 337–341.

35. Reverchon, E.; De Marco, I; Porta, G. D. Tailoring of nano- and micro-particles of some superconductor precursors by supercritical antisolvent precipitation. *Journal of Supercritical Fluids* **2002**, 23, 81–87.

36. Scholl, J.; Lindenberg, C.; Vicum, L.; Brozio, J.; Mazzotti, M. Antisolvent precipitation of PDI 747: kinetics of particle formation and growth. *Crystal Growth & Design* **2007**, 7(9), 1653-1661.

37. Todokoro, H.; Ezumi, M.; Hitachi, L. Scanning electron microscopy. **1999,** US Patent: 5,872,358.

38. Williams, D.; Carter, C. B. The Transmission Electron Microscope. Transmission Electron Microscopy, Springer US, 1996, Boston, MA.

39. Fahlman, B. D. Materials Chemistry, *Springer* **2007**, 357 – 412.

40. Hornyak, G. L.; Tibbals, H. F.; Dutta, J.; Moore, J. J. Introduction to Nanoscience and Nanotechnology, *Taylor & Francis Group*, **2009**, 107 - 167.

41. Ohtsuki, Y. H. Charged beam interaction with solids. *Taylor and Francis-London* **1983**, 15(3), p 248.

42. Meitner, L. *Z. Physik* **1922**, 9(1), 131–144. https://doi.org/10.1007/BF01326962

43. Auger, P.; Ehrenfest, P.; Maze, R.; Daudin, J.; Freon, R. A. Extensive Cosmic-Ray Showers. *Rev. Mod. Phys*. **1939**, 11, 288.

44. Duparc, O. H. Pierre Auger – Lise Meitner: Comparative contributions to the Auger effect. *International Journal of Materials Research* **2009**, 100(9), 1162-1166.

45. Bentzen, S. M. Lise Meitner and Niels Bohr—A Historical Note. *Acta Oncologica* **2000,** 39(8), 1002–1003.

46. Bozzola, J. J. Electron Microscopy. Encyclopedia of life sciences, *John Wiley & Sons, Ltd*, **2002**.

47. Krumeich, F. Properties of Electrons, their Interactions with Matter and Applications in Electron Microscopy. *Laboratory of Inorganic Chemistry, ETH Zurich, Switzerland*.

48. de Marcelo, A.; Pereira-da-Silva, Ferri, F. A. Scanning Electron Microscopy, Nanocharacterization Techniques. *Micro and Nano Technologies* **2017**, 1-35.

49. Parades, A. M. Microscopy: Scanning Electron Microscopy. *Encyclopedia of food microbiology (second edition)*, **2014**, 693-701.

50. Scanning Electron Microscope A to Z, Basic knowledge of SEM, JOEL.

51. Colliex, C. Seeing and measuring with electrons: Transmission electron microscopy today and tomorrow– An introduction. *C. R. Physique* **2014**, 15, 101–109.

52. Green, D. J, Chang, R. H. Transmission electron microscopy and computer-aided image processing for 3d structural analysis of macromolecules , 155-183.

53. Goodmans, L. Theory and Applications of Ultraviolet Spectroscopy. *J. Am. Chem. Soc*. **1963**, 85 (24), 4056–4057.

54. Basic UV-Vis Theory, Concepts and Applications. Thermo Spectronic.

55. Barbara, S. Infrared Spectroscopy. Kirk-Othmer Encyclopedia of Chemical Technology. *John Wiley & Sons, Inc.* **2005**, 14, 1-20.

56. Doyle, W. M. Principles and Applications of Fourier Transform Infrared (FTIR) Process Analysis. *Technical Note AN–906 Rev. C*.

57. Naseska, M. Fourier Transform Infrared Spectroscopy, Seminar, *University of Ljubljana,* **2016**.

58. Raman, C. V.; Krishnan, K. S. The Optical Analogue of the Compton Effect. *Nature* **1928**, 121(3053), 711-711.

59. Stiles, P. L.; Dieringer, J. A.; Shah, N. C.; Van Duyne, R. P. Surface-Enhanced Raman Spectroscopy. *Annu. Rev. Anal. Chem*. **2008,** 1, 601–26.

60. Maier, S. A.; Brongersma, M. L.; Kik, P. G.; Meltzer, S.; Requicha, A. A. G.; Atwater, H. A. Plasmonics- A Route to

Nanoscale Optical Devices. *Adv. Mater*. **2001**, 13(19), 1501-1505.

61. Kelly, K. L.; Coronado, E.; Zhao, L. L.; Schatz, G. C. The Optical Properties of Metal Nanoparticles: The Influence of Size, Shape, and Dielectric Environment. *J. Phys. Chem. B* **2003**, 107, 668-677.

62. Luis, M.; Marzan, L. Tailoring Surface Plasmons through the Morphology and Assembly of Metal Nanoparticles. *Langmuir* **2006**, 22 (1), 32–41.

63. Jain, P. K.; Huang, X.; El-Sayed, I. H.; El-Sayed, M. A. Review of some interesting surface plasmon resonance-enhanced properties of noble metal nanoparticles and their applications to biosystems. *Plasmonics* **2007**, 2, 107–118.

64. Mayer, K. M.; Hafner, J. H. Localized Surface Plasmon Resonance Sensors. *Chem. Rev.* **2011**, 111 (6), 3828–3857.

65. Hu, M.; Chen, J.; Li, Z. Y.; Au, L.; Hartland, G. V.; Li, X.; Marquez, M.; Xia, Y. Gold nanostructures: engineering their plasmonic properties for biomedical applications. *Chem. Soc. Rev*. **2006,** 35(11), 1084-1094.

66. Reynolds, R. A.; C. A. Mirkin, C. A.; Letzsinger, R. L. Homogeneous, Nanoparticle-Based Quantitative Colorimetric Detection of Oligonucleotides *J. Am. Chem. Soc*. **2000**, 122, 3795 – 3796.

67. Qiang, F.; Wenbo, S. Mie theory for light scattering by a spherical particle in an absorbing medium. *Appl. Opt.* **2001,** 40(9), 1354-1361.

68. Yang, W. H.; Schatz, G. C.; Van Duyne, R. P. Discrete dipole approximation for calculating extinction and Raman intensities for small particles with arbitrary shapes. *J. Chem. Phys*. **1995**, 103, 869-875.

69. Draine, B. T.; Flatau, P. J. Discrete-dipole approximation for scattering calculations. *J. Opt. Soc. Am. A*. **1994,** 11, 1491-1499.

70. Taflove, A.; Hagness, S. C. Computational Electrodynamics: The Finite-Difference Time domain Method, *Artech House, Boston*, MA, 2**005**.

71. Bian, R. X.; Dunn, R. C.; Xie, X. S.; Leung, P. T. Single molecule emission characteristics in near-field microscopy. *Phys. Rev. Lett*., **1995**, 75, 4772-4775.

72. Moskovits, M. Surface-enhanced spectroscopy. *Rev. Mod. Phys*., **1985,** 57, 783-826.

73. Fleischmann, M.; Hendra, P. J.; McQuillan, A. J. Raman spectra of pyridine adsorbed at a silver electrode. *Chem. Phys. Lett*., **1974**, 26(2),163–166.

74. Zhang, Z.; Yang, P.; Xu, H.; Zheng, H. Surface enhanced fluorescence and Raman scattering by gold nanoparticle dimers and trimers. *J. Appl. Phys*. **2013**, 113, 033102.

75. Merlen, A.; Labarthet, F. L.; Harte, E. Surface-Enhanced Raman and Fluorescence Spectroscopy of Dye Molecules Deposited on Nanostructure Gold Surfaces. *J. Phy. Chem C* **2010**, 114, 12878-12884.

76. Huang, C. C.; Yang, Z.; Lee, K. H.; Chang, H. T. Synthesis of highly fluorescent gold nanoparticles for sensing mercury(II). *Angew. Chem. Int. Ed*. **2007**, 46, 6824 –6828.

77. Li, T.; Guo, L.; Wang, Z. Gold nanoparticle-based surface enhanced Raman scattering spectroscopic assay for the detection of protein-protein interactions. *Anal.Sci.* **2008**, 24, 907- 910.

78. Herrera, G. M.; Padilla, A. C.; Hernandez-Rivera, S. P. Surface Enhanced Raman Scattering (SERS) Studies of Gold and Silver Nanoparticles Prepared by Laser Ablation. *Nanomaterials*, **2013**, 3, 158-172.

79. Raveendran, P.; Fu, J.; Wallen, S. L. Completely "Green" Synthesis and Stabilization of Metal Nanoparticles. *J. Am. Chem. Soc*., **2003**, 125(46), 13940–13941.

80. Raveendran, P.; Fu, J.; Wallen, S. L. A simple and "green" method for the synthesis of Au, Ag, and Au–Ag alloy nanoparticles. *Green Chemistry*, **2006**, 8, 34-38.

81. Dawson, E. D.; Wallen, S. L. Probing Transport and Microheterogeneous Solvent Structure in Acetonitrile−Water Mixtures and Reversed-Phase Chromatographic Media by NMR Quadrupole Relaxation. *J. Am. Chem. Soc*. **2002**, 124, 14210-14220.

82. Reimers, J. R.; Hall, L. E. The Solvation of Acetonitrile. *J. Am. Chem. Soc*. **1999**, 121, 3730–3744.

83. Greeneltch, N. G.; Blaber, M. G.; Schatz, G. C.; Van Duyne, R. P. Plasmon-Sampled Surface-Enhanced Raman Excitation Spectroscopy on Silver Immobilized Nanorod Assemblies and Optimization for Near Infrared (λex = 1064 nm) Studies. *J. Phys. Chem. C*. **2013**, 117(6), 2554-2558.

84. Sivapalan, S. T.; Devetter, B. M.; Yang, T. K.; van Dijk, T.; Schulmerich, M. V.; Carney, P. S.; Bhargava, R.; Murphy, C. J. Off-resonance surface-enhanced Raman spectroscopy from gold nanorod suspensions as a function of aspect ratio: not what we thought. *ACS Nano*, **2013,** 7, 2099-2105.

85. Jaishankar, M.; Tseten, T.; Anbalagan, N.; Mathew, B. B.; Beeregowda, K. N. Toxicity, mechanism and health effects of some heavy metals. *Interdiscip Toxicol*. **2014,** 7(2), 60–72.

86. Tchounwou, P. B.; Yedjou, C. G.; Patlolla, A. K.; Sutton, D. J. Heavy Metals Toxicity and the Environment. *EXS*. **2012**, 101, 133–164.

87. Sharma, R. K.; Agrawal, M. Biological effects of heavy metals: An overview. *J. Environ. Biol*. **2005**, 26, 301-313.

88. Achparaki, M.; Thessalonikeos, E.; Tsoukali, H.; Mastrogianni, O.; Zaggelidou, E.; Chatzinikolaou, F.; Vasilliades, N.; Raikos. N. Heavy metals toxicity. *Aristotle University Medical Journal* **2012**, 39(1), 29-34.

89. Broussard, L. A.; Hammett-Stabler, C. A.; Winecker, R. E.; Ropero-Miller, J. D. The Toxicology of Mercury. *Laboratorymedicine* **2002**, 33(8), 614-625.

90. Azevedo, B. F. et. al. Toxic Effects of Mercury on the Cardiovascular and Central Nervous Systems. *J Biomed Biotechnol*. **2012**; 2012: 11 pages, Article ID: 949048.

91. Park, J. D.; Zheng, W. Human Exposure and Health Effects of Inorganic and Elemental Mercury. *J Prev Med Public Health*. **2012,** 45(6), 344–352.

92. Yu, L.; Yan, X. Flow injection on-line sorption preconcentration coupled with cold vapor atomic fluorescence spectrometry and on-line oxidative elution for the determination of trace mercury in water samples. *At. Spectrosco*. 2004, 25, 145-153.

93. Capelo, J. L.;, Maduro, C.; Mota, A. M. Evaluation of focused ultrasound and ozonolysis as sample treatment for direct determination of mercury by FI-CV-AAS. Optimization of

parameters by full factorial design. *Ultrason Sonochem*. **2006,** 13(1), 98-106.

94. Martinis, E. M.; Berton, P.; Olsina, R. A.; Altamirano, J. C.; Wuilloud, R. G.; Mater, J. H. Trace mercury determination in drinking and natural water samples by room temperature ionic liquid based-preconcentration and flow injection-cold vapor atomic absorption spectrometry. *Journal of hazardous materials* **2009**, 167, 475-481.

95. Li, Q.; Zhou, X.; Xing, D. Rapid and highly sensitive detection of mercury ion ($Hg^{2+}$) by magnetic beads-based electrochemiluminescence assay. *Biosens. Bioelectron*. **2010**, 26, 859-862.

96. Chen, K. H.; Wang, H. W.; Kang, B. S.; Chang, C. Y.; Wang, Y. L.; Lele, T. P.; Ren, F.; Pearton, S. J.; Dabiran, A.; Osinsky, A.; Chow, P. P. Low Hg(II) ion concentration electrical detection with AlGaN/GaN high electron mobility transistors. *Sensors and Actuators B* **2008**, 134, 386–389.

97. Diez, S.; Bayona, J. M. Determination of Hg and organomercury species following SPME: A review. *Talanta* **2008**, 77, 21–27.

98. Morita, M.; Yoshinaga, J.; Edmonds, J. S. The determination of mercury species in environmental and biological samples. *Pure and Applied Chemistry.* **1998**, 70, 1585-1615.

99. Wang, M.; Feng, W.; Shi, J.; Zhang, F.; Wang, B.; Zhu, M.; Li, B.; Zhao, Y.; Chai, Z. Development of a mild mercaptoethanol extraction method for determination of mercury species in biological samples by HPLC–ICP-MS. *Talanta* **2007**, 71, 2034–2039.

100. Gao, Y.; Shi, Z.; Long, Z.; Wu, P.; Zheng, C.; Hou, Z. Determination and speciation of mercury in environmental and biological samples by analytical atomic spectrometry. *Microchem. J.* **2012**, 103, 1–14.

101. Leopold, K.; Foulkes, M.; Worsfold, P. Methods for the determination and speciation of mercury in natural waters-A review. *Anal. Chim. Acta.* **2010**, 663, 127–138.

102. Selid, P. D.; Xu, H.; Collins, E. M.; Face-Collins, M. S.; Zhao, J. X. Sensing Mercury for Biomedical and Environmental Monitoring. *Sensors* **2009**, *9*, 5446-5459.

103. Gotzl, A.; Riepe, W. Mercury determination — SPME and colorimetric spot test. *Talanta* **2001**, 54, 821–827.

104. Paciornik, S.; Yallouz, A. V.; Campos, R. C.; Gannermand, D. Scanner Image Analysis in the Quantification of Mercury using Spot-Tests. *J. Braz. Chem. Soc.* **2006**, 17(1), 156-161.

105. Alex V. A Spot Test Scheme for the Identification of Metal Ions. *J. Chem. Educ*. **1962,** 39(8), 395.

106. Fitri, Z.; Muhammad, A. Gold and silver nanoparticles and indicator dyes as active agents in colorimetric spot and strip tests for mercury(II) ions: a review. *Microchim Acta* **2017,** 184, 45–58.

107. Feigl, F. Spot tests based on the action and formation of mercuric cyanide. *Israel journal of chemistry* **1967**, 5, 1-14.

108. Gonzalez, A. L.; Cecilia, N.; Beranek, J.; Barnard, A. S. Size, Shape, Stability and Color of Plasmonic Silver Nanoparticles. *J. Phys. Chem. C* **2014**, 118, 9128−9136.

109. Cao, W.; Huang, T.; Xu, X. H.; Elsayed-Ali, H. E. Localized surface plasmon resonance of single silver nanoparticles studied by dark-field optical microscopy and spectroscopy. *J. Appl. Phys*. **2011**, 109, 034310.

110. Amendola, V.; Bakr, O. M.; Stellacci, F. A Study of the Surface Plasmon Resonance of Silver Nanoparticles by the Discrete Dipole Approximation Method: Effect of Shape, Size, Structure, and Assembly. *Plasmonics* **2010,** 5, 85–97.

111. Katok, K. V.; Whitby, R. L.; Fukuda, T.; Maekawa, T.; Bezverkhyy, I.; Mikhalovsky, S. V.; Cundy, A. B. Hyperstoichiometric Interaction between Silver and Mercury at the Nanoscale. *Angew. Chem. Int. Ed.* **2012**, 51, 2632 –2635.

112. Annadhasan, M.; Muthukumarasamyvel, T.; Sankar Babu, V. R.; Rajendiran, N. Green Synthesized Silver and Gold

Nanoparticles for Colorimetric Detection of $Hg^{2+}$, $Pb^{2+}$, and $Mn^{2+}$ in Aqueous Medium. *ACS Sustainable Chem. Eng*. **2014**, 2, 887−896.

113. Wu, L. P.; Zhao, H. W.; Qin, Z. H.; Zhao, X. Y.; Pu, W. D. Highly Selective Hg (II) Ion Detection Based on Linear Blue-Shift of the Maximum Absorption Wavelength of Silver Nanoparticles. *J Anal Methods Chem*. **2012**, vol. 2012, Article ID 856947, 5 pages.

114. Kumar, V.; Singh, D. K.; Mohan, S.; Bano, D.; Gundampati, R. K.; Hasan, S. H. Green synthesis of silver nanoparticle for the selective and sensitive colorimetric detection of mercury (II) ion. *J. Photochem. Photobiol. B* **2017**, 168, 67–77.

115. Vasileva, P.; Alexandrova, T.; Karadjova, I. Application of Starch-Stabilized Silver Nanoparticles as a Colorimetric Sensor for Mercury(II) in 0.005 mol/L Nitric Acid. *Journal of Chemistry*, **2017**, vol. 2017, Article ID 6897960, 9 pages.

116. Firdaus, M. L.; Fitriani, I.; Wyantuti, S.; Hartati, Y. W.; Khaydarov, R.; McAlister, J. A.; Obata, H,; Gamo, T. Colorimetric Detection of Mercury (II) Ion in Aqueous Solution Using Silver Nanoparticles. *Anal. Sci.* **2017**, 33(7), 831-837.

117. Radhakumary, C.; Sreenivasan, K. Gold nanoparticles generated through ‘‘green route’’ bind $Hg^{2+}$ with a concomitant

blue shift in plasmon absorption peak. *Analyst* **2011**, 136 (14), 2959−2962.

118. Morris, T.; Copeland, H.; McLinden, E.; Wilson, S.; Szulczewski, G. The Effects of Mercury Adsorption on the Optical Response of Size-Selected Gold and Silver Nanoparticles. *Langmuir* **2002**, 18, 7261-7264.

119. Farhadi, K.; Forough, M.; Molaei, R.; Hajizadeh, S.; Rafipour, A. Highly selective Hg2+ colorimetric sensor using green synthesized and unmodified silver nanoparticles. *Sens. Actuators, B* **2012**, 161, 880−885.

120. Kroto, H. W.; Heath, J. R.; O'Brien, S. C.; Curl, R. F.; Smalley, R. E. $C_{60}$: Buckminsterfullerene, *Nature* **1985**, 318, 162-163.

121. Smalley, R. E. Discovering the fullerenes, *Rev. Mod. Phys*. **1997,** 69(3), 723.

122. Terrones M., Hsu W.K., Kroto H.W., Walton D.R.M. Nanotubes: A Revolution in Materials Science and Electronics. In: Hirsch A. (eds) Fullerenes and Related Structures. Topics in Current Chemistry, 1999, 199. Springer, Berlin, Heidelberg.

123. Daniel, V. S.; Carbon Nanotubes and Related Structures: New Materials for the Twenty-First Century. *Am. J. Phys*. **2004**, 72(3), 414-15.

124. Loh, K. P.; Bao, Q.; Eda, G.; Chhowalla, M. Graphene oxide as a chemically tunable platform for optical applications. *Nature chemistry*, **2010**, 2, 1015-24.

125. Zhu, Y.; Murali, S.; Cai, W.; Li, X.; Suk, J. W.; Potts, J. R.; Ruoff, R. S. Graphene and Graphene Oxide: Synthesis, Properties, and Applications. *Adv. Mater*. **2010,** 22, 3906–3924.

126. Rattana, T.; Chaiyakun, S.; Witit-anun, N.; Nuntawong, N.; Chindaudom, P.; S. Oaew, S.; Kedkeaw, C.; Limsuwan, P. Preparation and characterization of graphene oxide nanosheets. *Procedia Engineering*. **2012**, 32, 759 – 764.

127. Hu, X.; Yu, Y.; Hou, W.; Zhou, J.; Song, L. Effects of particle size and pH value on the hydrophilicity of graphene oxide. *Applied Surface Science*. **2013**, 273, 118–121.

128. Kavinkumar, T.; Manivannan, S. Uniform decoration of silver nanoparticle on exfoliated graphene oxide sheets and its ammonia gas detection, *Ceram. Int*. **2016**, 42, 1769–1776.

129. Wang, H. L.; Dai, H. J. Strongly coupled inorganic–nano-carbon hybrid materials for energy storage. *Chem. Soc. Rev*. **2013**, 42, 3088–3113.

130. Bai, H.; Li, C.; Shi, G. Q. Functional composite materials based on chemically converted graphene. *Adv. Mater*. **2011**, 23, 1089–1115.

131. Li, H.; Song, Z.; Zhang, X.; Huang, Y.; Li, S.; Mao, Y.; Ploehn, H. J.; Bao, Y.; Yu, M. Ultrathin, molecular-sieving graphene oxide membranes for selective hydrogen separation. *Science* **2013**, 342, 95–98.

132. Kuila, T.; Mishra, A. K.; Khanra, P.; Kim, N. H.; Lee, J. H. Recent advances on the efficient reduction of graphene oxide and its application as energy storage electrode materials, *Nanoscale* **2013**, 5, 52–71.

133. Stankovich, S.; Dikin, D.A.; Dommett, G. H. B.; Kohlhaas, K. M.; Zimney, E. J.; Stach, E. A.; Piner, R. D.; Nguyen, S. T.; Ruoff, R. S. Graphene-based composite materials. *Nature* **2006**, 442, 282–286.

134. Xu, W. P.; Zhang, L. C.; Li, J. P.; Lu, Y.; Li, H. H.; Ma, Y. N.; Wang, W. D.; Yu, S. H. Facile synthesis of silver@graphene oxide nanocomposites and their enhanced anti-bacterial properties. *J. Mater. Chem*. **2011**, 21, 4593–4597.

135. Pant, B.; Pokharel, P.; Tiwari, A. P.; Saud, P. S.; Park, M.; Ghouri, Z. K.; Choi, S.; Park, S. J.; Kim, H. Y. Characterization and anti bacterial properties of aminophenol grafted and Ag NPs decorated graphene nanocomposites. *Ceram. Int*. **2015**, 41, 5656–5662.

136. deFaria, A. F.; Martinez, D. S. T.; Meira, S. M. M.; deMoraes, A. C. M.; Brandelli, A.; Filho, A. G. S.; Alves, O. L. Anti-adhesion and antibacterial activity of silver nano- particles

supported on graphene oxidesheets. *Coll. Surf. B: Biointerfaces* **2014**, 113, 115–124.

137. Tang, X. Z.; Cao, Z. W.; Zhang, H. B.; Liu, J.; Yu, Z. Z. Growth of silver nanocrystals on graphene by simultaneous reduction of graphene oxide and silver ions with a rapid and efficient one-step approach. *Chem. Commun*. **2011**, 47, 3084–3086.

138. Lue, S. J. et. al. The Preparation of Graphene Oxide-Silver Nanocomposites: The Effect of Silver Loads on Gram-Positive and Gram-Negative Antibacterial Activities. *Nanomaterials* **2018**, 8, 163.

139. Gu, D. et. al., Efficient synthesis of silver-reduced graphene oxide composites with prolonged antibacterial effects, Ceram. Int. 2016. http://dx.doi.org/10.1016/j.ceramint.2016.03.069i

140. Kamali, K. Z.; Pandikumar, A.; Sivaraman, G.; Lim, H. N.; Wren, S. P.; Sun, T.; Huang, N. M. Silver@Graphene Oxide Nanocomposite-Based Optical Sensor Platform for Biomolecules. DOI: 10.1039/C4RA11356J

141. Li, C.; Wang, X.; Chen, F.; Zhang, C.; Zhi, X.; Wang, K.; Cui, D. The antifungal activity of graphene oxide–silver nanocomposites. *Biomaterials* **2013**, 34, 3882–3890.

142. Roy, K.; Ghosh, C. K.; Sarkar, C. K. Rapid detection of hazardous $H_2O_2$ by biogenic copper nanoparticles synthesized

using Eichhornia crassipes extract. *Microsyst. Technol.* **2017**. DOI:10.1007/s00542-017-3480-z.

143. Ashdown, B. C.; Stricof. D. D.; May, M. L.; Sherman, S. J.; Carmody, R. F. Hydrogen Peroxide Poisoning Causing Brain Infarction: Neuroimaging Findings. *AJR* **1998**, 170, 1653-1655.

144. Watt, B. E.; Proudfoot, A. T.; Vale, J. A. Hydrogen Peroxide Poisoning. *Toxicol. Rev*. **2004**, 23 (1), 51-57.

145. Sinduja, B.; John, S. A. Ultrasensitive optical sensor for hydrogen peroxide using silver nanoparticles synthesized at room temperature by GQDs. *Sens. Actuators, B* **2017**, 247, 648–654.

146. Wang, H.; Wang, H.; Li, T.; Ma, J.; Li, K.; Zuo, X. Silver nanoparticles selectively deposited on graphene-colloidal carbon sphere composites and their application for hydrogen peroxide sensing. *Sens. Actuators, B* **2017**, 239, 1205–1212.

147. Farrokhnia, M.; Karimi, S.; Momeni, S.; Khalililaghab, S. Colorimetric sensor assay for detection of hydrogen peroxide using green synthesis of silver chloride nanoparticles: Experimental and theoretical evidence. *Sens. Actuators, B* **2017**, 246, 979–987.

148. Uzer, A.; Durmazel, S.; Ercag, E.; Apak, R. Determination of hydrogen peroxide and triacetone triperoxide(TATP) with a

silver nanoparticles-based turn-on colorimetric sensor. *Sens. Actuators, B* **2017**, 247, 98–107.

149. Nitinaivinij, K.; Parnklang, T.; Thammacharoen, C.; Ekgasit, S.; Wongravee, K. Colorimetric determination of hydrogen peroxide by morphological decomposition of silver nanoprisms coupled with chromaticity analysis. *Anal. Methods* **2014**, 6, 9816–9824.

150. Arena, A.;, Scandurra, G.; Ciofi, C. Copper Oxide Chitosan Nanocomposite: Characterization and Application in Non-Enzymatic Hydrogen Peroxide Sensing. *Sensors* **2017**, 17, 2198.

151. Wang, Y.; Wei, W.; Zeng, J.; Liu, X.; Zeng, X. Fabrication of a copper nanoparticle/ chitosan/ carbon nanotube-modified glassy carbon electrode for electrochemical sensing of hydrogen peroxide and glucose. *Microchim Acta* **2008**, 160, 253–260.

152. Liu, Y.; Han, Y.; Chen, R.; Zhang, H.; Liu, S.; Liang, F. In situ Immobilization of Copper Nanoparticles on Polydopamine Coated Graphene Oxide for $H_2O_2$ Determination. PLoS *ONE* **2016**, 11(7): e0157926. doi:10.1371/journal.pone.0157926

153. Tang, K.; Wu, X.; Wang, G.; Li, L.; Wu, S.; Dong, X.; Liu, Z.; Zhao, B. One-step preparation of silver nanoparticle embedded amorphous carbon for non-enzymatic hydrogen peroxide sensing. *Electrochem. Commun*. **2016**, 68, 90–94.

154. Li, Q. Z.; Qin, X. Y.; Luo, Y. L.; Lu, W. B.; Chang, G. H.; Asiri, A. M.; Al-Youbi, A. O.; Sun, X. P. One-pot synthesis of Ag nanoparticles/reduced graphene oxide nanocomposites and their application for non-enzymatic $H_2O_2$ detection. *Electrochim. Acta* **2012**, 83, 283–287.

155. Niaa, P. M.; Woia, P. M.; Alias, Y. Facile one-step electrochemical deposition of copper nanoparticles and reduced graphene oxide as non-enzymatic hydrogen peroxide sensor. *Appl. Surf. Sci.* **2017**, 413, 56–65.

156. Rezaei, B.; Askarpour, N.; Ghiaci, M.; Niyazian, F.; Ensafi, A. A. Synthesis of Functionalized MWCNTs decorated with Copper Nanoparticles and its application as a sensitive sensor for amperometric detection of $H_2O_2$. *Electroanalysis* **2015**, 27, 1-10.

157. Dang, T. M. D.; Le, T. T. T.; Fribourg-Blanc, E.; Dang, M. C. Synthesis and optical properties of copper nanoparticles prepared by a chemical reduction method. *Adv. Nat. Sci.: Nanosci. Nanotechnol*. **2011**, 2, 015009 (6pp)

158. Ayesha, K.; Rashid, A.; Younas, R.; Ren Chong. A chemical reduction approach to the synthesis of copper nanoparticles. *Int. Nano Lett*. **2016**, 6, 21–26.

159. Ji, Z.; Shen, X.; Zhu, G.; Zhou, H.; Yuan, A. Reduced graphene oxide/nickel nanocomposites: facile synthesis, magnetic and catalytic properties. *J. Mater. Chem.* **2012**, 22, 3471.

# APPENDIX

**Refereed Journals**

1. Anju Ajayan, Vineeth Madhavan, Sumitha Chandran and Poovathinthodiyil Raveendran*, A simple anti-solvent method for the controlled deposition of metal and alloy nanoparticles, *New J. Chem.*, 2018, 42, 11979-11983.
2. Vineeth Madhavan, Pranav Gangadharan, Anju Ajayan, Sumitha Chandran, Poovathinthodiyil Raveendran*. Microwave-assisted solid-state synthesis of Au nanoparticles, size-selective speciation, and their self-assembly into 2D-superlattice. *Nano-Structures & Nano-Objects,* Elsevier.

**Conference Proceedings**

1. Poster presentation at the Fourth International Conference on Frontiers in Nanoscience and Technology, COCHIN NANO 2016 at CUSAT Cochin.
2. Oral presentation at National seminar "The Green chemical strategies and Technologies" held at St. Josephs College, Devagiri, Kozhikode.
3. Poster presentation at SCICON’16 - International Conference on Advanced Materials Held at Amrita Vishwa Vidyapeetham.